OPTIMAL DESIGN AND CONTROL

OF A LOWER-LIMB PROSTHESIS

WITH ENERGY REGENERATION

HOLLY E. WARNER

Bachelor of Science in Mechanical Engineering

Cleveland State University

May 2014

submitted in partial fulfillment of requirements for the degree

MASTERS OF SCIENCE IN MECHANICAL ENGINEERING

at the

CLEVELAND STATE UNIVERSITY

AUGUST 2015

We hereby approve this thesis for

HOLLY E. WARNER

Candidate for the Master of Science in Mechanical Engineering degree for the

Department of Mechanical Engineering

and the CLEVELAND STATE UNIVERSITY

College of Graduate Studies

_____

Thesis Chairperson, Daniel Simon, Ph.D.

_____

Department & Date

_____

Thesis Committee Member, Hanz Richter, Ph.D.

_____

Department & Date

_____

Thesis Committee Member, Antonie van den Bogert, Ph.D.

_____

Department & Date

Student's Date of Defense: August 11, 2015

ACKNOWLEDGMENTS

OPTIMAL DESIGN AND CONTROL OF A LOWER-LIMB PROSTHESIS WITH
ENERGY REGENERATION

HOLLY E. WARNER

ABSTRACT

The majority of amputations are of the lower limbs. This correlates to a particular need for lower-limb prostheses. Many common prosthesis designs are passive in nature, making them inefficient compared to the natural body. Recently as technology has progressed, interest in powered prostheses has expanded, seeking improved kinematics and kinetics for amputees. The current state of this art is described in this thesis, noting that most powered prosthesis designs do not consider integrating the knee and the ankle or energy exchange between these two joints. An energy regenerative, motorized prosthesis is proposed here to address this gap.

After preliminary data processing is discussed, three steps toward the realization of such a system are completed. First, the design, optimization, and evaluation of a knee joint actuator are presented. The final result is found to be consistently capable of energy regeneration across a single stride simulation. Secondly, because of the need for a prosthesis simulation structure mimicking the human system, a novel ground contact model in two dimensions is proposed. The contact model is validated against human reference data. Lastly, within simulation a control method combining two previously published prosthesis controllers is designed, optimized, and evaluated. Accurate tracking across all joints and ground reaction forces are generated, and the knee joint is shown to have human-like energy absorption characteristics. The successful completion of these three steps contributes toward the realization of an optimal combined knee-ankle prosthesis with energy regeneration.

TABLE OF CONTENTS

LIST OF FIGURES

LIST OF TABLES

CHAPTER I

INTRODUCTION

Lower limb amputations are frequent among those with diabetes mellitus. In the year 2009 alone approximately 68,000 hospital discharges in the United States were due to amputations, an increase of 24% compared to 20 years before [7]. In recent years amputations due to traumatic injuries related to military service have increased as well. More than 75% of these amputations were of the lower extremities; 34.5% were transfemoral, indicating loss of both the knee and the ankle joints [23]. Especially among transfemoral amputees, therefore, it is a challenge to find the best prosthesis solution.

1.1 Motivation

The majority of above knee amputees currently use passive prostheses. These include devices such as the Mauch SNS, Rheo Knee, and C-leg. While microcontroller knees, such as the C-leg, improve upon the purely mechanical knees, such as the Mauch SNS, there are still significant deficits relative to able-bodied motion; see Figure 1 [12]. As depicted, users of both types of prostheses lack knee flexion during stance and ankle plantarflexion during push-off, both of which are requirements for proper gait kinematics. This frequently leads to extensive health issues beyond
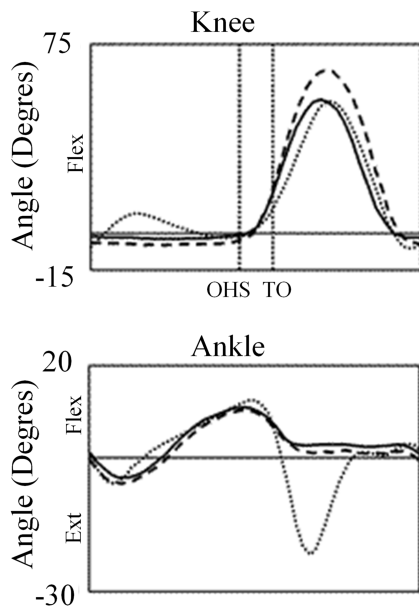
Figure 1: Gait of able-bodied (dotted line), C-leg (solid line), and Mauch leg (dashed line) subjects. Adapted from [38]. Used with permission, Appendix L

the original cause of the amputation. Examples include the fact that amputees are 25% more likely to have osteoarthritis compared to able-bodied individuals [44]. Furthermore, amputees have an 88% probability of osteoporosis. The likelihood of back problems also increases to 52% [8].

In addition to the ancillary health issues associated with poor kinematics, amputees expend up to 50% more energy than able-bodied persons [11]. The expense of motion further degrades amputees' quality of life. The source of this loss is primarily the architecture of prostheses. Most prostheses use passive damping and stiffness to regulate the motion of the knee and ankle, respectively. Previous research, Figure 2, shows that the knee has a net negative power (absorption) while the ankle has a net positive power (generation). Accordingly, passive prostheses incur significant energy loss at the knee and cannot provide active ankle push-off. These designs prove cumbersome not only for walking, but also for energy-intensive tasks such as standing up and ascending stairs.

Recent prosthesis development has addressed user mobility issues by motor-
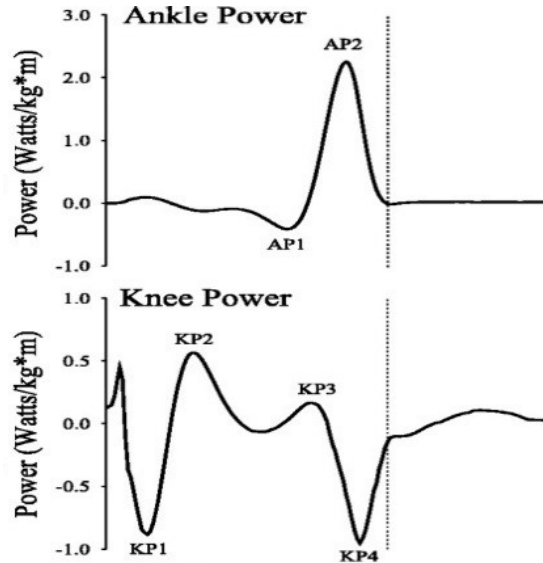
Figure 2: Joint power consumption (positive) and absorption (negative) for able-bodied gait. Adapted from [25]. Used with permission, Appendix L

izing the knee as in the Power Knee, but energy losses and the lack of active ankle push-off have not been considered in this case. An active ankle prosthesis has also been commercialized, but is not made to be integrated with a powered knee [13]. An exception to this dichotomy is a prototype leg developed at Vanderbilt University with motors at both knee and ankle; however, it is not commercially available [46]. One of the major drawbacks to each of these powered devices is battery life. The usage time for the Power Knee is between five and seven hours [31]. For the Vanderbilt leg the limit is about two hours of walking before recharging is required [46].

To explain the intensive energy usage of these devices, one may refer back to Figure 2. It is known that the natural leg transfers much of the excess energy at the knee to the ankle, which is a net consumer of energy. Quantitatively, for an average able-bodied gait case at a fast walking pace the knee produces a net 29.5 J of energy, and the ankle consumes 30.6 J of energy [52]. Assuming perfect efficiency, this leaves only 1.1 J to metabolic energy expenditure. It is not indicated that any of the previously mentioned powered devices were designed with this feature of the able-bodied system in mind. Accordingly, it would seem an optimal combination to

design an active prosthesis, such that gait kinematics and kinetics may be accurately restored, with the capacity for energy regeneration, extending battery life.

In considering a motor-driven active prosthesis design, control is also of great importance. Control is the essence of the interaction between the human and prosthesis. It determines whether the motion, joint torques, and energy usage mimic the natural system or not. Current prosthesis control strategies frequently do not take into account their resulting energetic performance. Consideration for energy flows associated with prosthesis controllers has been developed only recently [34, 37].

1.2 Literature Review

The development of a powered, energy regenerative prosthesis has been considered in the past literature. As early as the 1980's this idea was under development at the Massachusetts Institute of Technology. In [39] and [48] a prosthesis with an active knee joint is developed with the intent to implement energy regeneration. Because of hardware limitations the device was never commercialized, and the experimental regeneration efficiency was significantly less than predicted.

More recently, several different approaches to energy regeneration have been evaluated. Reference [49] presents an electrically-based energy regenerative active knee prosthesis. This too was limited by hardware as batteries cannot meet the high charging rate demanded to absorb the excess power of the knee. Mechanical alternatives have also been developed. In [9] a ratchet-like mechanism is implemented at the passive knee joint. The stored energy is then transferred to assist the ankle joint, which is motorized, during push off. A spring and clutch system is introduced for a passive ankle joint in [4]. Both of these systems, while they meet the intended purpose, are not directly controllable, and the latter does not address the knee joint, which is fundamental. Hydraulic energy storage has been attempted as well. Refer-

ence [50] describes the development of a knee prosthesis in which the energy collected from the knee is stored via an accumulator and released back to power the knee joint as necessary. However, like others, efficiency was a clear limiting factor for this system.

Seeking the controllability of an electrical system, a new approach is offered in [33]. Due to the recent advent of the supercapacitor, the realization of an electrically regenerative active knee and ankle prosthesis may be possible. The inspiration to use a supercapacitor-based storage system is derived from work with hybrid and electrical vehicles such as [5]. Supercapacitors have the ability to absorb large amounts of energy in short periods of time, which was the limiting factor in [49]. With optimal design of both the mechanical and control systems integrated with a supercapacitor storage unit, perhaps the efficiency proposed within some of the aforementioned works may be obtained.

1.3   Thesis Contributions and Organization

Several steps in the process of developing a regenerative motorized knee and ankle prosthesis will be presented. These include a knee joint actuator system, an optimal ground contact simulation method, and a controller for both the knee and ankle. The presentation of these topics is completed as discussed next.

Because of the intensive human aspect of this work, a solid set of reference data must be developed. The methods used in preparing the reference data are described in Chapter II. The next topic, actuator modeling and optimization, begins the contributions of this work and is covered in Chapter III. An improved method of simulating the effects of ground contact in a two-dimensional model is subsequently developed, Chapter IV. In Chapter V a novel controller relating to a complete leg simulation is presented with a particular emphasis on the control of the above knee

prosthesis and the controller's optimization. Chapter VI closes with a discussion and suggestions for future work.

CHAPTER II

REFERENCE DATA

For the primary contributions of this work several sets of reference data are required. This data will be used for both performance evaluation and controller tracking. To make use of this data, preliminary processing must be completed. Two separate data cases must be prepared. The first is a single trial, one stride dataset originating from the Cleveland Clinic gait lab (Cleveland Clinic, Cleveland, Ohio). This data was used for the study presented in [33], which is related to this work. Therefore, for consistency the Cleveland Clinic (CC) data will be used for a portion of this work.

While a single stride is sufficient for initial analysis, it does not accurately represent the daily activities of an amputee. Accordingly, a more extensive dataset was used in this work as well. This dataset was obtained from a collaboration with the Louis Stokes Cleveland Veterans Administration (Cleveland VA Medical Center, Cleveland, Ohio). The Veterans Administration (VA) dataset is composed of data acquired from multiple subjects. A variety of speeds is included, and the datasets have many consecutive strides. Within this section the methods of preparing both datasets for use as an evaluative measure and as control references will be detailed.

2.1 Cleveland Clinic Data Processing

The CC data used for this work had already been processed from its raw form to a set of vectors that held the time, knee moment, and knee angle associated with a single stride. As is expected of natural gait, it was non-periodic. Of primary interest beyond the given data was the velocity and acceleration of the knee joint. Thus a routine to derive this data without introducing noise was developed.

The original data was 55 samples long. To form a smooth representation of the data, spline curves could be fit to it. This was completed using the *spline* function in MATLAB, which uses cubic interpolation. Upon converting the raw data to splines, a matrix of coefficients is generated, four coefficients for each time step, of dimensions 54×4. Multiplying this matrix by

$$\begin{bmatrix} 0 & 3 & 0 & 0 \\ 0 & 0 & 2 & 0 \\ 0 & 0 & 0 & 1 \\ 0 & 0 & 0 & 0 \end{bmatrix}$$

yields the coefficients of the first derivative. Multiplying the coefficients of the first derivative by the matrix once more produces the second derivative coefficient matrix. It effectively reduces the order of the polynomial with each multiplication while multiplying the remaining coefficients by the value of their associated powers. The original (position), first derivative (velocity), and second derivative (acceleration) splines could then be evaluated at the desired time step size. The results are illustrated in Figure 3. As desired, by using this method there is no noise introduced. To complete the data set, the knee moment profile was processed by the same method, though no derivatives were taken; it is also shown in Figure 3
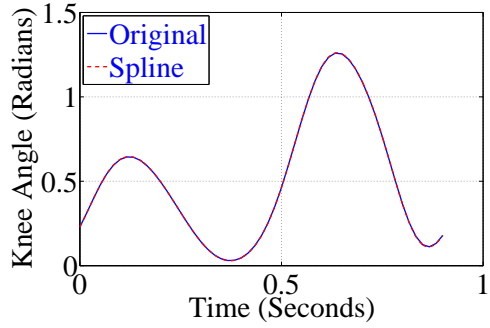
(a) CC original data and spline comparison
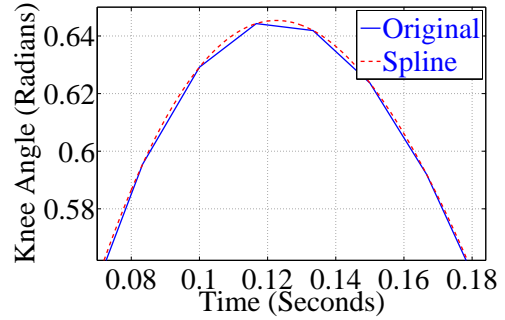
(b) CC original data and spline comparison enlarged at the first peak
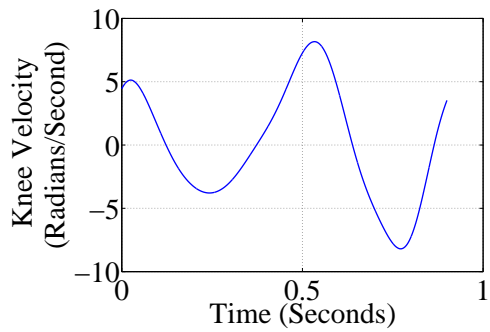
(c) CC spline first derivative
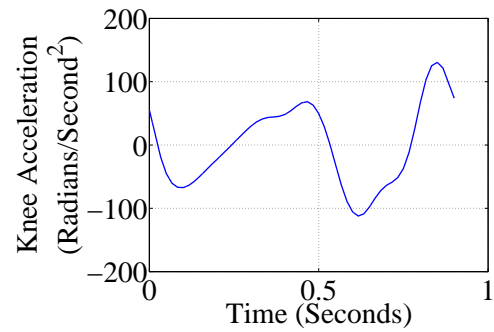
(d) CC spline second derivative
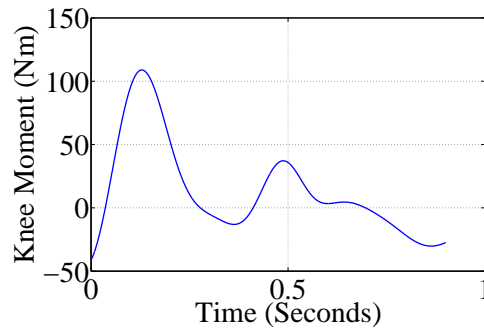
(e) CC spline moment data

Figure 3: Plots illustrating the CC data, the spline process, and the resulting derivatives

2.2 Veterans Administration Data Processing

For each trial the VA data was obtained in several forms, a marker and force plate file resulting from motion capture, preprocessed joint trajectory (position and velocity) files, a preprocessed file containing computed joint moments, and a preprocessed file of the calculated joint powers. Each of the preprocessed files were for a three-dimensional model. The usefulness of these files was limited, therefore, because this work is to be completed for a two-dimensional model. It was determined that the joint trajectories should be reevaluated in a two-dimensional framework. Several pieces of information in particular must be obtained. These include the dimensions of the subject, the joint trajectories, and a description of the heel and toe forward kinematics. The data for the left leg was selected arbitrarily for these computations.

2.2.1 Subject Dimensions

To begin the data analysis process, the subject dimensions must be determined from a standing trial. A marker set giving the global positions of the markers during standing was provided for each subject. Frequently when evaluating the leg in two dimensions, markers at the greater trochanter (GTRO), lateral epicondyle (LEK), lateral malleolus (LM), heel (HEE), and fifth toe metatarsal (MT5) are used as they sufficiently outline the subject's leg position; refer to Figure 4. Accordingly, these markers were used to determine the subject's dimensions.

Six dimensions are of interest in defining the subject's geometry. They are the length of the thigh (l_2), the length of the shank (l_3), the length of the foot from heel to toe (l_4), the distance from the ankle joint to the toe (aT), the distance from the ankle joint to the heel (aH), and the height of the ankle joint above the sole of
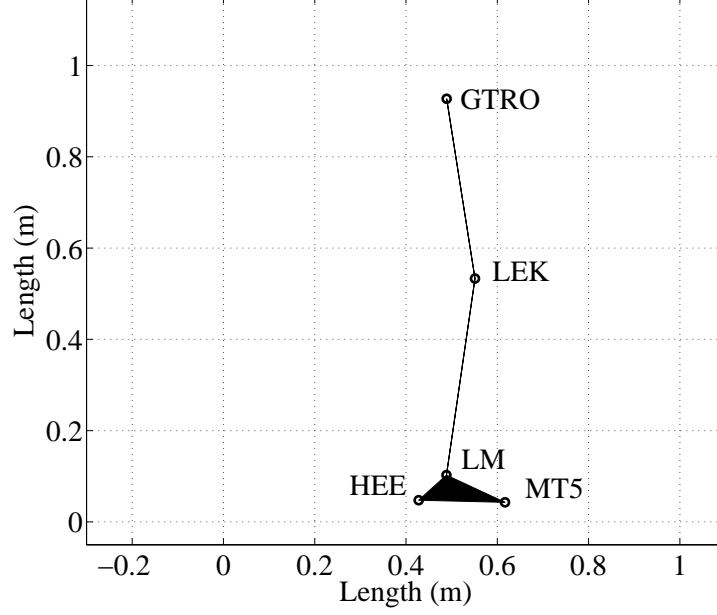
Figure 4: Marker placement for the leg

the foot (ah). These dimensions may be calculated by basic geometry.

$$l_2 = \sqrt{(LGTRO_x - LLEK_x)^2 + (LGTRO_z - LLEK_z)^2} \tag{2.1}$$

$$l_3 = \sqrt{(LLEK_x - LLM_x)^2 + (LLEK_z - LLM_z)^2} \tag{2.2}$$

$$l_4 = LMT5_x - LHEE_x \tag{2.3}$$

$$aT = \sqrt{(LLM_x - LMT5_x)^2 + (LLM_z - LMT5_z)^2} \tag{2.4}$$

$$aH = \sqrt{(LLM_x - LHEE_x)^2 + (LLM_z - LHEE_z)^2} \tag{2.5}$$

$$ah = LLM_z - \frac{LMT5_z + LHEE_z}{2} \tag{2.6}$$

The coordinate system for the global marker file is defined as x^+ anterior and z^+ up. The L preceding each marker name indicates that it is for the left side. Because the heel and toe markers were not consistently level, the average of the vertical coordinate for each of these is used in determining the height of the ankle joint.

11

2.2.2   Position Data by Inverse Kinematics

Inverse kinematics provides the means of extracting joint translations and rotations from motion capture marker data. In this case the vertical displacement and rotation of the hip joint, rotation of the knee joint, and rotation of the ankle joint are of interest. One method of solving motion capture data inverse kinematics is to use optimization. A two-dimensional form of the method presented in [51] was used to compute the inverse kinematics.

The global positions of the markers are known. A forward kinematics model of the subject is created, and a matching marker set is placed on the model. The joints of the forward kinematics model are then manipulated by the selected optimization algorithm until by some measure of cost the forward kinematics model markers are deemed close enough to the global positions recorded for the motion capture markers. This process is completed for each time step of the motion capture data, eventually providing a full set of joint trajectories. Within the next sections the forward kinematics model and optimization method will be developed for applying inverse kinematics to the VA datasets.

Forward Kinematics Model

The forward kinematics model for the VA data had to be addressed considering two cases. Some trials consisted of walking in one direction on the treadmill while others were reversed. This could be identified by the subject and marker set. The direction was consistent among the trials of Subject AB01, who also had a full body marker set recorded. All other subjects' trials were in the opposite direction and had only lower body marker sets recorded.

Local coordinate systems were defined for each segment of the leg. If the leg is visualized resting in a horizontal orientation with the hip joint to the left and the ankle joint to the right, each of the local coordinate systems may be simply defined

12
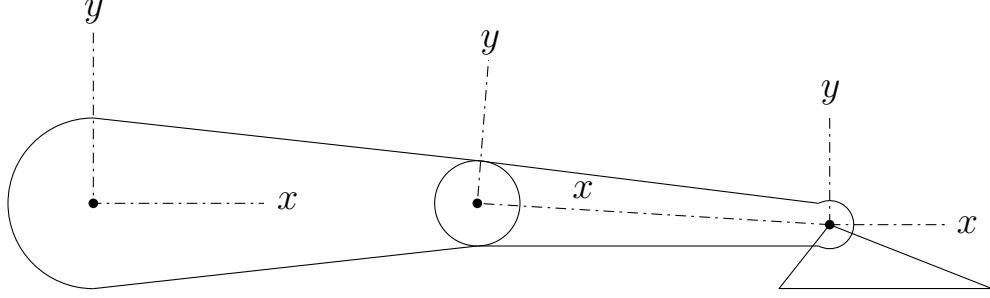
Figure 5: Local coordinate system assignment for forward kinematics

by placing their origins at the hip, knee, and ankle joints, pointing each x axis toward the next origin, and pointing each y axis perpendicularly upward, Figure 5. The case shown is for the direction traveled by Subject AB01. To be able to use the same model for the alternative case, the vertical orientation of the foot may be reversed while the coordinate systems remain in the same location and orientation.

To define any posture, the homogeneous transformation matrices for each of these coordinate systems must be developed.

$$T(T_x, T_y, \theta) = \begin{bmatrix} \cos(\theta) & -\sin(\theta) & T_x \\ \sin(\theta) & \cos(\theta) & T_y \\ 0 & 0 & 1 \end{bmatrix} \tag{2.7}$$

The inputs to (2.7) are a translation in the x direction T_x, a translation in the y direction T_y, and a rotation θ. Each of the leg segment coordinate systems may be described by using T.

$$T_{thigh} = T(Hip_{horiz}, Hip_{vert}, Hip_{rot}) \tag{2.8}$$

$$T_{thigh,shank} = T(l_2, 0, Knee_{rot}) \tag{2.9}$$

$$T_{shank} = T_{thigh} T_{thigh,shank} \tag{2.10}$$

$$T_{shank,foot} = T(l_3, 0, Foot_{rot}) \tag{2.11}$$

13

$$T_{foot} = T_{shank} T_{shank,foot} \tag{2.12}$$

Markers may now be placed in the frames that have been defined. The global coordinates of each marker are generated by multiplying the coordinates of the marker in the local coordinate frame by the related homogeneous transformation matrix.

$$f_{hip}(q) = T_{thigh} \begin{bmatrix} 0 & 0 & 1 \end{bmatrix}^T \tag{2.13}$$

$$f_{knee}(q) = T_{thigh} \begin{bmatrix} l_2 & 0 & 1 \end{bmatrix}^T \tag{2.14}$$

$$f_{ankle}(q) = T_{shank} \begin{bmatrix} l_3 & 0 & 1 \end{bmatrix}^T \tag{2.15}$$

$$f_{heel}(q) = T_{foot} \begin{bmatrix} -\sqrt{aH^2 - ah^2} & \mp ah & 1 \end{bmatrix}^T \tag{2.16}$$

$$f_{toe}(q) = T_{foot} \begin{bmatrix} \sqrt{aT^2 - ah^2} & \mp ah & 1 \end{bmatrix}^T \tag{2.17}$$

The sign of ah is selected based on the data set in use. For any trials related to Subject AB01, it is negative. For all other marker data sets it is positive. The positive case reverses the vertical orientation of the foot as was previously described.

Optimization

For this application the MATLAB function *fminsearch* was selected as the optimization algorithm. The cost function was defined as a sum of the squared residuals.

$$cost_{IK} = \sum_i \left(marker_i - f_i(q) \right)^2 \tag{2.18}$$

$marker_i$ represents the actual location of the markers, and $f_i(q)$ is the result of evaluating the forward kinematics model for marker i. An initial guess at approximately standing was supplied to the algorithm for the first frame $q = [0\ 1\ -\pi/2\ 0\ \pi/2]$. After the first frame the solution of the previous time step was used as the initial
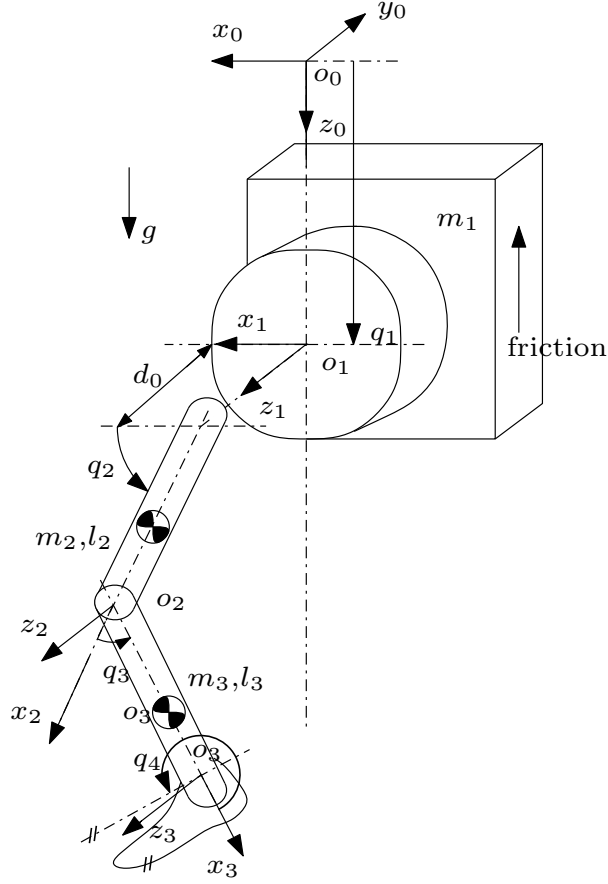
Figure 6: Coordinate system assignment for the Cleveland State University hip robot with prosthetic leg model attached. This figure was adapted from the originally published version in [37] from IFAC-PapersOnline, DOI 10.3182/20140824-6-ZA-1003.00332, 2014. Used with permission, Appendix L

guess for each consecutive time step.

2.2.3   Coordinate System Alignment

The final step in processing the position data is aligning the data resulting from the inverse kinematics computation with the coordinate system to be used in simulation. The coordinate system for the simulation was determined through application of the Denavit-Hartenberg convention for the Cleveland State University hip robot combined with a knee and ankle prosthesis. It is defined as shown in Figure 6. In all datasets the horizontal motion of the hip was discarded to match the constraints
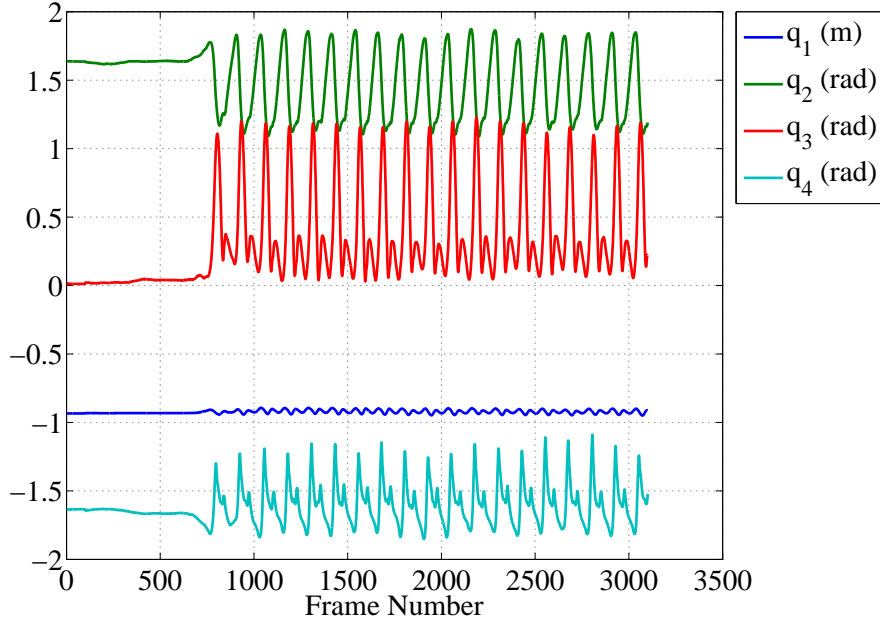
Figure 7: VA data trajectories for Subject AB01, Trial 003

of the robot. For the full body marker set cases all of the resulting inverse kinematics required a change of sign to align with the coordinate system of Figure 6. The lower body marker set cases required a reversal of the hip vertical displacement coordinate, which was identical to the full body set, the addition of π to the hip angle coordinate, and no changes to the remaining coordinates.

2.2.4 Velocity and Acceleration Data and Resampling

The computation of velocity and acceleration from the VA data was performed by the same method as described in Section 2.1. Prior to the spline fit and derivative process, however, the VA data's sampling frequency was reduced by a factor of 3. This decrease in the number of samples provided a smoother fit because every spline between points can increase the potential to fit the curve to fluctuations due to noise. The resulting splines, including the position data, were evaluated at the original sampling rate. Examples of the final trajectories for each of the joints after this process may be seen in Figure 7.
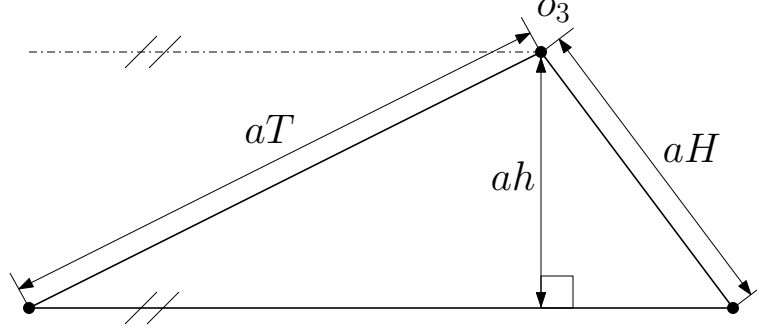
Figure 8: Foot dimension definitions and geometric relationships

2.2.5 Foot Kinematic Model

A triangular foot model was used throughout this work when ground contact was of interest. This model is depicted in Figure 8. One may see that the foot model connects to the sketch of the hip robot at the origin of the third coordinate frame. The heel and toe coordinates may be located in the world frame (zeroth frame) by kinematics. The forward kinematic equations for the x and z coordinates for both the heel and the toe were derived as follows. These will be required in Section 4.1

$$x_h^0 = l_2 \cos(q_2) + l_3 \cos(q_2 + q_3) + aH \cos\left(q_2 + q_3 + q_4 + \left(\frac{\pi}{2} + \cos^{-1}\left(\frac{ah}{aH}\right)\right)\right) \quad (2.19)$$

$$\begin{aligned} z_h^0 = q_1 + l_2 \sin(q_2) + l_3 \sin(q_2 + q_3) \\ + aH \sin\left(q_2 + q_3 + q_4 + \left(\frac{\pi}{2} + \cos^{-1}\left(\frac{ah}{aH}\right)\right)\right) \end{aligned} \quad (2.20)$$

$$x_t^0 = l_2 \cos(q_2) + l_3 \cos(q_2 + q_3) + aT \cos\left(q_2 + q_3 + q_4 + \left(\frac{\pi}{2} - \cos^{-1}\left(\frac{ah}{aT}\right)\right)\right) \quad (2.21)$$

$$\begin{aligned} z_t^0 = q_1 + l_2 \sin(q_2) + l_3 \sin(q_2 + q_3) \\ + aT \sin\left(q_2 + q_3 + q_4 + \left(\frac{\pi}{2} - \cos^{-1}\left(\frac{ah}{aT}\right)\right)\right) \end{aligned} \quad (2.22)$$

17

2.3   Discussion

In brief, two separate data sets were prepared for use throughout this work. The first set, the CC data, was composed of a single stride and required the processing of derivatives. A spline-based method was applied and velocity and acceleration determined. The second set from the VA included far more variety, ranging across subjects and speeds and including multiple strides. It was reprocessed to fit the two-dimensional requirement of this work. This included determining the dimensions of subjects from marker data, calculating inverse kinematics, and defining some necessary forward kinematics. The reference data is now formatted for use as a measure of comparison and controller tracking reference.

CHAPTER III

ACTUATOR SYSTEM DESIGN AND OPTIMIZATION

Unlike previous generations of prostheses, active prostheses require an actuator system. This system must comply with tight space constraints and generate a significant amount of torque as it supports the weight of nearly the entire human body for part of the gait cycle. In addition to these general requirements, the ultimate goals of natural movement and optimal energy regeneration must be addressed.

For this work the actuator system is considered as any component in the system starting from the joint of the prosthesis body up to and including the power source. Accordingly, this is composed of both a mechanical and an electrical subsystem. In this chapter the design methods for each of these systems is discussed followed by simulation of, optimization of, and results for the overall actuator. The crank-slider actuator is commonly modeled among prosthesis work. Also, supercapacitor-based regenerative actuating mechanisms have been studied [33, 34, 37]. However, emphasis on optimal energy regeneration through combining the crank-slider mechanism with an electrical system including a supercapacitor is original to this work. The chapter is concluded with a discussion.
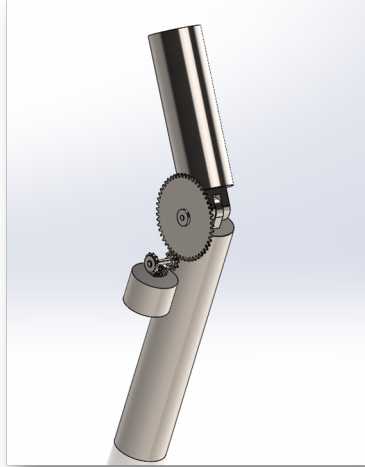
Figure 9: Three-dimensional schematic of a direct drive actuator

3.1   Actuator Modeling

When designing a powered prosthesis, the system that transforms the output of the motor to motion of the knee joint is an important consideration. One can identify two primary methods, a geared direct drive mechanism and a crank-slider mechanism, applicable to a knee joint. Within the broader context of powered prosthetics, it should be noted that both options may be applied to the ankle joint as well.

Figure 9 depicts a schematic form of the first case, a direct drive actuator. The only power transmission element between the motor and knee joint is the gearing. Alternatively, Figure 10 represents a basic crank-slider mechanism. Power transmission in this case is accomplished by combining a motor, ballscrew, and linkage with the knee joint.

A basic direct drive actuator model has been previously studied related to this work [33]. Therefore, the crank-slider design was selected for investigation for the sake of comparison and because of several notable features. Specifically, the crank-slider design can fit conveniently within the shape of a human shank; it is
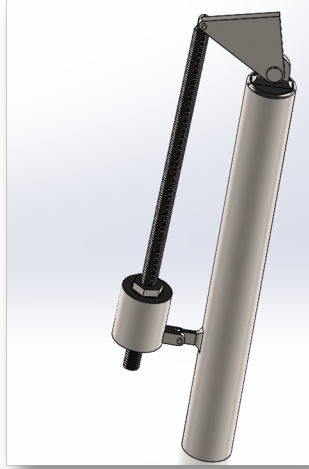
Figure 10: Three-dimensional schematic of a crank-slider actuator

compact. It is also a common form factor for prosthetics, making it possible to build upon some previous work. Examples of prostheses using this architecture include the Mauch SNS (passive), C-leg (passive with microcontroller), and Vanderbilt prototype (active) [19, 46]. The ballscrew and linkage combination provides a wide range of variables open to selection; this is of benefit because it offers multiple parameters for optimization. Lastly, this design mimics the leg's natural functioning as muscles apply linear forces rather than direct torques to joints.

Development of the crank-slider actuator model was completed in two stages. First, a proof of concept model mirroring a previous actuator model that included only a geared direct-drive motor was completed. This was then followed by an expansion of the crank-slider actuator model, integrating mechanical losses into the driving mechanism to better evaluate the actuator's capacity for energy regeneration.

3.1.1 Geometry and Kinematics

A symbolic expression describing the geometry, and thereby kinematics, of the crank-slider is required. By rotating the entire assembly shown in Figure 10, a convenient coordinate system for the crank-slider may be defined as shown in Fig-
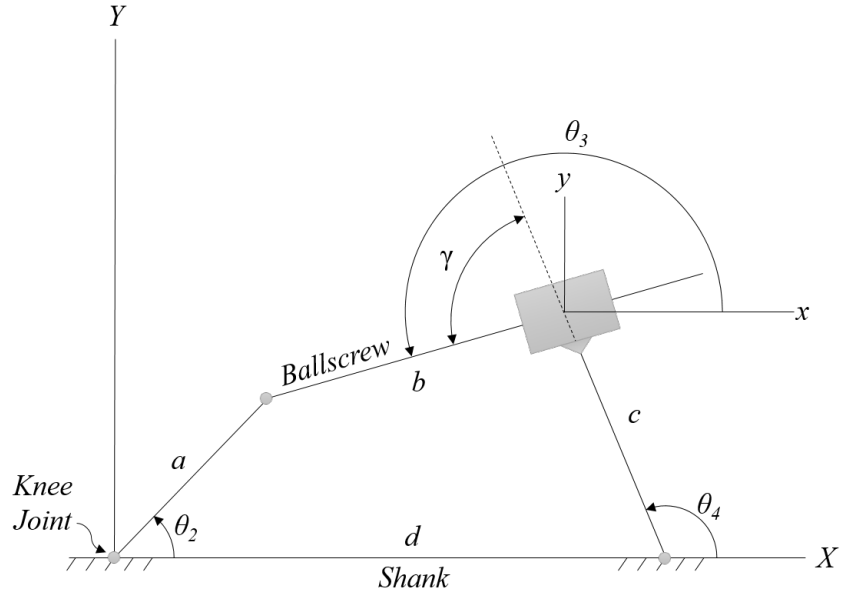
Figure 11: Geometry definitions used in deriving crank-slider kinematics

ure [11](navigation), which illustrates the relevant nomenclature and is based on [29]. Referring to the notation given in Figure [12](navigation), one can see that the flexion angle of the knee ϕ_k may be directly related to θ_2 by a constant angle ϕ_l, which is the angle at the knee joint of the triangular link.

$$\theta_2 = \pi - \phi_l - \phi_k \tag{3.1}$$
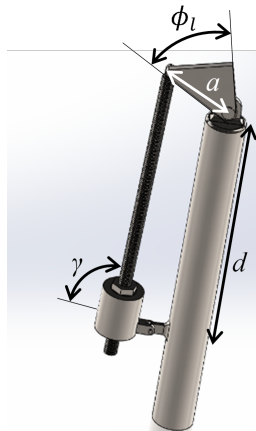
Figure 12: Notated three-dimensional schematic of crank-slider actuator

As further points of reference, a in Figure 11 is the side of that same triangular link that joins the shank to the ballscrew, and d is the length of the shank between the upper and lower crank-slider connection points.

Based upon Figure 11, loop equations for the x and y coordinates and a geometric constraint equation may be established.

$$a \cos \theta_2 - b \cos \theta_3 - c \cos \theta_4 - d = 0$$

$$a \sin \theta_2 - b \sin \theta_3 - c \sin \theta_4 = 0 \tag{3.2}$$

$$\theta_3 = \theta_4 + \gamma$$

Combining these equations and solving for θ_2 and b yields the following.

$$\theta_2 = \pi + \cos^{-1} \left(\frac{-a^2 + b^2 + 2bc \cos \gamma + c^2 - d^2}{2ad} \right) \tag{3.3}$$

$$b = \sqrt{a^2 - 2ad \cos \theta_2 + \frac{(c \cos \gamma)^2}{2} - \frac{(c \sin \gamma)^2}{2} - \frac{c^2}{2} + d^2)} - c \cos \gamma \tag{3.4}$$

Each of these equations will be utilized in the dynamic analysis, Section 3.1.2.

3.1.2 Dynamic Models

A representative dynamic model of the system is essential for optimization. Because the primary interest of this work is energy regeneration, a modeling approach based on power, which is easily integrated to evaluate energy, called bond graph modeling was selected [21]. Furthermore, the desired result, the charging of a supercapacitor, involves an interdisciplinary approach; the bond graph modeling method provides a straightforward means of combining the mechanical and electrical engineering fields. An overview of the bond graph approach is presented in Appendix A.

The bond graph modeling method is applied to the prosthesis actuator system in several forms. First, the basic model for comparison to the direct drive model
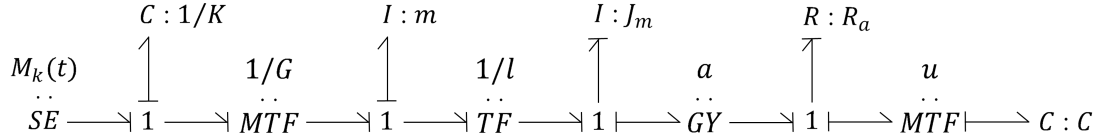
Figure 13: Bond graph representing the basic actuator system

is developed. This is followed by two expansions to incorporate mechanical losses. The first expansion involves the creation of a complex friction model for a selected ballscrew to observe the effects of mechanical losses on the prosthesis' energy regeneration capacity. The friction model is then generalized for use in optimization as the second expansion.

Basic Actuator

While formalized bond graph construction methods have been developed, the system of interest was constructed by inspection. The actuator model is shown in Figure 13. The input SE on the left is a knee torque profile. From left to right, the elements represent a torsion spring at the knee joint, crank-slider geometry, ballnut mass, ballscrew lead, motor inertia, motor constant, armature resistance, an ideal DC-DC power converter, and a capacitor. As can be seen in the figure, the modularity of the bond graph method makes it simple to divide the system into the mechanical and electrical subsystems for more detailed study and to expand the bond graph, modeling further details.

Dividing the system at the GY element, thereby dividing it into the mechanical and electrical subsystems, one may consider the model at a deeper level. Starting with the mechanical subsystem, the SE element represents the reference data discussed in Section 2.1. This knee moment data accounts for all dynamic interactions combined that apply torque to the knee joint. This is linked to a C element, representing a torsion spring, such that they share the same velocity. The next element represents the crank-slider linkage. Recalling that the model is based on the

conservation of power, it is most straightforward to find the modulus G by writing the power conservation equation across this element as follows:

$$P_{in, \ knee \ (rotary)} = P_{out, \ ballscrew \ (linear)}$$

$$T_2\dot{\theta}_2 = F_{ballscrew}\dot{b}$$

$$\text{know, } \dot{\theta}_2 = \frac{db}{dt}\frac{d\theta_2(b)}{db} = \dot{b}\frac{d\theta_2(b)}{db} \qquad (3.5)$$

$$\therefore F_{ballscrew} = \frac{d\theta_2(b)}{db}T_2.$$

This equation provides the required relationship, and the derivative $\dfrac{d\theta_2(b)}{db}$ is G, which is determined by taking the derivative of (3.3).

$$\frac{d\theta_2}{db} = \frac{b + c\cos\gamma}{ad\sqrt{1 - \dfrac{\left(-a^2 + b^2 + 2bc\cos\gamma + c^2 - d^2\right)^2}{4a^2d^2}}} \qquad (3.6)$$

In addition to being used as the transformer modulus, the value of G describes the instantaneous mechanical advantage of a given linkage.

The next several elements represent the ballscrew. First, the I element stands for the ballnut's linear inertia as it moves along the screw. Secondly, a transformer is used to represent the change from linear motion to rotation. The denominator of the modulus is the lead of the screw. Lastly, the rotational inertia element is included in the mechanical subsystem. Within the model developed here, it represents the motor inertia. The inertia of the ballscrew may also be added.

The transition to the electrical subsystem occurs at the GY element. The modulus of this element is the motor torque constant. The circuit represented in the bond graph is shown in Figure 14. A R element is placed in series with the motor to represent the armature resistance. The DC-DC power converter is integrated into the bond graph by use of an MTF element for which the transformer modulus is a
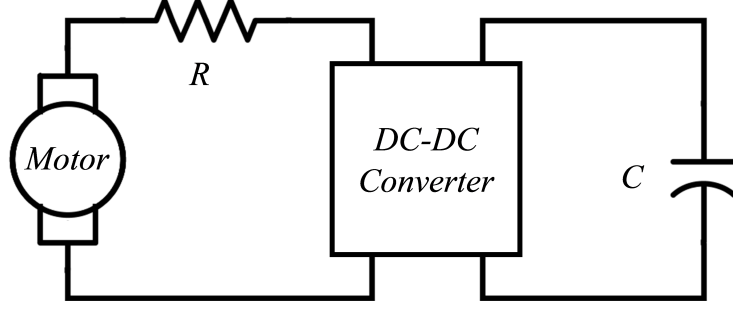
Figure 14: Circuit representing motor and electronics

value labeled u, which will be further discussed in Section 3.2. Lastly, a C element represents one of the keys to the system, the supercapacitor energy storage device.

The causality assignment was such that the system state variables were the knee velocity, motor momentum, and capacitor current. A through power convention was also established. Consequentially, all elements will indicate power exiting the system when the product of effort and flow is positive except the SE, which is the opposite. The detail of deriving the system differential equations for simulation is shown in Appendix B. The final result is given below:

$$\dot{\phi}_k = Gl\dot{\theta}_m \tag{3.7}$$

$$\ddot{\theta}_m = \frac{1}{J_m + ml^2}\left(lGM_k(t) - lGK\phi_k - \frac{\alpha^2}{R}\dot{\theta}_m + \frac{\alpha u}{RC}q_C\right) \tag{3.8}$$

$$\dot{i}_C = \frac{\alpha u}{R}\dot{\theta}_m - \frac{u^2}{RC}q_C \tag{3.9}$$

where ϕ_k is the knee angle, θ_m is the motor angle, q_C is the capacitor charge, and i_C is the capacitor current.

Actuator with Complex Friction Model

Because the model of the basic actuator system is general for optimization with the focus being placed on regeneration capacity, only the lead of the ballscrew is being modeled as this incorporates both the kinematic and kinetic transformations

26

that this element implies. This is only one parameter that defines a ballscrew; the remainder of the parameters, diameter, length, and preload among others, have been left to be determined during future mechanical design beyond the scope of this work. Accordingly, the ability to model mechanical friction is limited because few details of the screw are known; however, to accurately consider the actuator's potential for energy regeneration, the mechanical losses must be estimated.

To address this challenge, a test case could be evaluated. An optimal set of parameters can be determined with the basic actuator model, which is frictionless. Within this parameter set a ballscrew lead value would be specified. A specific ballscrew with this lead value could then be selected based on guidelines given by ballscrew manufacturers and a complex friction model developed from the screw's now known parameters. This model can be simulated for a given parameter set, providing insight into friction's effects on the system's power flow and energy usage.

Friction modeling within a ballscrew has been a topic of much study ranging from the development of highly complex models to the simplest efficiency accounting. Complex models of a ballscrew system includes variables such as rolling contact, lubrication, sliding, ball-to-ball contact, and the return system, among others, such as in [30]. Simplifications modeling only a portion of these effects have been established. For example, in [47] the model was based primarily on bearing-related effects. Considering the problem from a general perspective, it has been modeled with modification as a basic screw as well [42]. Experimental modeling has also been applied to this problem [20]. Selecting from among these options is really dependent on the accuracy required for the application and the available information. For this work, reaching a good balance between accuracy and available information, the method discussed in [42] has been selected.

The addition of a complex friction model requires that another R element be integrated into the actuator bond graph. According to [42], the friction of a ballscrew
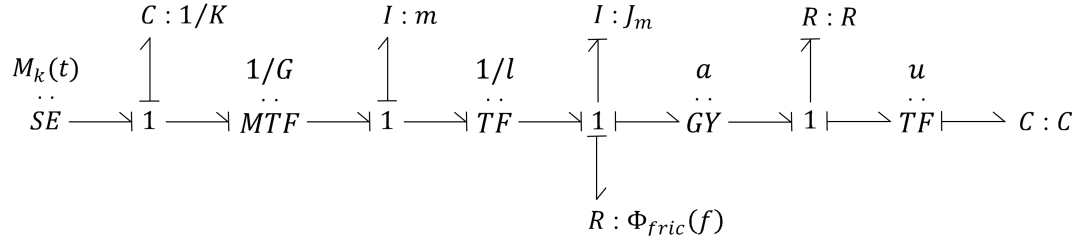
Figure 15: Bond graph incorporating nonlinear R element that represents a complex friction model for the ballscrew

is greatly dependent on the preload of the ballnut and primarily of the Coulomb type.

$$\Phi_{fric}(f) = |\tau_{fric}| \operatorname{sign}(f) \tag{3.10}$$

Φ_{fric} is a function of the incoming flow, angular velocity in this case, alone because of the sign function. The addition of this function to the bond graph is illustrated in Figure 15. It can be seen that this change to the bond graph does not change the state variable definitions or add an algebraic loop, which would be indicated by indefinite causality.

Due to the friction being primarily associated with the preload and composed of the Coulomb form, the friction torque could be represented by the equation typically describing the torque to raise or lower a load with the force F_P set equal to the preload rather than axial load force.

$$\tau_{fric} = F_P R_{pitch} \left(\frac{2\pi R_{pitch}\mu \pm l\cos\alpha}{2\pi R_{pitch}\cos\alpha \mp \mu l} \right) \tag{3.11}$$

In addition to the preload, the pitch radius R_{pitch}, friction coefficient μ, screw lead l, and thread angle α must be known. For a high-precision ballscrew with a light preload in the ballnut a value of $\mu = 0.005$ may be used for the coefficient of friction. Additionally, the thread angle α for a ballscrew is 45° [42]. The remaining parameters are dependent on the geometry of the specific ballscrew being considered. The first set of signs given in (3.11) is for extension of the screw while the second set is for

compression.

Once again deriving the system equations in an algorithmic manner, the final system describing the expanded model may be determined.

$$\dot{\phi}_k = Gl\dot{\theta}_m \tag{3.12}$$

$$\ddot{\theta}_m = \frac{1}{J_m + ml^2}\left(lGM_k(t) - lGK\phi_k - \frac{\alpha^2}{R}\dot{\theta}_m + \frac{\alpha u}{RC}q_C - \Phi_{fric}\left(\dot{\theta}_m\right)\right) \tag{3.13}$$

$$i_C = \frac{\alpha u}{R}\dot{\theta}_m - \frac{u^2}{RC}q_C \tag{3.14}$$

The details of this derivation are contained in Appendix D; it follows the derivation of the frictionless system closely.

Actuator with Generalized Friction Model

Alternatively, and perhaps most commonly, the frictional losses of a ballscrew can be modeled by a simplified method, accounting for the efficiency of the screw which is stated by manufacturers to be about 90% [26]. The ballscrew friction model developed by Olaru, et al. has shown close agreement with this value for a variety of speeds and a range of contact loads, indicating the sufficiency of this method for optimization purposes [30]. The results of the complex friction model should also provide confirmation of this approach. Accounting for this efficiency figure in the dynamic model provides a second means for modeling the ballscrew's friction. Most importantly, this approach is feasible for optimization as it is not dependent on screw parameters beyond the lead l.

Applying this concept to the basic transformer model shown for the ballscrew in Figure 13 requires a loss of the power conservation property of the bond graph as illustrated in general terms for the case where the screw is converting power in the

29

mechanical rotation domain to power in the mechanical translation domain and $\eta < 1$.

$$F_{screw}\dot{x} = \eta\tau_{screw}\dot{\theta} \tag{3.15}$$

The equations describing a ballscrew within a bond graph are separated into the kinematic relationship and kinetic relationship, (3.16) and (3.17), respectively.

$$\dot{\theta} = \frac{1}{l}\dot{x} \tag{3.16}$$

$$\tau_{screw} = lF_{screw} \tag{3.17}$$

Using these equations to substitute back into the right-hand side of the power equality given in (3.15), one can see that the efficiency coefficient must only be applied to either (3.16) or (3.17). Since the friction torque is a kinetic variable, it follows that the efficiency coefficient should be applied to (3.17).

$$\tau_{screw} = \eta lF_{screw} \tag{3.18}$$

It cannot simply be said, however, that (3.18) always holds true as it is possible for the screw to be driven by the force, backdriving.

$$F_{screw} = \eta\frac{1}{l}\tau_{screw} \tag{3.19}$$

For the power equality to hold for both of these cases and the equations to be of the form (3.17) as implemented in the bond graph, the coefficient η cannot simply be set to 0.9, though the efficiency is always 90%. The solution to this is to use the equation of the form (3.18) where two values of η are switched between. The first is obvious: $\eta_F = 0.9$ for the case where the force is driving the screw. The second is found by solving (3.19) for τ_{screw}. This requires $\eta_\tau = \frac{1}{0.9}$ and is for the case where the torque

30

is driving the screw.

Replacing (3.17) in the bond graph system equation derivation process with the form (3.18) leads to a slight alteration of the second equation of motion of the original set of equations. The complete set is shown below with the addition of the efficiency term.

$$\dot{\phi}_k = Gl\dot{\theta}_m \tag{3.20}$$

$$\ddot{\theta}_m = \frac{1}{J_m + ml^2\eta}\left(\eta lGM_k(t) - \eta lGK\phi_k - \frac{\alpha^2}{R}\dot{\theta}_m + \frac{\alpha u}{RC}q_C\right) \tag{3.21}$$

$$i_C = \frac{\alpha u}{R}\dot{\theta}_m - \frac{u^2}{RC}q_C \tag{3.22}$$

The derivation of (3.20)-(3.22) is detailed in Appendix E.

3.2   Open-Loop Control

Because it would mirror the control of the direct drive system of [33] and provide accurate tracking of reference data, an open-loop controller was selected for testing the regenerative capacity of the system in simulation. The open-loop controller was designed using semi-active modulation for this portion of the work. This system fits the framework for a semi-active system in that the actuator is not directly controlled by an external source, rather, a system variable, u in this case, is modulated to control the flow of power to the actuator from a storage device, namely a supercapacitor.

To determine u, the equations of motion were manipulated such that a direct solution was possible based on reference data. The general case of this method, termed "u-inversion," is established in [35]. The procedure is shown in Appendix C for the basic crank-slider actuator model. The inversion process has been omitted for the remainder of the actuator models because it is identical for each case with the exception of the final step, which is easily derived.

3.3 Simulation, Optimization, and Results

In this section the simulation and optimization methods and results of each actuator model developed in Section 3.1.2 will be presented. Due to their consecutive dependencies, the simulations, optimizations, and results will be grouped according to model. Additionally, biogeography-based optimization, the optimization algorithm selected for this work, will be discussed both theoretically and in application within this section.

3.3.1 Basic Actuator

Simulation of Basic Actuator Model

The basic actuator model was developed in Simulink by implementing the system equations (3.7)-(3.9) in block diagram form. An embedded MATLAB function was used to contain the equations of the transformer modulus G. The input to the system was the knee moment profile from the single stride CC data discussed in Section 2.1.

In keeping with the parameters of the original direct-drive proof of concept model, the parameters from the same motor datasheet, a Maxon RE 65, were used. Because the ballscrew is an optimized element, the mass of the motor was substituted for the value of the mass of the ballnut. Lastly, the link length c was set to zero, reducing space requirements. Each of these parameters are detailed in Table I. The remainder of the parameters were optimized and will be discussed in the following sections on optimization.

Optimization of Basic Actuator Model

Optimization of the basic actuator model was completed to prove the potential for a crank-slider actuator to successfully charge a capacitor. The optimization

Parameter	Symbol	Value	Units
Motor Constant	α	0.054	Nm/A
Armature Resistance	R	0.0821	Ohm
Motor Inertia	J_m	1.29×10^{-4}	kg m^2
Estimated Nut Mass	m	2.1	kg
Link Length	c	0	m

Table I: Fixed parameters for all actuator models

was accomplished with the biogeography-based optimization algorithm, which will be described next. This is then followed by the detail of the application of biogeography-based optimization to this particular problem.

Biogeography-Based Optimization Biogeography-based optimization (BBO) is an algorithm based upon the migration and emigration of species to and from various isolated habitats where the habitats represent problem solutions and species characterize solution features [40, 41]. In nature each isolated habitat can be labeled with an associated habitat suitability index (HSI), an overall measure of its ability to support species. The HSI is dependent on a variety of suitability index variables (SIV). Within the study of biogeography the SIV's correspond to features of a habitat such as the amount of vegetation, availability of water, climate, and other factors.

Logically, if a habitat has a high HSI, it can support a greater number of species and will, therefore, have a higher emigration rate, meaning that many species will spread from the high HSI habitat to surrounding habitats. In addition, a high HSI habitat will have a low immigration rate because it is so populated; most new species will not have access to the necessary resources.

Transferring these general ideas to the solution of an optimization problem, one can correlate each isolated habitat with a single candidate solution. The HSI is a measure of candidate solution's fitness. Similarly, the SIV's correspond to features of that candidate solution. Immigration λ and emigration μ rates are determined

33

Parameter	Value
Population Size	200
Number of Generations	100
Number of Elite Individuals	2
Probability of Mutation	0.02

Table II: Biogeography-based optimization parameters used for optimization of the actuator models

probabilistically and provide the means of sharing information between solutions. The emigration rate determines whether or not a solution feature will be shared with another habitat, and the immigration rate is used to select the future location of the solution feature.

Beyond the basics of natural biogeography, two features are added to the algorithm used in this work, mutation and elitism. Mutation is determined probabilistically and set at a low rate such that new information may be added, reducing the chance of the algorithm finding a local minimum, yet it does not become a random search. To implement elitism the best candidate solutions are passed from generation to generation; in this way the best solution of the consecutive generation will be no worse than that of the previous generation.

Application of BBO to Basic Actuator Model Multiple optimization runs were completed with the algorithm parameters given in Table II. A relevant cost function was defined.

$$Cost = -(q_{C,final} - q_{C,initial}) \qquad (3.23)$$

Because BBO seeks to minimize the cost function and the goal is maximization of the capacitor charge for one gait cycle, a negative sign is introduced. While maximization of energy gain is more applicable, this cost function based on maximizing the capacitor charge was selected to remain consistent with the original simulation [33].

The optimized parameters were selected as shown in Table III, which also

Parameter	Minimum Value	Maximum Value	Units
C	0	500	F
K	0	100	Nm/rad
a	0	0.15	m
d	0	0.3	m
γ	0	π	rad
ϕ_l	0	π	rad
l	1	6.350	mm/rev
q_{C0}	0	8000	C

Table III: Optimization parameter ranges for the actuator models

includes the search spaces. All of the parameters were allowed to vary throughout a continuous search space except for the ballscrew lead l for which a discrete set was defined. This set consisted of the following values in mm/rev: 1, 1.25, 2, 2.5, 3, 4, 5, 5.08, 6, and 6.35. All values greater than and including 2 mm/rev are expected to represent a backdrivable screw [49].

Lastly, several constraints were placed on the acceptable solutions to help ensure basic feasibility. This was implemented through penalizing the cost function of any solution not meeting the constraints by setting it to infinity. Specifically, the geometry variables were required to result in real values for the variable length link b (ballscrew) and for the transformer ratio G. Additionally, solutions for u resulting from the u-inversion process were required to be real and between negative one and one.

Results

Though multiple solutions were found following several optimization trials that resulted in an increase in capacitor charge, one example set of results is provided for the basic actuator model. Several considerations went into determining when a sufficient set of parameters had been selected by the optimization algorithm as the methods utilized do not guarantee global optima. These basic conditions were applied for each case of optimization throughout this work. First, an intuitive sense

Parameter	Symbol	Value	Units
Capacitance	C	221.54	F
Spring Constant	K	47.64	Nm/rad
Link Length	a	0.055	m
Link Length	d	0.25	m
Angle	γ	1.32	rad
Angle	ϕ_l	1.17	rad
Screw Lead	l	5.08	mm/rev
Initial Capacitor Charge	q_{C0}	6726	C

Table IV: Example set of optimization results for the basic actuator model

for the capacity of the optimization was obtained through completing a number of trials during the development of each model. Secondly, trials were performed with the finalized model and any cost trends observed. Finally, as long as the algorithm did not seek to exceed any of the parameter ranges and the cost functions were within a relative measure of magnitude, the best cost solution was typically selected.

The parameters selected by the optimization algorithm are given in Table IV. Each of these values are within feasible ranges. Figure 16 illustrates the minimum value of the cost function from generation to generation. By 100 generations no visible improvement has occurred in the cost function within the last forty generations, indicating that this is a more than sufficient number of generations for this optimization problem.
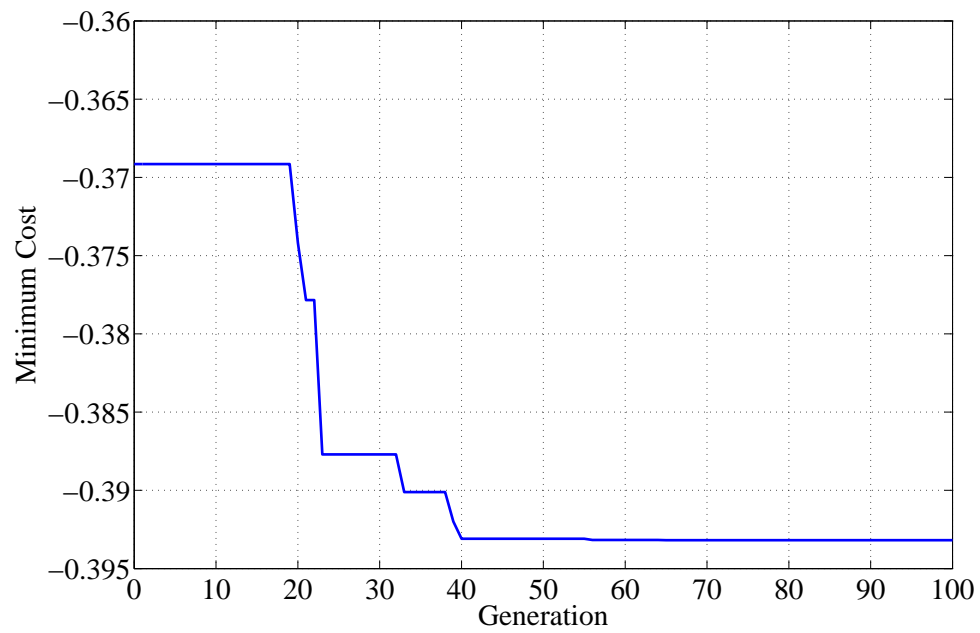
Figure 16: Progression of the minimum cost for an optimization run for the basic actuator model for a single gait cycle
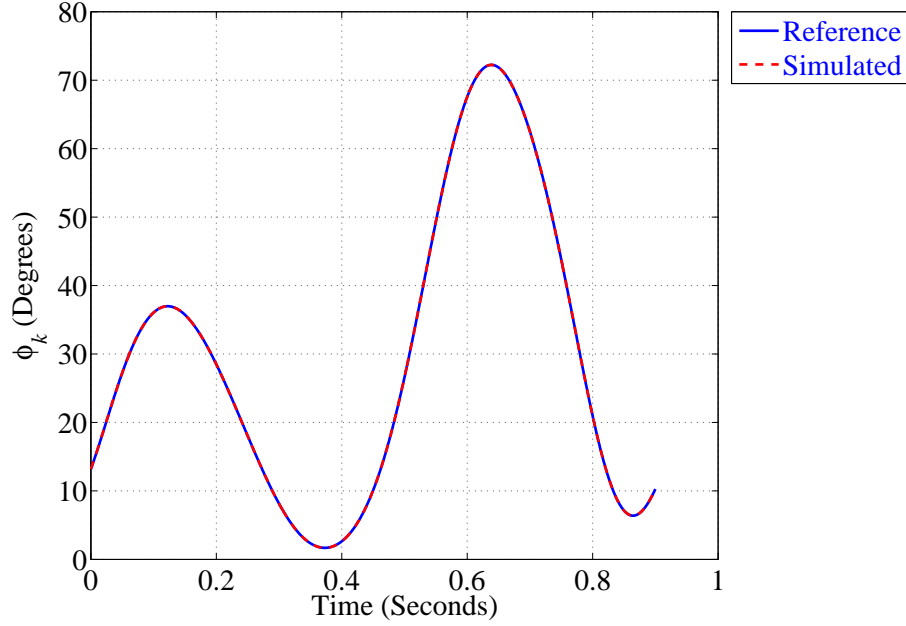
Figure 17: Tracking performance of basic actuator model for single gait cycle

Mathematically perfect tracking is shown in Figure 17, indicating that the open loop control method was successful. The total RMS error comparing the simulated knee angle to the reference data

$$RMS_{total} = \sqrt{\sum_i \left(\phi_{k,i,ref} - \phi_{k,i,sim}\right)^2} \qquad (3.24)$$

was 7.52×10^{-5} rad. The electrical attributes of this trial for the complete stride may be seen in Figures 18a–18c. For this set of parameters the capacitor charge increased by 0.3932 C, and the energy increased by 11.94 Joules.
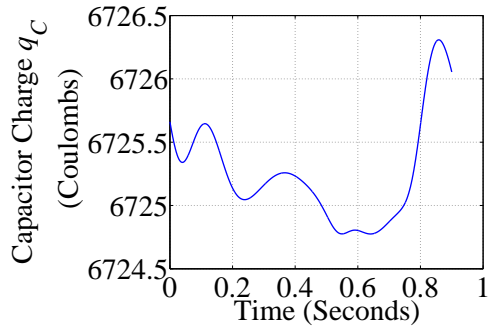
(a) Capacitor charge over one gait cycle. An overall gain is observed.
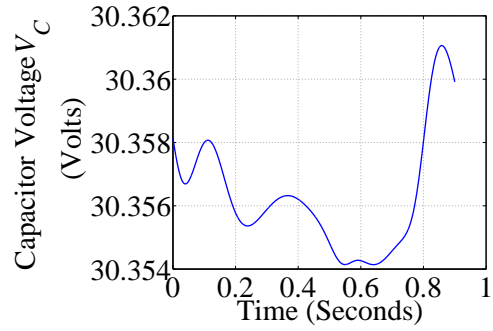
(b) Capacitor voltage over one gait cycle. A slight increase in voltage is indicated
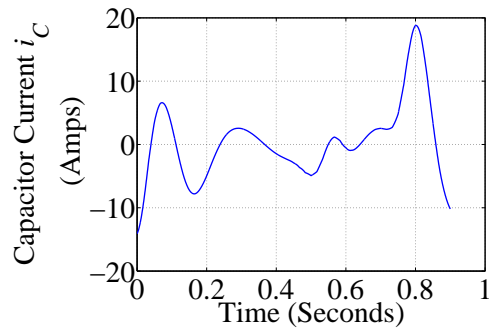
(c) Capacitor current over one gait cycle

Figure 18: Plots illustrating behavior of the basic actuator model electrical system over one gait cycle

3.3.2 Complex Friction Actuator

Having shown that the crank-slider actuator at a basic level is capable of energy regeneration, a model including friction at the ballscrew is to be simulated. After describing the simulation, the results for the complex friction actuator model are presented.

Simulation of Complex Friction Actuator Model

The complex friction actuator model simulation was created by using the fixed parameter set and the parameter set identified during optimization of the basic actuator model, Tables I and IV. To complete the model detail required for simulation, an actual ballscrew must be identified. The selection of a ballscrew is primarily dependent on the axial load. An equation expressing the axial load of the ballscrew may be derived as implied by the bond graph:

$$F_{axial} = \frac{1}{l}\left(\left(ml^2 + J_m\right)\ddot{\theta}_m + \frac{\alpha^2}{R}\dot{\theta}_m - \frac{\alpha u}{RC}q_C\right). \tag{3.25}$$

This equation can be evaluated with the parameters of the presented basic actuator system simulation results.

Upon evaluating (3.25), the peak force was extracted. The value determined was $F_{axial} = 1421$ N ≈ 320 lbf. Coupled with the value of the screw lead, 0.2 in/rev or 5.08 mm/rev, this information was sufficient to select a ballscrew as it also defined the required preload value. The optimal preload value is 10% of the maximum force according to [42]. This is a value of $F_P = 142.1$ N ≈ 32 lbf. The selected screw must be capable of having this preload applied.

A search was conducted among several ballscrew manufacturers. The final selection was a PowerTrac 0631-0200 SRT RA screw and SEL 10408 nut assembly from

Nook Industries [18]. The datasheet for this product can be found in Appendix F. This screw is able to handle a dynamic load of up to 815 lbf and preloads up to 233 lbf, and it possesses the required lead. While a ballscrew does not have a pitch radius as defined in the typical sense for power screws or gears, the ball circle radius is a reasonable approximation [17]. For the Nook Industries screw the ball circle radius was $R_{pitch} = 0.00801$ m.

Simulink was used to create the system simulation. This was implemented by constructing the system equations in block diagram form. While no optimization was intended for this simulation, it was developed within the same framework as the basic actuator simulation such that optimization could be possible if required in the future given further development. Additionally, a specialized function was used to implement the friction model. Within a MATLAB embedded function block logic was assembled to provide switching between the screw extension and compression variations of the friction torque equation and to apply the sign function.

Lastly, auxiliary MATLAB code was developed and additional blocks were added to the Simulink diagram to track the power flow and energy usage of the system. Alongside a general energy accounting an efficiency term for the ballscrew was calculated. A sum of the power entering and a sum of the power exiting the 1-junction connecting the friction R element to the bond graph, excepting the power entering the friction R element, were computed. These were integrated to determine the total energy entering and exiting the junction. Division of the exiting energy value by the entering energy value produced an efficiency term for the ballscrew. One item of note within the energy balance software inconsequential to the final results is discussed in Appendix G.
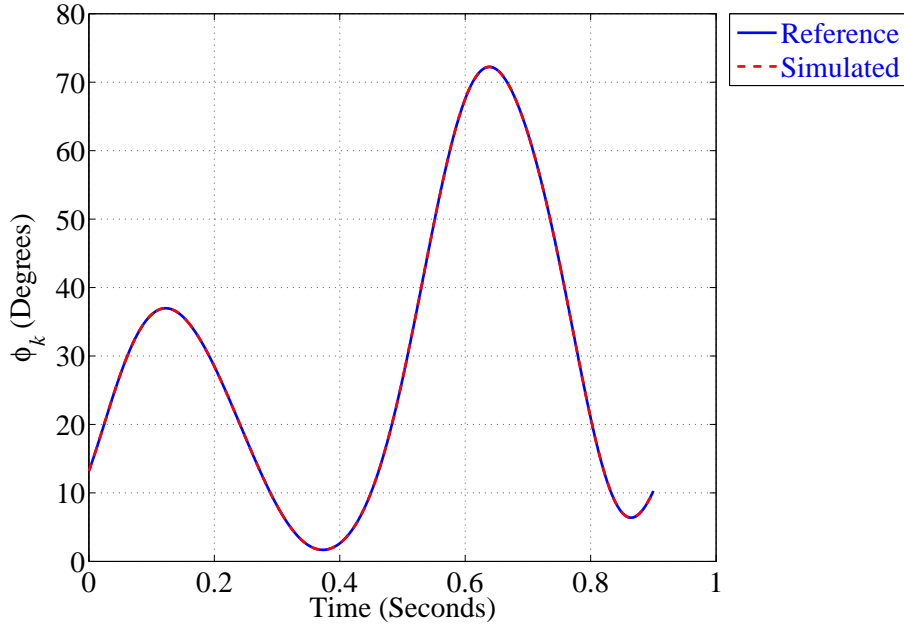
Figure 19: Tracking performance of complex friction model for single gait cycle

Complex Friction Actuator Model Results

The simulation was run using the CC dataset for the input reference knee moment with a length of one stride. Mathematically perfect tracking as predicted by the u-inversion technique was attained, as shown in Figure 4. The total root mean square value obtained, equation (3.24), was 7.9578×10^{-5} rad.

The attributes of the electrical system throughout the simulation time are depicted in Figures 20a–20c. With the inclusion of the friction losses the capacitor still charged for the given parameter set. Over one full stride a gain of 0.2620 C was observed.
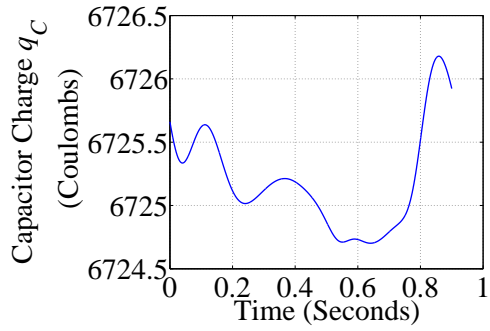
(a) Capacitor charge over one gait cycle. An overall gain is observed.
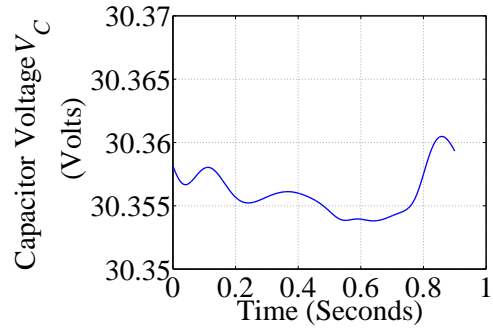
(b) Capacitor voltage over one gait cycle. A slight increase in voltage is indicated
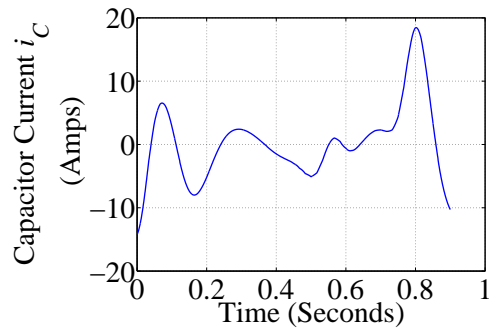
(c) Capacitor current over one gait cycle

Figure 20: Plots illustrating behavior of the complex friction model electrical system over one gait cycle
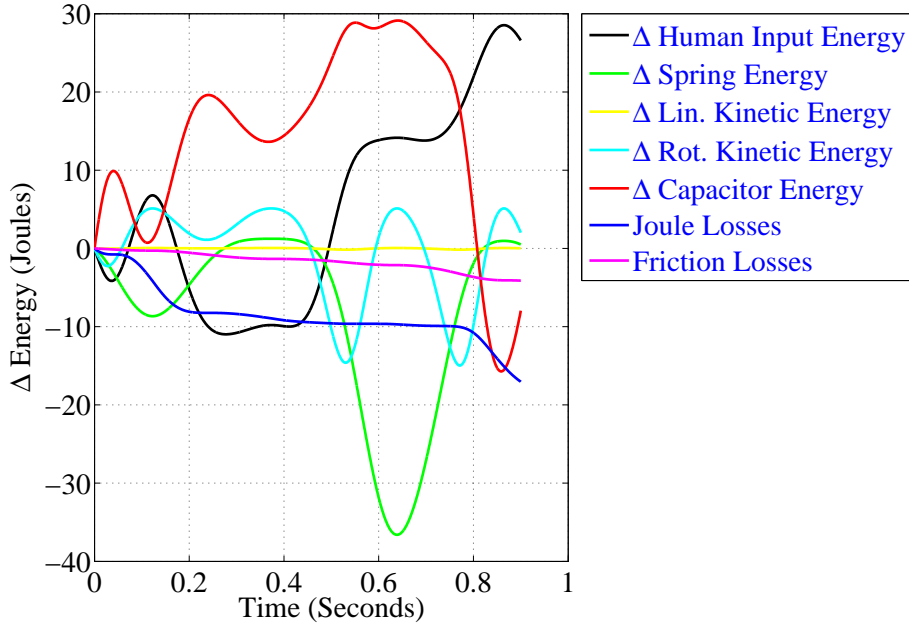
Figure 21: Plot illustrating the change in energy of each component of the complex friction model. For the given sign convention a negative change in energy corresponds to energy gained by a component

The change in energy for each component was also evaluated and is shown in Figure 21. The sum of the final values of each component's change in energy was on the order of 10^{-6}, confirming that the system model is truly energy conserving. An overall gain of 7.95 J was observed in the capacitor. The net available energy entering the system from the human was 26.58 J. The capacitor stored energy represents approximately 30% of this available energy. It can also be noted that the losses related to the motor resistance were two to three times greater than the friction losses, suggesting that this may be an important area to investigate with respect to the overall actuator's efficiency.

The plot of power flow in Figure 22 shows an alternating pattern between the power provided and required by the human and the power delivered to and extracted from the capacitor. This illustrates the power exchange expected for regeneration.

Finally, the efficiency of the ballscrew actuator was evaluated, Figure 23.
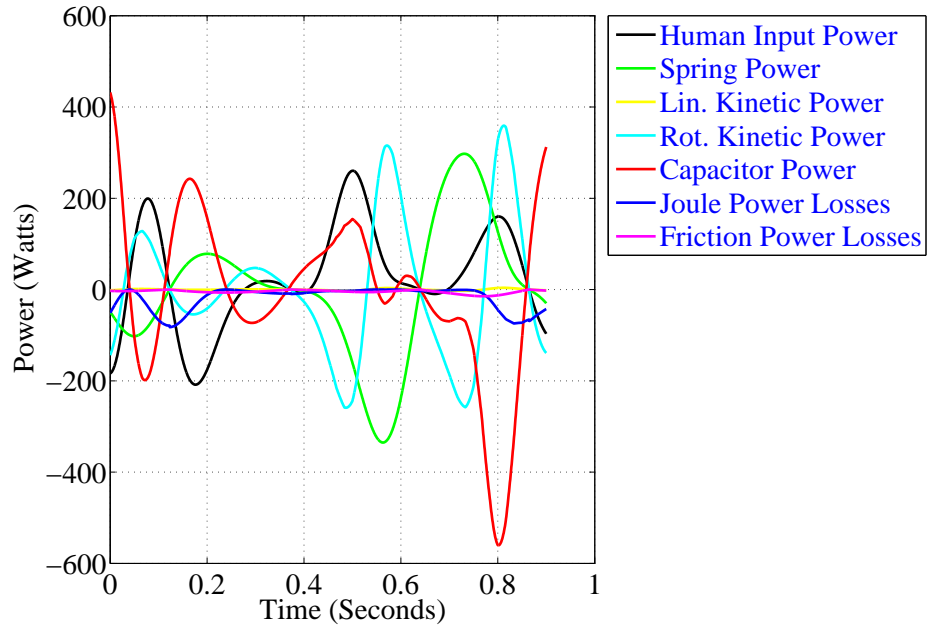
Figure 22: Plot illustrating the power of each component of the complex friction model. For the given sign convention a positive value corresponds to power entering the bond graph body, thereby exiting a component

At its lowest point the efficiency of the screw was 97%. This suggests that the manufacturer's value of 90% is more than sufficient in accounting for the friction losses. However, it should be noted that the efficiency is dependent on the preload of the ballscrew. While large variations in the required value of the preload are not expected for different screws, further trials for different parameter sets would be required to determine the range of this variation.
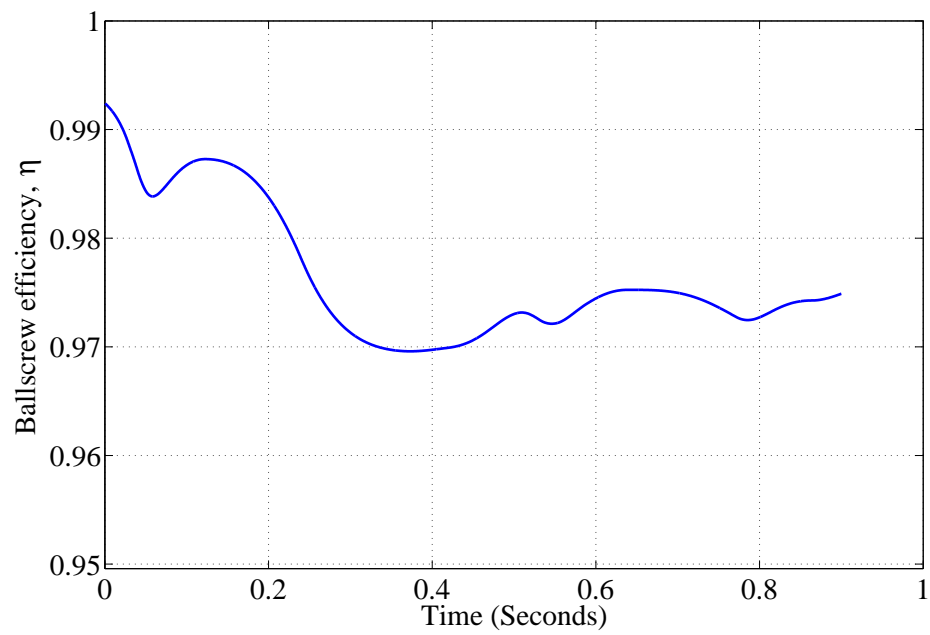
Figure 23: Efficiency of the ballscrew within the complex friction actuator model simulated over one gait cycle

3.3.3 Generalized Friction Actuator

Having confirmed that the efficiency of the ballscrew is no less than 90% by evaluating a more complex model of the ballscrew, it is reasonable to assume the manufacturer's given efficiency value of 90% to simplify the model. This simplification makes optimization more feasible. It provides a means of creating an actuator model that may be optimized yet will represent the frictional losses within a safe margin of error. Within this section the simulation implementing the generalized friction actuator model will be presented. This model will then be optimized. To conclude, the results of this optimization will be presented.

Simulation of Generalized Friction Actuator Model

Similar to the simulation developed for the complex friction actuator model the system equations were implemented in block diagram form. An embedded MATLAB function was prepared for the selection of η. Based on the power convention of the bond graph, the switching was defined such that $\eta = 0.9$ would be selected for positive power flow through the ballscrew TF element, corresponding to backdriving, and $\eta = \dfrac{1}{0.9}$ would be selected for negative power flow, in which case the screw is being driven by the torque. The value for η must be initialized due to requirements of the simulation software. Because in the general case it is unknown which state the simulation will begin in, the initial value for η was selected to be one, fully efficient

Code for an energy balance was completed for this model as well as calculation of the efficiency across the ballscrew TF element. While the system energy would no longer balance because of the non-power conserving change made to the system equations, the difference will represent the losses due to the screw's friction torque. In addition, dividing the time integral of the input power of the TF by the time integral

	Optimized System Parameters								Capacitor Charge Gained (C)	Capacitor Energy Gained (J)	Friction Losses (J)
	C (F)	K (Nm/rad)	a (m)	d (m)	γ (rad)	ϕ_l (rad)	l (mm/rev)	q_{C0} (C)			
Trial 1	122.89	32.32	0.061	0.30	0.49	1.32	5	4078	0.056	1.85	9.67
Trial 2	140.82	31.16	0.091	0.23	2.43	1.35	2	4503	0.060	1.92	9.58
Trial 3	70.39	32.18	0.061	0.30	0.58	1.32	5	2332	0.056	1.85	9.66
Trial 4	117.40	32.15	0.062	0.30	2.26	1.33	5.08	3933	0.055	1.84	9.66
Trial 5	151.62	30.69	0.036	0.29	2.71	1.28	3	4930	0.060	1.94	9.53

Table V: Optimization results for the generalized friction actuator model for five trials

of the output power of the TF will yield an efficiency term to be compared with the

expected value of 90%.

Optimization of Generalized Friction Actuator Model

Upon completion of the simulation, optimization of the generalized friction model could be accomplished. This was approached by use of the evolutionary optimization algorithm biogeography-based optimization previously discussed. In addition to the basic algorithm, mutation and elitism were utilized once again. Each run was begun with a random seed. Five trials were run with the algorithm parameters of Table II. The parameter ranges defined in Table III were used for each of the trials. All constraints were equivalent between the basic actuator model optimization and the generalized friction actuator model optimization. The cost function was also consistent with the basic actuator model optimization.

Generalized Friction Actuator Model Results

Associated with each trial a best parameter set was determined. The results of the five trials are shown in Table V. While it cannot be concluded from the results of the individual trials that a global optimum was found by the optimization algorithm, it is clear that particular ranges of the parameters tend to cause the maximum capacitor charge. The consistency across the capacitor charge gained, capacitor energy gained, and friction losses columns between trials is striking in that this suggests
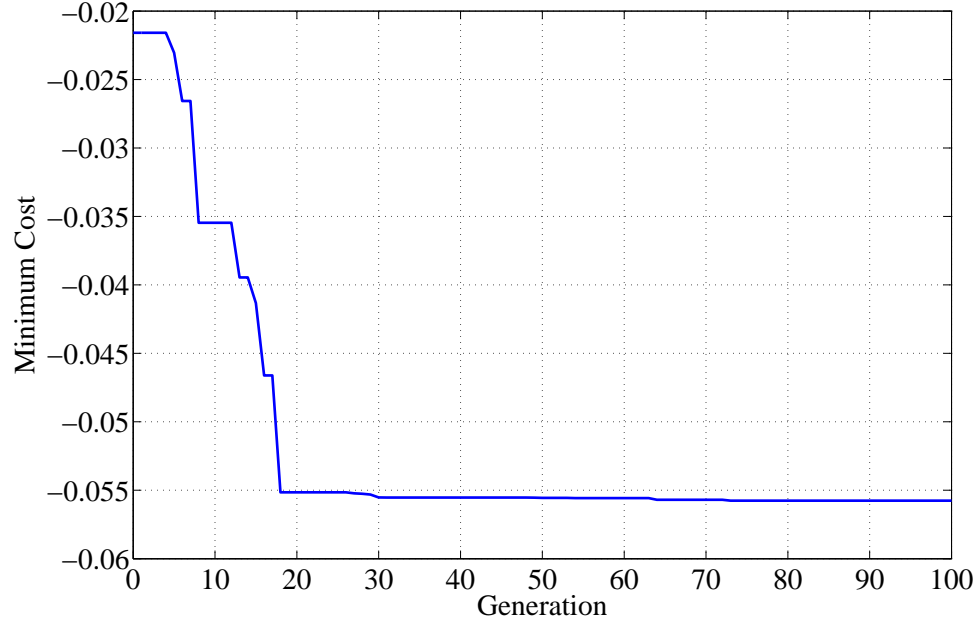
Figure 24: Progression of the minimum cost for an optimization run for the generalized friction actuator model for a single gait cycle

that even with the variations among the system parameters, the algorithm may have been consistently approaching the same limit.

Example results will be provided for Trial 1. For each of the five optimization runs convergence was achieved. An example plot is shown in Figure 24. Though the greatest decreasing behavior occurs until generation 20, visible improvements may be noted up to approximately generation 72. This indicates that 100 generations was once again sufficient.

Because the timing of the efficiency switching could not be exactly determined during the u-inversion process for this case, the tracking, as shown in Figure 25, is no longer mathematically perfect. The error of the simulated data versus the reference data according to equation (3.24) was $RMS_{total} = 0.0011$ rad. However, this is still sufficient accuracy for gait.
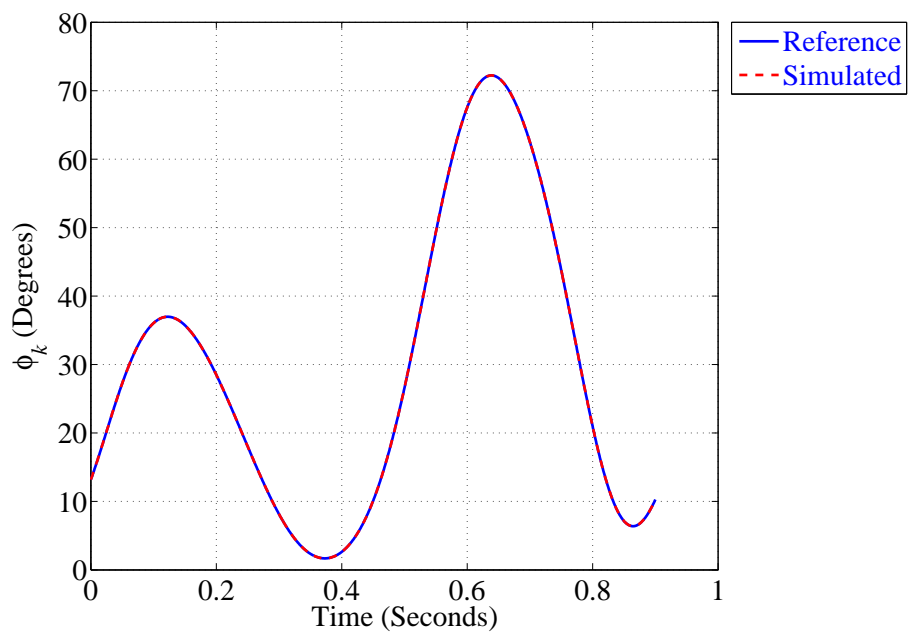
Figure 25: Tracking performance of generalized friction actuator model for single gait cycle
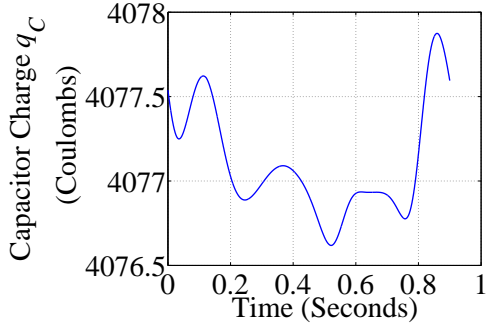
(a) Capacitor charge over one gait cycle. An overall gain is observed.
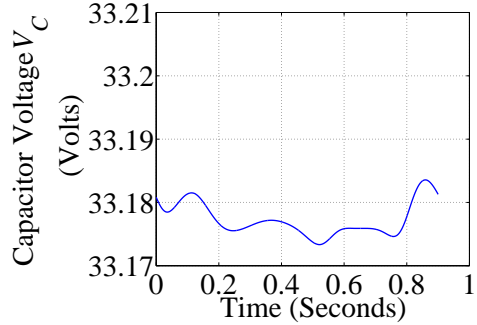
(b) Capacitor voltage over one gait cycle. A slight increase in voltage is indicated
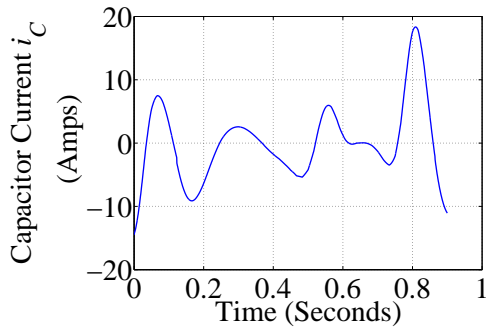
(c) Capacitor current over one gait cycle

Figure 26: Plots illustrating behavior of the generalized friction actuator model electrical system over one gait cycle

A set of plots demonstrating the electrical features of the system is given in Figures 26a–26c. Within the first plot one can observe the overall increase in charge of the capacitor. The voltage remains fairly constant with small variations yet increases in correspondence with the increase in charge. There is significant variation in the current, indicating the variable nature of the required torque. In general, the electrical attributes are very similar to each of the previously presented cases.

A plot exhibiting the change in energy within the elements of the system was also created and is shown in Figure 27. While an exact energy balance could not be computed for this case as it was forced into a non-energy conserving state, the model could be checked by comparing the energy balance and the frictional losses
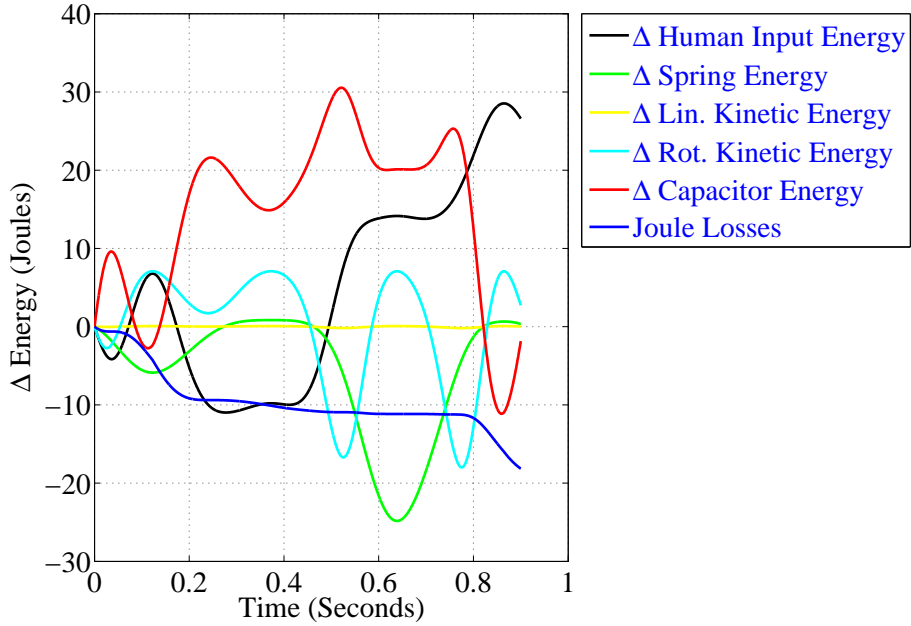
Figure 27: Plot illustrating the change in energy of each component of the generalized friction actuator model. For the given sign convention a negative change in energy corresponds to energy gained by a component

value. These values were equivalent within several thousandths of Joules, confirming that the system was balanced, though not energy conserving.

Once again an alternating pattern between the capacitor and human power flows is observed in Figure 28, representing the power exchange between the human and prosthesis. Additionally, one can see indications of the switching of the efficiency value within this plot as it causes discontinuities in the power flow.

Finally, the results of the efficiency model were plotted in Figure 29 to confirm its accurate performance. A brief transient is observed. This is due to the fact that $\eta = 1$ initially within the simulation. If $\eta = \dfrac{1}{0.9}$, which is the case for this specific data set, the transient effect is eliminated.
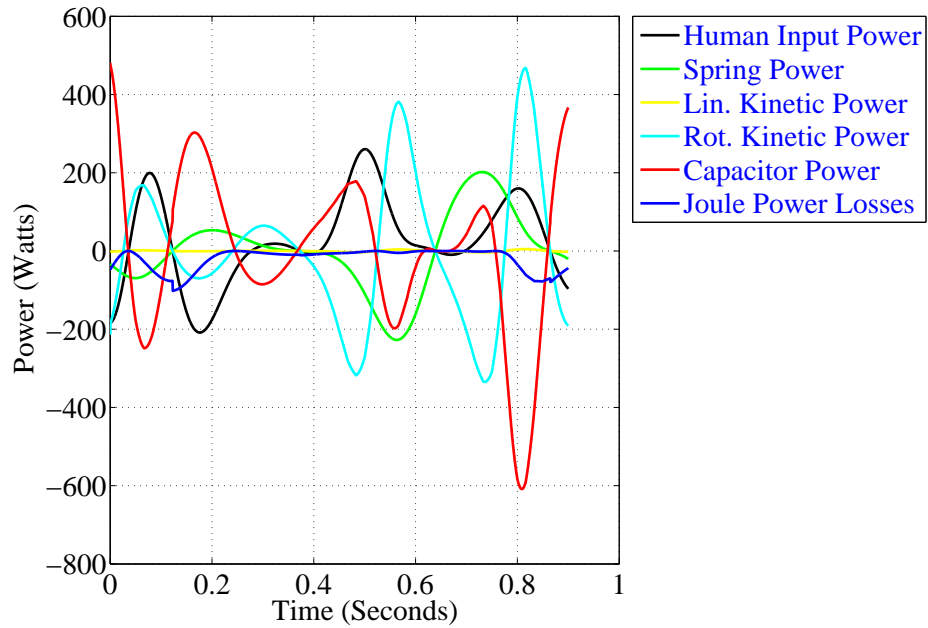
Figure 28: Plot illustrating the power of each component of the generalized friction actuator model. For the given sign convention a positive value corresponds to power entering the bond graph body, thereby exiting a component
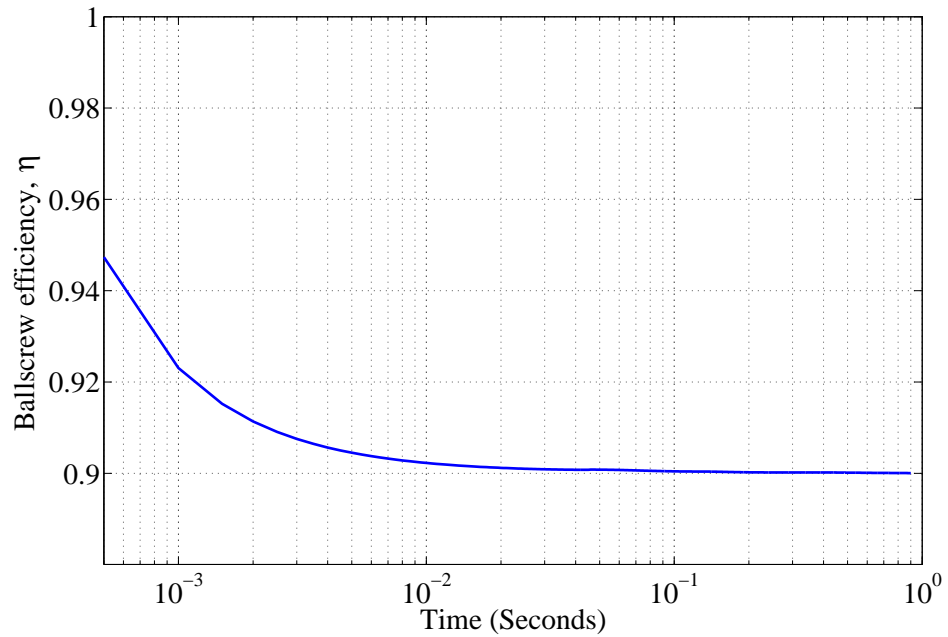
Figure 29: Efficiency of the ballscrew throughout one gait cycle

3.4 Discussion

Three individual models of a crank-slider actuator for an active prosthetic leg were developed and validated within this chapter. First, a basic actuator model mirroring a direct drive actuation system model from [33] was studied. The second actuator model explored an approach to modeling the frictional losses of the ballscrew based upon its geometry and preload. The final method was the implementation of generalized friction losses based upon an efficiency percentage, decoupling the ballscrew geometry from the addition of friction to the simulation. This method was pursued because it allows greater freedom in optimization; the ballscrew may simply be modeled by its lead value as in the basic actuator model.

The basic actuator model showed the potential for this actuator style to successfully collect excess energy at the knee joint across multiple optimization trials. Among the three actuator models this model, which was without mechanical losses, resulted in the greatest increase in capacitor charge, 0.3932 C.

The results of simulation of the complex friction actuator model indicated that the manufacturer's value of 90% efficiency is beyond sufficient as the lowest value recorded for this model was approximately 97%. Additionally, for the specific parameter set used in this simulation, regeneration capacity was maintained. The second lowest increase in capacitor charge, this model showed a gain of 0.2620 C. Looking to future development, the predicted regeneration capacity of the complex friction model simulation is equivalent to 26% of the energy needed for driving an ankle motor according to Winter's data for a fast walking pace [52].

Simulation and optimization of the third model, the generalized friction actuator model, was completed for a total of five trials. For many parameters a clear range arose among the best solutions. Even at 90% efficiency the system was capable of charging the capacitor. This model resulted in the smallest increase in capacitor

charge, a total of between 0.055 C and 0.060 C, dependent on the trial.

In summary, all three actuator models resulted in an increased capacitor charge over one gait cycle of the CC reference data. With each consecutive increase in the total friction modeled, a decrease in the accumulated charge is observed, providing confirmation of the models' accuracy. One future direction for expansion of this work is optimization of the motor and perhaps other aspects of the system to decrease the losses due to the armature resistance, a multifaceted problem. Further considering the energy regeneration capacity, it would be of interest to theoretically determine the maximum limit possible and compare this value to the results achieved through optimization. Additionally, looking toward physical application of the actuator, machine design work must be completed. Finally, the models may be extended and evaluated for the ankle joint of a fully actuated prosthesis.

CHAPTER IV

GROUND CONTACT MODEL DESIGN

AND OPTIMIZATION

In considering the development of a controller emphasizing energy regeneration, a broader model must be developed. Such a proposed model should include a hip model in combination with a prosthesis model as well as a method of simulating the effects of ground contact. A simulation of the Cleveland State University hip robot and a Mauch prosthesis may be modified to address the first two requirements and will be further discussed in Chapter V. A method of approaching the third and final requirement, a ground contact model, will be addressed within this chapter.

As indicated in Figure 6, the hip robot operates in two dimensions. To be applicable, the available reference data was processed down to two dimensions. Therefore, it is required that any contact model developed for this case must also be two-dimensional. Such a model has been previously implemented within the combined hip robot-prosthesis simulation, yet its goal was solely replicating two-point, heel and toe, contact with an approximately realistic magnitude for a single data set. This limits its capacity to provide realistic ground reaction forces to the simulation when any variation is introduced, consequentially limiting the ability to optimize a controller across a variety of data.

In Section 4.1.1 the original contact model is reviewed, and a novel contact model is developed in Section 4.1.2 to meet the aforementioned needs. Sections 4.2 and 4.3 are also unique contributions of this work. The methods used in optimizing this model are described in Section 4.2. This is followed by Section 4.3, which presents the results of the ground contact model optimization for several sets of test data. Section 4.4 concludes the chapter with a discussion of these results.

4.1   Ground Contact Model

4.1.1   Initial Hip Robot Contact Model

The ground contact model original to the hip robot simulation as presented in [28] was based on a spring and kinetic friction. A vertical force and a horizontal force were each determined for both the heel and the toe. Because the treadmill is a flexible walking surface, a spring model was selected for the vertical force calculation. Observing the horizontal ground reaction force for the anterior-posterior direction, Figure 30, one may note that it appears to be a scaled version of the vertical force with a change in sign in the middle, leading to the general kinetic friction model with a sign modification added.

According to a linear spring model

$$F_{vert} = -k_{belt}\delta_{vert} \tag{4.1}$$

the force is directly proportional to the compression of the spring; note that extension past the spring's equilibrium is not possible in this case. The vertical displacement δ_{vert} is, practically speaking, the distance that the heel or toe dips beneath the treadmill "ground level." It may be calculated by subtracting the vertical coordinate of the heel or toe from the distance from the hip robot's world origin to the treadmill
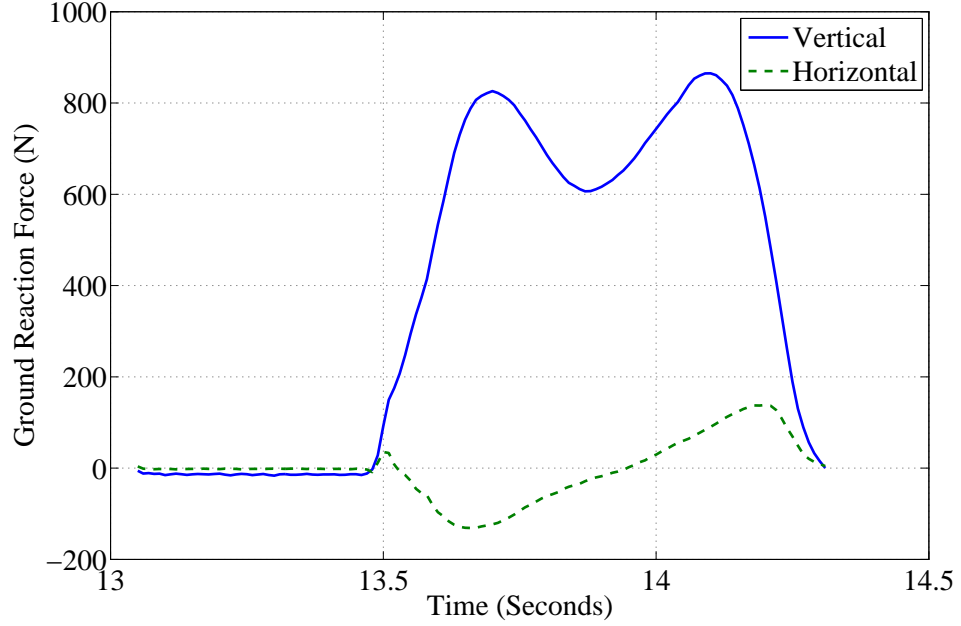
Figure 30: Single stride example ground reaction force data from Subject AB01, Trial 003

surface, also called the standoff.

$$\delta_{vert} = \text{standoff} - (\text{heel or toe})_{vert} \tag{4.2}$$

Having determined the vertical force at both the heel and the toe, which is a normal force, the equation for kinetic friction may be applied directly to determine the horizontal force for the heel and toe. The modification of the sign is handled as shown.

$$F_{horiz} = -\left|\mu F_{vert}\right|\text{sign}\Big((\text{heel or toe velocity})_{horiz} - (\text{belt velocity})\Big) \tag{4.3}$$

The values assigned to each of the constants in the previous three equations are given in Table VI.

Parameter	Value	Units
$k_{belt,heel}$	30000	N/m
$k_{belt,toe}$	50000	N/m
$standoff$	1.03	m
μ	0.2	$unitless$

Table VI: Parameters used in the initial hip robot contact model

4.1.2   Novel Ground Contact Model

The initial approach to developing a new contact model for use with a broad array of data was based on an architecture identical to the model discussed in Section 4.1.1 because in reality the closest model to a compliant belt is likely some form of spring. Therefore, the initial model only differed from the original model in that it included optimization (see Section 4.2 for algorithm details) of a threshold and a stiffness constant for each the heel and the toe; the horizontal force model remained the same. It should be noted that due to the method of processing the dataset of Section 2.2, the definition of δ_{vert} is as shown in equation (4.4) from this point forward. Here "threshold" is a small vertical shift dependent on the depth of ground penetration required for sufficient contact.

$$\delta_{vert} = \text{threshold} - (\text{heel or toe})_{vert} \tag{4.4}$$

While this method did address the basic need, tuning the model to variable data, it did not do so with good accuracy referred to the reference data. Particularly, the results tended toward an overly extensive contact period, primarily before heel contact is indicated to begin in the reference data, Figure 31c. Because the heel was typically the source of this excess contact time, the heel force was frequently minimized to unrealistically small values, Figure 31a.

(a) Heel

(b) Toe

(c) Total
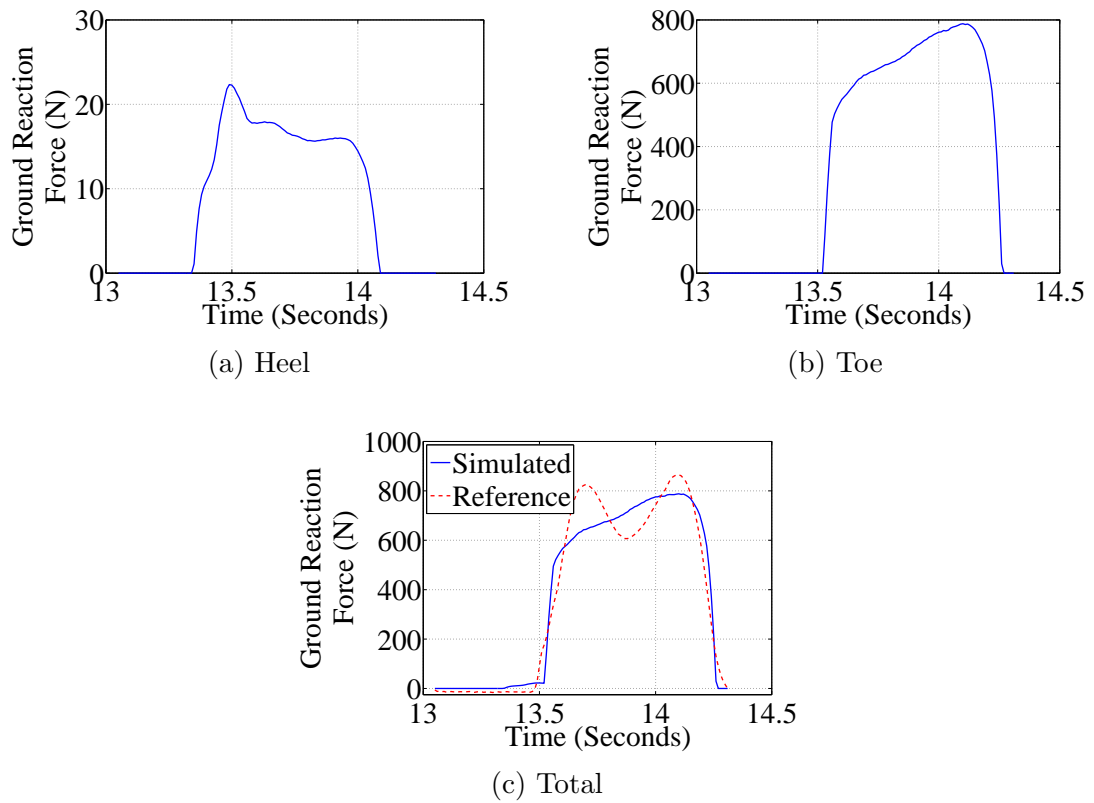
Figure 31: Example vertical ground reaction force case resulting from optimization of the contact model presented in Section 4.1.1 for Subject AB01, Trial 003

(a) Heel

(b) Toe

(c) Total
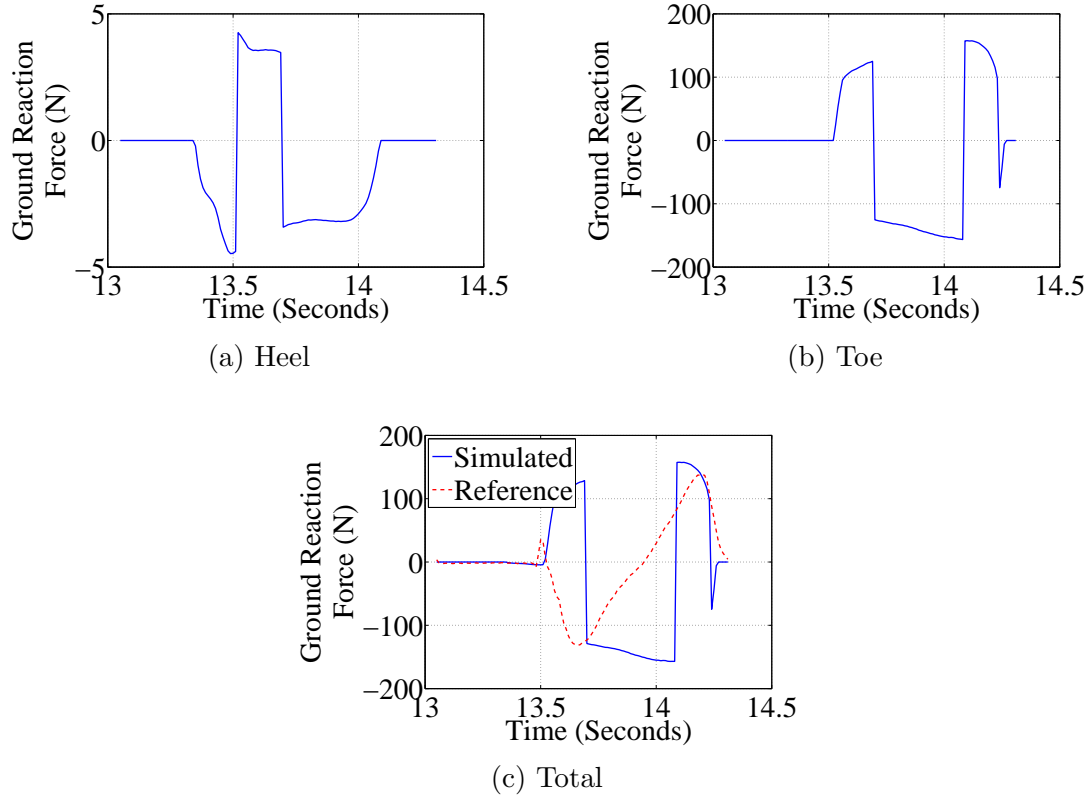
Figure 32: Example horizontal ground reaction force case resulting from optimization of the contact model for Subject AB01, Trial 003

The results of the horizontal contact model are shown in Figure 32. These results were deemed acceptable on several grounds. First, the overall magnitude was accurate. Secondly, each of the positive and negative sections were represented over the stride, though they were shifted. Lastly, the magnitude of the horizontal force is small relative to the vertical force, decreasing its effects. Therefore, the same horizontal contact force model was kept for all trials.

In an effort to improve upon the model, a number of variations with respect to the spring were tested including quadratic, cubic, and quartic models. Not realizing the desired change throughout these iterations suggested a fundamental shortcoming of the model. Truly, the sole of the foot does not fit into solid body mechanics [53]. Rather, there is significant tissue before the "solid body" bone makes contact with
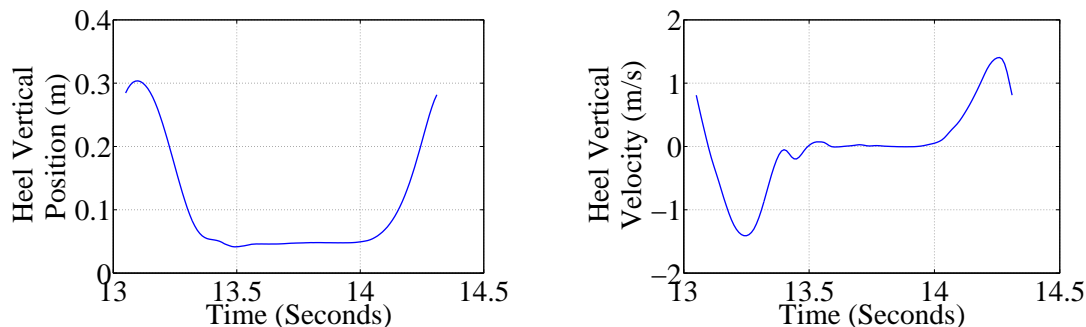
(a) Heel position. Note that sign is opposite world coordinate system for illustration purposes

(b) Heel velocity. Note that sign is opposite world coordinate system for illustration purposes

Figure 33: Example heel trajectories for Subject AB01, Trial 003

the ground. Numerous complex finite element models have been developed in the study of the effects of foot structure on its loading [3, 10, 22]. Because of the time required for optimization iterations, a faster method than finite element modeling is required for this application. Furthermore, the level of detail and accuracy resulting from such models would significantly exceed the requirements of this work. Hence the addition of a damping term was considered as an alternative solution.

A damping force at a basic level can be considered velocity dependence, paralleling a stiffness force which is displacement dependence. As the foot proceeds through heel strike, see Figure 33, the vertical velocity decreases until solid contact, full compression, of the heel at which point the velocity settles to practically zero. Using this information, one may infer that damping, velocity dependence, could play an important role in heel contact timing. One model illustrating a version of this approach may be found in [1]. In this case a total of 10 spring-damper units are spread across the surface of the sole of a two-dimensional foot model. Each element follows

$$f_{y,j} = a\delta_j^3 \left(1 + b\dot{\delta}_j\right). \tag{4.5}$$

Within this equation $f_{y,j}$ is the vertical force at each element, a is the stiffness, b is the damping, and δ_j is the distance by which the jth element penetrates the ground.

Because two contact points are to be used to replicate the ground reaction force in this work as opposed to ten, the model from [1] still overcomplicates the solution. Accordingly, an alternative model was developed, keeping this model in mind. Considering the form of the data, refer to Figure 33, it follows that the higher velocity corresponds primarily with soft tissue contact rather than compressed soft tissue and bone. Therefore, an implementation of the damping approach that acts as a valve or continuous switch, allowing less force through during higher velocity periods and more force through during lower velocity periods, seems rational. This may be implemented as shown below.

$$F_{vert} = -k_{belt}\delta_{vert}(1 - \text{sat}(b\dot{\delta}_{vert}^2, 0, 1))$$ (4.6)

Within equation (4.6) a linear spring determines the magnitude of the vertical force, identical to the initial contact model. This is then multiplied with a term that includes a saturation function, limiting its output to between zero and one. This term either allows the full magnitude of the vertical force to pass or scales it back with increasing velocity. If the velocity is too large, this term can reach zero, completely eliminating the vertical force. The value b is the damping constant of a quadratic form. $\dot{\delta}_{vert}$ is the time derivative of equation (4.4). To take a smooth derivative of δ_{vert}, a transfer function was utilized.

$$TF_{derivative} = \frac{s}{0.025s + 1}$$ (4.7)

The value of 0.025 was selected by trial and error to maintain relative peak magnitudes while providing a smooth result to avoid irrelevant switch action. The horizontal contact model was maintained.

In summary, a novel contact model has been developed. It includes features of the terrain, namely belt stiffness and friction, as well as a basis in the soft tissue

63

and bone combination influencing the sole of the foot. The next section will discuss the selection of the constants associated with this model via optimization.

4.2 Contact Model Optimization

Because of the nature of the developed contact model, the constants sought have not been previously defined in the literature. Additionally, adequate reference data is available. This combination fits well within an optimization framework. Within Section 4.2.1 the selected optimization algorithm, particle swarm optimization, will be presented. Particle swarm optimization was selected for this problem since it is strong in both global and local exploration, an important feature because little intuitive judgement could be used for initializing some of the parameters to be optimized. Discussion of the method in general will be followed by the detail of how particle swarm optimization was applied to the given problem, Section 4.2.

4.2.1 Particle Swarm Optimization

The particle swarm optimization (PSO) methodology is based upon the swarming behavior of birds, fish, and other creatures. Each of these creature groups have an optimal method of moving through space. Studies have indicated that each individual's movements are dependent upon both the individual's preferred motion and its neighbors' trajectories. This combination of trends leads to the best overall motion pattern for the group. Many forms of PSO have been developed based on this generalized idea; only one version will be described here [6, 41].

Translating the swarm behavior into an algorithm, a population of candidate solutions is initialized in two steps. First, each solution is given a starting position and velocity. Secondly, the cost function for each candidate solution is evaluated. These candidates are then sorted from best to worst, and the best individual is labeled the

current global best. A generational progression is then begun. At the start of each generation the global best is identified and saved. For each candidate solution its personal best is updated if its current position is an improvement on the past best, and its neighborhood best is identified. The neighborhood for this version of PSO is being defined as a particular number of nearest individuals; the number of individuals in the neighborhood is a tuning parameter of the algorithm [41].

Identification of each best is followed by an update of each individual's velocity

$$
\begin{aligned}
\Delta v_{personal,i} &= r_{1,i} \; \phi_{1,max} \left(v_{personal \; best,i} - v_{current,i} \right) \\
\Delta v_{neighborhood,i} &= r_{2,i} \; \phi_{2,max} \left(v_{neighborhood \; best,i} - v_{current,i} \right) \\
\Delta v_{global,i} &= r_{3,i} \; \phi_{3,max} \left(v_{global \; best,i} - v_{current,i} \right) \\
v_{new,i} &= \kappa \left(v_{current,i} + \Delta v_{personal,i} + \Delta v_{neighborhood,i} + \Delta v_{global,i} \right),
\end{aligned}
\tag{4.8}
$$

where i refers to the index of the individual in the PSO population. The first three equations describe the change in velocity caused by the three components, personal, neighborhood, and global bests. The difference between each best and the current velocity is multiplied by a random number r scaled by ϕ_{max} such that the value is between zero and ϕ_{max}. Each ϕ_{max} is a tuning factor for the algorithm; in ascending order they are termed the cognitive constant, the neighborhood social constant, and the global social constant. Within the final equation all of the velocity change factors are added to the current velocity. This sum is scaled by κ, the constriction coefficient; it prevents the velocity from reaching unstable magnitudes and is calculated as shown, where α is a tunable parameter [41].

$$
\kappa = \frac{2\alpha}{\phi_{1,max} + \phi_{2,max} + \phi_{3,max} - 2}
\tag{4.9}
$$

Upon determining the velocity of each individual, the new velocity is added

to the current position. These values are then bounded by a given range, which has been defined for the problem. The cost is once again calculated, and the population is sorted from best to worst. A form of elitism is then implemented by replacing the global worst by the global best, concluding the generation. The process is replicated for each generation until a stopping criterion is met. In these ways the candidate solutions are scattered over the solution space, performing a global search, and yet are drawn to the best overall solution, performing a local search as the generations progress [41].

4.2.2 Contact Model Optimization

The equations describing the contact model were recreated in block diagram form within Simulink. The forward kinematics for the heel and toe were computed and then fed into these force equations, specifically vertical and horizontal forces were calculated for both the heel and the toe. It should be noted that damping was implemented for both contact areas, heel and toe. Though not discussed earlier, damping was applied to the toe because of the potential for soft tissue effects across the complete sole of the foot. The optimization was left to determine the usefulness of this parameter. In the case that the toe did not require this degree of freedom, b could be set to zero. As in the original contact model μ was set to 0.2. The primary output of the simulation for optimization was the sum of the vertical heel and toe forces, the total vertical force.

The PSO algorithm described in Section 4.2.1 was wrapped around this simulation, which produced the data required to evaluate the cost function

$$RMS = \sqrt{\frac{1}{n} \sum_{j} \left(GRF_{ref,j} - GRF_{sim,j}\right)^2}, \qquad (4.10)$$

where j refers to the sample number in the time interval of interest. With exception of

Parameter	Value
Population Size	50
Number of Generations	75
Number of Elite Individuals	1
Neighborhood Size	5
$\phi_{1,max}$	2
$\phi_{2,max}$	2
$\phi_{3,max}$	2
α	0.9

Table VII: Particle swarm optimization parameters used for optimization of the contact model

Parameter	Minimum Value	Maximum Value	Units
threshold	-0.1	-0.03	m
k_{heel}	-1000000	-1000	N/m
k_{toe}	-1000000	-1000	N/m
b_{heel}	0	2000	s^2/m^2
b_{knee}	0	100	s^2/m^2

Table VIII: Optimization parameter ranges for the contact model

the number of generations, the PSO algorithm parameters were selected by reference to the literature [41]. The number of generations was determined by observation of the convergence behavior. The PSO parameter values are given in Table VII. For each of the parameters being varied within the simulation, ranges were set by observation of the reference data and trial and error. The final selected set is provided in Table VIII. Optimization was setup to be performed over a single, user-selected stride of data from toe-off to toe-off.

4.3 Results

Optimization of the contact model was conducted across three human subjects and at up to three speeds, yielding a total of nine datasets. In each case the PSO algorithm showed suitable convergence behavior within the specified 75 generations, Figure 34. Though in most cases small improvements not visible within the
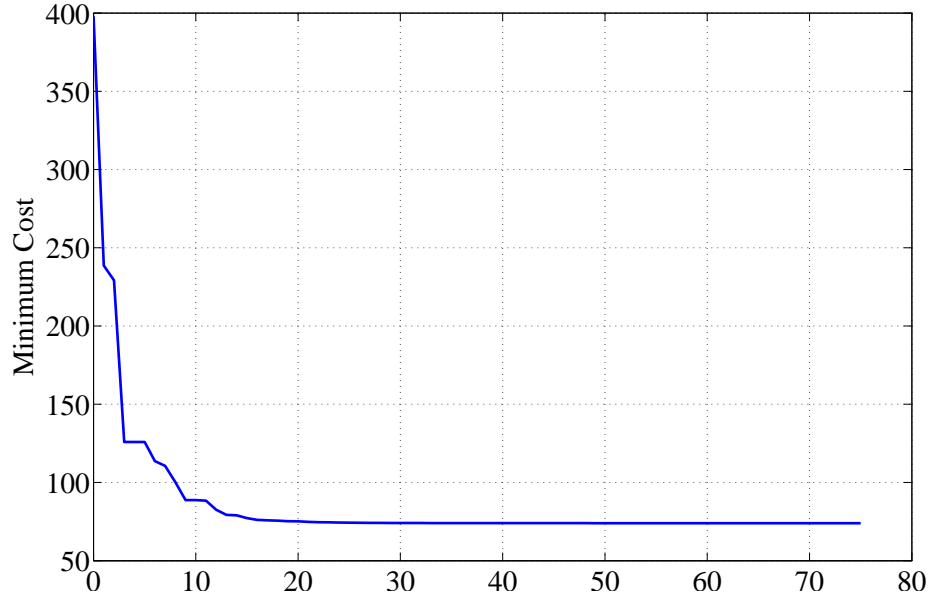
Figure 34: Example convergence curve for PSO optimization of the contact model for Subject AB01, Trial 003

plot continued to be made until the final generation, the average cost (not shown) was approaching near the minimum cost, indicating convergence.

The dataset from Subject AB01 included only preferred speed data; two trials from this set were used for optimization. The dataset from Subject AB03 included multiple trials at three different speeds, fast, preferred, and slow. Two trials at each speed were selected and optimized. It should be noted that the marker data for Subject AB01 yielded a fairly level foot. For AB03 a slight tip downward toward the toe is distinguishable. The dataset for AB04 is included because this dataset had a comparatively larger difference in height between the heel and toe markers, a factor of interest. The optimization is nondeterministic, therefore a set of representative results was selected after multiple optimization runs for each dataset. It was found as a general rule that a cost function value of approximately 90 N, give or take, indicated the potential for a suitable solution. The optimization process indicated a number of local minima. A summary of the example solutions is given in Table IX.

A trend to eliminate the toe damping is seen throughout all of the trials,

68

Subject	Trial	Speed	Optimized Contact Model Parameters					Solution Cost (N)
			threshold (m)	k_{heel} (N/m)	k_{toe} (N/m)	b_{heel} (s^2/m^2)	b_{toe} (s^2/m^2)	
AB01	003	Preferred 1 m/s	−0.0597	6752	36058	101.49	5.31	73.99
AB01	004	Preferred 1 m/s	−0.0574	32481	61706	101.45	0	71.01
AB03	00017	Fast 1.25 m/s	−0.0501	21013	48292	82.35	0	106.88
AB03	00018	Fast 1.25 m/s	−0.0534	22038	41490	1984.73	0	117.47
AB03	00001	Preferred 1 m/s	−0.0570	5134	38985	1745.38	6.15	90.82
AB03	00002	Preferred 1 m/s	−0.0549	1888	39511	0	3.31	91.23
AB03	00011	Slow 0.75 m/s	−0.0448	110536	90664	2000	0	101.53
AB03	00012	Slow 0.75 m/s	−0.0539	13263	48573	854.27	0	92.72
AB04	0001	Preferred 1.3 m/s	−0.0382	289695	60117	1877.43	0	127.74

Table IX: PSO optimization results for the contact model across multiple data sets

suggesting that this is not as significant a factor for the toe as opposed to the heel. Additionally, it may be noted that the lowest cost solutions (AB01) are associated with a more level heel and toe marker set, indicating that this may be a somewhat limiting factor of the contact model; see Figure 35. Beyond these broad remarks, some of the given solutions will be highlighted to note several more features of the results.

Comparing the application of the contact model with damping to the optimization results shown in Figure 31 from optimization of the original model, one may note that while there is still a period of slight heel stubbing, Figure 36, the damping effect allows the optimization process to increase the heel force, Figure 36a, without a large penalty. The peak heel force is increased by a factor of five in this case. Additionally, the toe makes contact quickly after heel strike, and the heel leaves contact prior to toe off, both features of gait.

(a) AB01 (b) AB03 (c) AB04
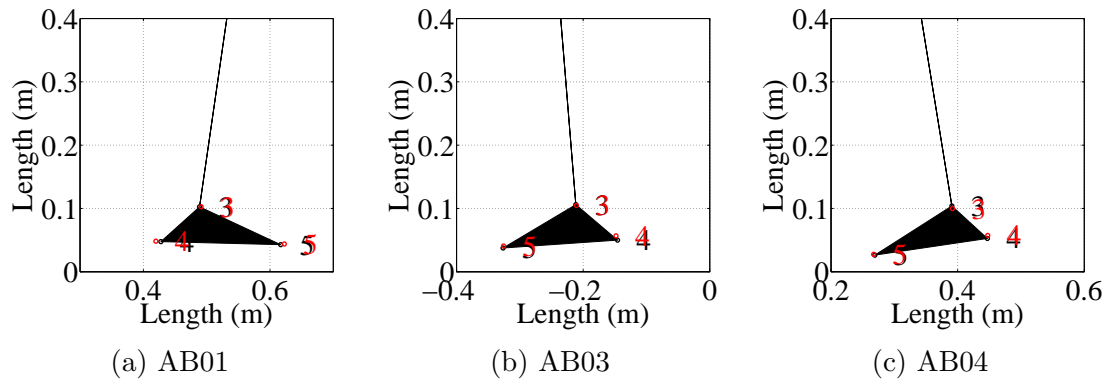
Figure 35: Example inverse kinematics plots illustrating the progression of subject's tendencies toward a sloped foot. Each frame was frozen when the subject's hip marker was directly over his or her ankle marker

(a) Heel

(b) Toe

(c) Total
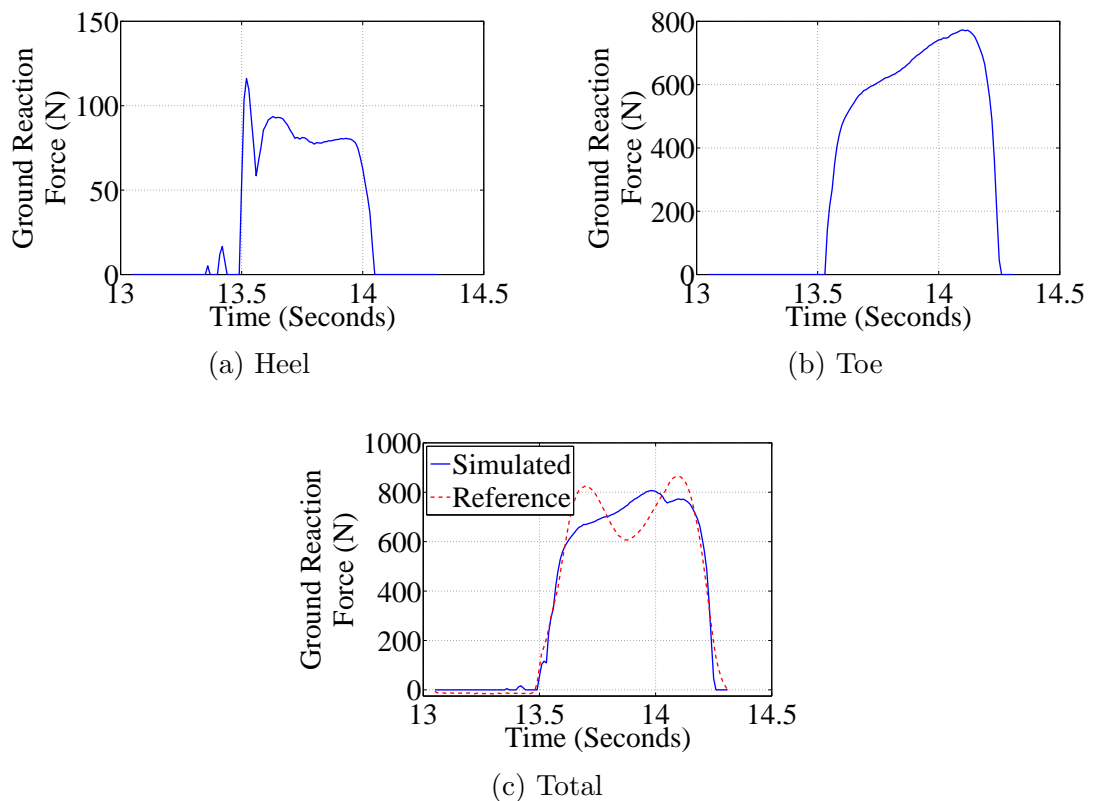
Figure 36: Example vertical ground reaction force case resulting from optimization of the contact model for Subject AB01 at his or her preferred walking pace, Trial 003

70
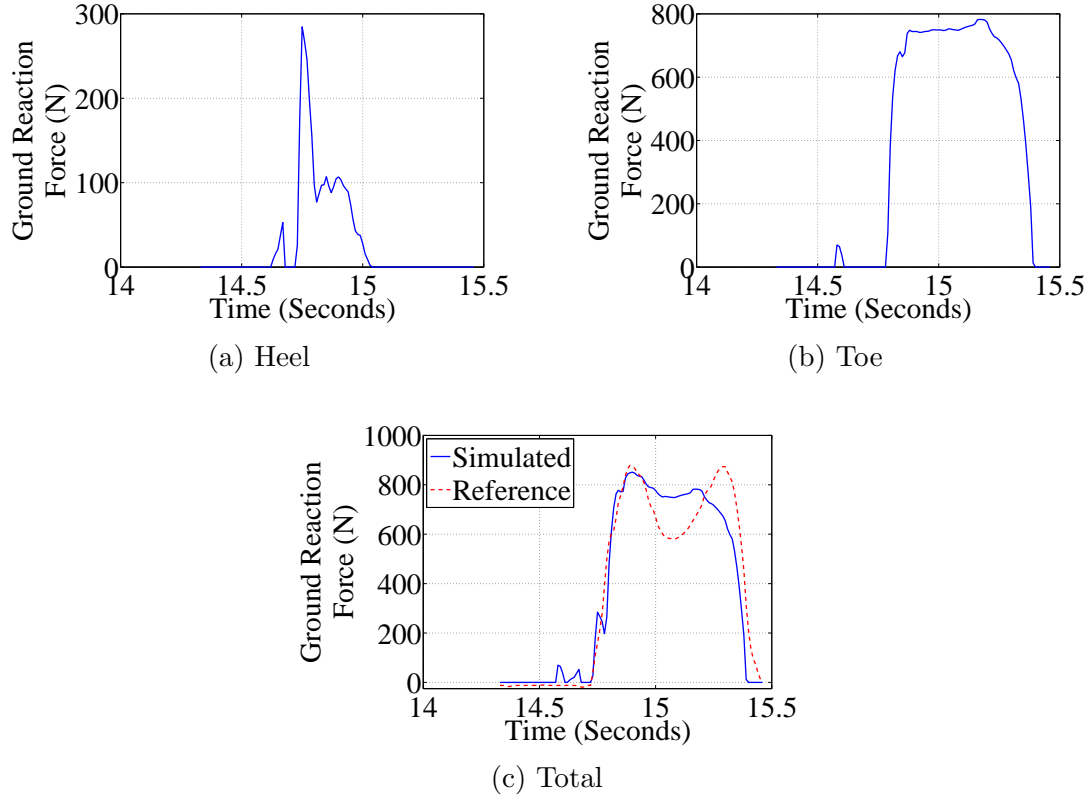
Figure 37: Example vertical ground reaction force case resulting from optimization of the contact model for Subject AB03 at a fast walking pace, Trial 00017

Within the next set of results shown, Figure 37, a brief period of toe stubbing is observed, indicating that the threshold was not low enough. Features such as this are far more common for marker sets where the heel marker is higher than that of the toe, such as is the case for the marker placement for Subject AB03.

The optimization of AB04 presented three cases, significant toe stubbing, complete elimination of heel contact, and an increase of the threshold and heel stiffness. Each of these served the purpose of improving the cost under "toe-dipped" conditions. The third case was most prevalent among the solutions and was, thereby, selected for inclusion in the presented data, Figure 38. It can be seen that the greatest effect of the non-level foot for this example dataset is the limited heel contact period.

(a) Heel

(b) Toe

(c) Total
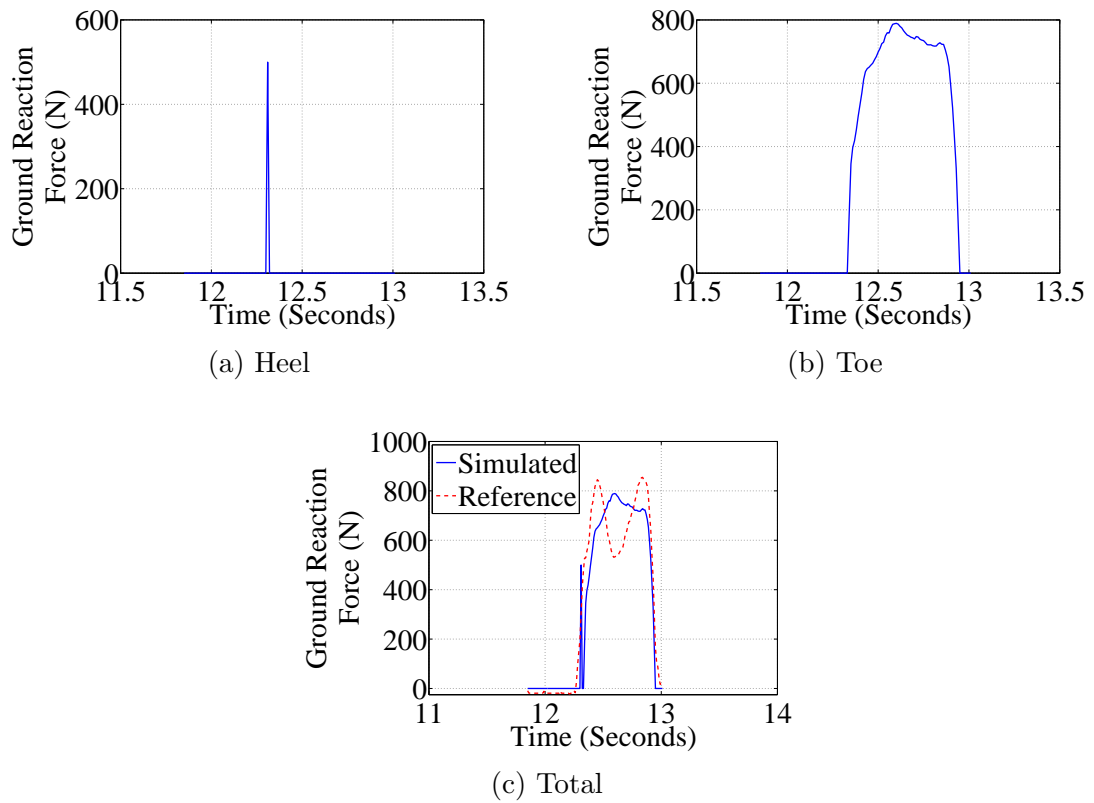
Figure 38: Example vertical ground reaction force case resulting from optimization of the contact model for Subject AB04 at his or her preferred walking pace, Trial 0001

4.4 Discussion

A contact model for use with two-dimensional data has been developed and tested. The goal was to form a model that could be optimized for use with the hip robot simulation and a variety of datasets. Heel contact was improved over the original model by introducing damping, velocity dependence. The model was tested over nine different datasets in each case providing a workable solution, though some would be preferred. It was also shown through this process that the damping effect was of greater importance at the heel, which is the location of greatest impact during gait, in comparison to the toe.

It can be seen across the results that a true double-peaked solution was not obtained. It is likely due to the fact that the heel force, though increased, is still low in comparison to the literature. Though heel and toe forces are not easily measured separately, resistive devices and pressure mats can provide a comparison of magnitude. These values suggest that the peak heel force should be less than that of the toe force yet reach between two-thirds and three-quarters of the peak toe force [2, 27, 32]. Future modifications to improve the magnitude of the heel contact may include changing the form of the damping portion of the equation or integrating several spring models, such as using both linear and quadratic types. Implementing the contact model within a dynamic simulation with closed loop control may also improve the force profile because the forward kinematics driven approach does not react to contact. By extension, the optimization of the contact model could be completed within a dynamic simulation.

The model is also limited by its ability to adapt to marker sets in which the heel and toe markers are not practically level. While a working solution could still be generated in these cases, it is rarely realistic. Because variation in the placement of markers is common, this issue will be ongoing. Anatomy would suggest that the

variation being seen is due to the placement of the heel marker because there is greater freedom at this location of the body as opposed to the toe. To limit the effects of this, the addition of an offset to the heel marker data, approximately leveling the heel and toe, when defining the subject dimensions and prior to the inverse kinematics computation may be possible.

These limitations being considered, the contact model is still consistent in its replication of heel strike, toe off, and the overall magnitude of the force relative to the reference data. Therefore, it is sufficient for use in dynamic simulations where these items are of primary importance such as will be required in Chapter V.

CHAPTER V

CONTROL SYSTEM DESIGN AND OPTIMIZATION

Robust tracking/impedance control has been recently introduced as a controller for systems that include both joints that should be controlled by a tracking strategy and joints that should be more pliable, combining tracking with force control [28]. Additionally, a form of impedance control with gain scheduling has been presented in the past as a reliable means of controlling a transfemoral prosthesis [45, 46]. The first controller has been tested with a single dataset on the same general model as is being used within this work [28]; however, the gains were hand tuned and the emphasis was not on energy regeneration. The second controller also appeared to be tuned without reference to energy regeneration.

In this chapter the combination of and expansion upon the robust tracking/impedance controller and the gain-scheduled impedance control work is sought in two ways. First, the robust tracking/impedance controller will be applied to the complete system, and the gait cycle will be broken into several sections. For each individual section, as appropriate, a set of gains will be defined. Secondly, the gain set will be optimized using multiple objectives, including energy regeneration.

Sections 5.1–5.3 cover precedent research. In Sections 5.4–5.6 new contri-

butions are communicated. The dynamic model of the hip robot and prosthesis is conveyed in Section 5.1. In Section 5.2 the robust tracking/impedance controller will be described. The gain-scheduled impedance control work will be covered in Section 5.3. Upon establishing each individual controller, the method proposed of combining the two will be discussed, Section 5.4. Next, Section 5.5 will present the details of the optimization. This will be followed by results, Section 5.6. A discussion, Section 5.7, will conclude.

5.1   Hip Robot and Prosthesis Dynamic Model

A dynamic model of the hip robot and a prosthesis was obtained for testing of the controller in simulation. This model is developed in detail up to the ankle joint in [36]. Several modifications and the addition of a foot model have been made since that publication. Some of these changes are reflected in [28]. Further adjustments for use in this work have also been made; therefore, the model will be briefly described in this section.

Of greatest importance among the changes made to the model is the addition of a foot model. This development was originally completed by the author of [28], and it was then modified for this work. The foot is of the form shown in Section 2.2.5. The forces applied to the foot are determined according to the contact model given in Section 4.1.2. The effects of these forces at each of the four joints, hip translation, hip rotation, knee rotation, and ankle rotation, are then calculated by use of the transpose of the Jacobians for the heel (h) and the toe (t).

$$\begin{bmatrix} F_{1,h} \\ \tau_{2,h} \\ \tau_{3,h} \\ \tau_{4,h} \end{bmatrix} = J_{v,h}^{T} \begin{bmatrix} F_{horiz,h} \\ F_{vert,h} \end{bmatrix} \tag{5.1}$$

$$\begin{bmatrix} F_{1,t} \\ \tau_{2,t} \\ \tau_{3,t} \\ \tau_{4,t} \end{bmatrix} = J_{v,t}^T \begin{bmatrix} F_{horiz,t} \\ F_{vert,t} \end{bmatrix} \tag{5.2}$$

The Jacobians may be found in Appendix H.

The complete system was derived in the robotics framework.

$$M(q)\ddot{q} + C(q,\dot{q})\dot{q} + G(q) + R(\dot{q}) + T_e = u \tag{5.3}$$

T_e is the external force effects equal to the sum of the left-hand vectors of equations (5.1) and (5.2). The linearity in parameters property holds true for (5.3), and it may, therefore, be rewritten as follows:

$$Y(q,\dot{q},\ddot{q})\Theta = u - T_e. \tag{5.4}$$

The inertia matrix M, Coriolis matrix C, gravity vector G, and friction and damping vector R are shown in terms of the parameters Θ in Appendix I.

In addition to the definition of new parameters because of the foot model extension, other changes were made to the parameter set relative to [36]. First, several values were updated. Secondly, to better represent the reference data within simulation cases, the link lengths were set to the subject physical parameters. The parameters used for this work are reported in Table X.

5.2 Robust Tracking/Impedance Control Overview

Robust tracking/impedance control is a combination of two control methods, robust passivity-based control and impedance control. Robust passivity-based control is a motion control strategy that takes advantage of the passivity property

Parameter	Symbol	Value	Units
Mass of link 1	m_1	40.5969	kg
Mass of link 2	m_2	8.5731	kg
Mass of link 3	m_3	2.29	kg
Mass of link 4	m_4	1.0875	kg
Length of link 2	l_2	Subject thigh length	m
Length of link 3	l_3	Subject shank length	m
Length of link 4	l_4	Subject foot length	m
Length joint 1 to link 2 CG	c_2	0.09	m
Length joint 2 to link 3 CG	c_3	0.32	m
Length joint 3 to link 4 CG	c_4	$l_4/2$	m
Rotary inertia of link 2	I_{2z}	0.435	kg-m^2
Rotary inertia of link 3	I_{3z}	0.0618	kg-m^2
Rotary inertia of link 4	I_{4z}	0.0184	kg-m^2
Link 1 sliding friction	f	83.33	N
Link 2 rotary damping	b	9.75	N-m-s

Table X: Parameter values used in the combined hip robot and prosthesis simulation. CG stands for center of gravity

of the robotic equations and is capable of handling parameter uncertainties, which is particularly important in live implementation [43]. Impedance control is a means of controlling force and velocity's relationship [14, 15, 16]. A controller combining these two approaches is desirable for the system of Section 5.1 because the upper two joints, hip vertical displacement and hip rotation, are required to follow set trajectories, pure motion control, while the prosthesis, knee and ankle joints, should be more flexible while yet following reference data. In this way the natural motion of a human hip is enforced regardless of the force and torque requirements on the hip robot. Further, the prosthesis, because in implementation it is not part of the natural system, may be tuned to act and react more like a human leg. This divides the system's joints into motion controlled (MC) joints q_1 and q_2 and impedance controlled (IC) joints q_3 and q_4 [28]. The general control method, particularly the way in which these two control strategies are interrelated, will be presented next, leaving proof of the method to [28].

First, the desired impedance is described.

$$I\ddot{\tilde{q}}_{IC} + b\dot{\tilde{q}}_{IC} + k\tilde{q}_{IC} = -T_{IC} \tag{5.5}$$

$\tilde{q}$ is the tracking error and T_{IC} is the external force and moment effects. Diagonal matrices I, b, and k are the desired impedance values. The control is then defined in the form utilized in robust passivity-based control.

$$u = \hat{M}(q)a + \hat{C}(q,\dot{q})v + \hat{g} - Kr + T_{IC} \tag{5.6}$$

K is a diagonal matrix of four gains. The first two values of K are for MC joints, and the last two values are for IC joints. This may also be expressed as in the form indicating linearity in the parameters. $\hat{\Theta}$ will be discussed later.

$$u = Y(q,\dot{q},v,a)\hat{\Theta} - Kr + T_{IC} \tag{5.7}$$

According to robust passivity-based control, v, a, and r are defined as follows.

$$v_{MC} = \dot{q}^d_{MC} - \Lambda_{MC}\tilde{q}_{MC} \tag{5.8}$$

$$a_{MC} = \dot{v} = \ddot{q}^d_{MC} - \Lambda_{MC}\dot{\tilde{q}}_{MC} \tag{5.9}$$

$$r_{MC} = \dot{q} - v = \dot{\tilde{q}}_{MC} + \Lambda_{MC}\tilde{q}_{MC} \tag{5.10}$$

For the impedance controlled joints v, a, and r include an extra term.

$$v_{IC} = \dot{q}^d_{IC} - \Lambda_{IC}\tilde{q}_{IC} - F_r z \tag{5.11}$$

$$a_{IC} = \dot{v} = \ddot{q}^d_{IC} - \Lambda_{IC}\dot{\tilde{q}}_{IC} - F_r \dot{z} \tag{5.12}$$

$$r_{IC} = \dot{q} - v = \dot{\tilde{q}}_{IC} + \Lambda_{IC}\tilde{q}_{IC} + F_r z \tag{5.13}$$

Λ is a diagonal matrix composed of four elements, as seen in the motion control set of equations for v, a, and r and the impedance control set of equations for v, a, and r. It is divided into two diagonal matrices, Λ_{MC} and Λ_{IC}, composed of two elements relative to each set of v, a, and r. The term added to v, a, and r is the product of a gain matrix F_r and a dynamic compensator. The dynamic compensator is a state equation with the state $\dot{z}$.

$$\dot{z} = Az + K_p\tilde{q}_{IC} + K_d\dot{\tilde{q}}_{IC} + K_f T_{IC} \tag{5.14}$$

F_r, K_p, and K_d may be calculated from the selected impedance gains. Justification for these values is provided in [28].

$$F_r = I^{-1} \tag{5.15}$$

$$K_p = k + AI\Lambda_{IC} \tag{5.16}$$

$$K_d = b - I\Lambda_{IC} + AI \tag{5.17}$$

At this point $\hat{\Theta}$ may be determined according to the robust passivity-based control framework.

$$\hat{\Theta} = \Theta_0 + \delta\theta \tag{5.18}$$

$\delta\theta$ is a switching term that is determined by a Lyapunov argument [28]. The resulting definition for $\delta\theta$ is prone to chattering, and therefore a deadzone solution was implemented rather than the original version. The deadzone version is given below

[28].

$$\delta\theta = \begin{cases} -\rho \dfrac{Y^T r}{||Y^T r||}, & ||Y^T r|| > \epsilon \\ -\dfrac{\rho}{\epsilon} Y^T r, & ||Y^T r|| \leq \epsilon \end{cases} \tag{5.19}$$

In applying this controller to the hip robot and prosthesis model there are a total of 14 gains to be tuned. There are two values of K and two values of Λ for the motion control joints, two values of K and two values of Λ for the impedance control joints, and lastly, the three impedance values, I, b, and k, for each of the two lower joints. Ten of these gains are associated with the prosthetic joints. All were originally tuned by trial and error.

5.3   State-Based Gain Switching

An alternative control method for prostheses also based on impedance control has been developed. In this case the control equation is simpler, but the gains are switched according to a finite state machine based on measurable features of the gait cycle. The controller was implemented for both the knee and ankle joints and tested with an active prosthesis prototype [45, 46].

Consisting of a spring term, a damper term, and an equilibrium angle, the impedance controller is defined.

$$\tau_i = k_i(\theta - \theta_{ki}) + b_i\dot{\theta} \tag{5.20}$$

i is the index of the current state as determined by a finite state machine. As opposed to the model presented in Section 5.2, this model does not include an inertia term.

The most recent version of the finite state machine includes a total of five modes. These modes are early stance, middle stance, late stance, swing flexion, and swing extension. The flow between these states and the corresponding transitions

81
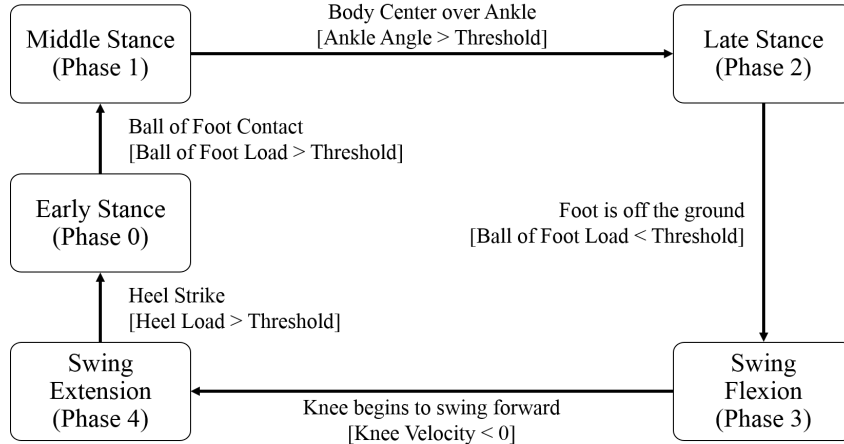
Figure 39: Finite state machine used for switching of control gains. Reproduced from [45]. © 2011 IEEE

are depicted in Figure 39. Each of the measurements required to transition between states are dependent only upon data that could be obtained from the prosthesis, making them hardware-feasible selections.

Considering a total of five states, three parameters per control law, and two joints, there is a total of 30 control gains requiring tuning for this method. Initial tuning was completed via a least squares fit against reference torque, angle, and angular velocity profiles. Further tuning was completed by hand during prototype testing.

5.4 Switched Robust Tracking/Impedance Controller

The controllers discussed in Sections 5.2 and 5.3 both have merit with respect to the human system. In the robust tracking/impedance controller it is assumed that a human will use his or her residual limb the same as before his or her amputation. Additionally, in both cases the application of impedance control implements the capacity to respond to the environment in a dynamic fashion. Within the gain scheduled impedance controller the fact that humans do not present a constant impedance during dynamic action is applied [24]. Taking each of these features and combining

Threshold	Value	Units
Ball of Foot Load	25	N
Ankle Angle	-100	Degrees
Heel Load	25	N

Table XI: Threshold values selected for switching of the finite state machine

them, therefore, should produce a prosthesis controller in better agreement with the human system.

To perform this combination, the exact form of the robust tracking/impedance controller is utilized. It is then augmented with a switching algorithm. The motion control and impedance control gains for the knee and ankle are each allowed to vary over five discrete intervals. These intervals are defined as in Figure 39. There are a total of 5 gains for each joint, forming a combined 10 gains per state. Overall, there are 50 gains to be determined in tuning this controller. In addition, there are several switching thresholds.

The simulation of the hip robot and prosthesis combined from Section 5.1 was modified to include the state switching of Figure 39. After several iterations the threshold values required for switching were determined, Table XI. To avoid premature switching due to any stubbing of the heel or toe, the heel and ball of foot load thresholds were set above the contact level zero. By considering two criteria, the ankle angle threshold was selected. First, the inverse kinematics solution could select from an infinite number of revolutions about the ankle joint, though an equilibrium at approximately -90° or 270° was most likely. For the current code setup the ankle angle threshold needed to be set informed of the trajectory's equilibrium. Secondly, the ankle angle threshold value was selected based on observation of the dataset; the center of mass was judged to be over the ankle when the ankle is slightly dorsiflexed.

5.5 Controller Optimization

The BBO algorithm was selected for the tuning of the switched robust tracking/impedance controller. A composite cost function including tracking, ground reaction force, and energy regeneration was prepared. To bring each component into a general range of magnitude such that each would have an equal chance of being minimized, weights were applied.

$$cost = q_{3,cost} + q_{4,cost} + \frac{1}{100}E_{3,cost} + \frac{1}{200}GRF_{vert,cost}$$

$$q_{3,cost} = \sqrt{\frac{1}{n}\sum_i (q_{3,i,sim} - q_{3,i,ref})^2}$$

$$q_{4,cost} = \sqrt{\frac{1}{n}\sum_i (q_{4,i,sim} - q_{4,i,ref})^2} \tag{5.21}$$

$$E_{3,cost} = \left| (E_{3,t_2,sim} - E_{3,t_1,sim}) - \int_{t_1}^{t_2} P_{3,ref}dt \right|$$

$$GRF_{vert,cost} = \sqrt{\frac{1}{n}\sum_i (GRF_{vert,i,sim} - GRF_{vert,i,ref})^2}$$

where i is the time index of each point in the time interval of interest. Each of the tracking costs and the GRF cost are in root mean square form. The energy cost is calculated such that the change in energy over the simulated gait cycle will approach the total excess of energy available at the knee, determined by integration of the knee power reference data. The energy cost was defined to approach the reference energy because the capacity to gain or lose energy is directly related to the joint torque, assuming the velocity is fixed by accurate tracking performance. Therefore, if realistic torque values are met for the actuation system, it is technically possible for the energy to increase by an amount greater than would be indicated by human reference data. The cost to this, however, is the potential for high reaction forces or

Parameter	Value
Population Size	50
Number of Generations	200
Number of Elite Individuals	2
Probability of Mutation	0.02

Table XII: Biogeography-based optimization parameters used for optimization of the switched robust tracking/impedance controller

Parameter	Minimum Value	Maximum Value
Λ_3 or $\Lambda_{IC,1}$	1	4000
K_3	1	4000
I_3	0.01	6
b_3	1	6000
k_3	1	75000
Λ_4 or $\Lambda_{IC,2}$	1	4000
K_4	1	4000
I_4	0.01	6
b_4	1	3000
k_4	1	75000

Table XIII: Optimization parameter ranges for the robust tracking/impedance controller. The gains for the knee joint are in the upper portion while the ankle joint gains compose the lower half

torques at other joints, making a limit desirable.

BBO was applied in the same form as was discussed in Section 3.3.1. The BBO algorithm parameters were set as given in Table XII for each run. The population size was selected based on the number of individual parameters to be varied. After several iterations the number of generations was determined according to the observed rate of convergence. Each population member included a set of 50 gains, those previously described. For each of the 10 gains per state ranges within which the population features could be varied were set; refer to Table XIII. The population was initialized randomly within these ranges with exception of two candidate solutions, one high impedance case and one low impedance case from [28]. To define these gains for use in the multiple state switching format, the gains were repeated for each state, forming a 50 gain candidate solution. These initial candidates are presented

Parameter	Initial Candidate 1	Initial Candidate 2
Λ_3 or $\Lambda_{IC,1}$	230	230
K_3	350	350
I_3	0.1	0.9
b_3	150	500
k_3	1000	3000
Λ_4 or $\Lambda_{IC,2}$	300	300
K_4	550	550
I_4	0.1	0.9
b_4	30	250
k_4	400	2000

Table XIV: Initial optimization candidate solutions for the robust tracking/impedance controller. The table is divided by grouping the knee joint gains in the upper portion and the ankle joint gains below

Hip Joint Gain	Value
Λ_1 or $\Lambda_{MC,1}$	155
Λ_2 or $\Lambda_{MC,2}$	155
K_1	155
K_2	150

Table XV: Gains used for the hip joint

in Table XIV. Lastly, the gains of the hip motion controller, none of which were being optimized, were selected to provide accurate tracking; see Table XV. Though iterations were not completed, it was found that the gains related to the hip vertical displacement q_1 could be reduced relative to those selected in [28]. The values associated with the hip rotation q_2 were maintained from [28].

Any gain combinations that resulted in divergence were penalized by forcing them to have a cost value of infinity. Such solutions were caught by two methods. The first method was composed of a try/catch statement. If a solution diverged within simulation causing it to throw an error, it would be caught at this level. The second method was post-simulation as a divergent solution did not guarantee that the simulation would crash. These solutions were caught by calculating the difference between consecutive values of q_4. If the absolute value of this difference was greater

Evaluative Measure	Trial 1	Trial 2	Trial 3	Trial 4	Trial 5
$q_{3,cost}$ (rad)	0.006352	0.007332	0.004612	0.012917	0.003954
$q_{4,cost}$ (rad)	0.009355	0.008636	0.009565	0.004577	0.010621
$E_{3,cost}$ (J)	0.0011	0.0491	0.0404	0.0044	0.0010
GRF_{cost} (N)	51.01	54.41	52.33	59.12	51.86
$cost$	0.2708	0.2885	0.2762	0.3131	0.2739
ΔE_3 (J)	9.5639	9.6141	9.6054	9.5606	9.5640

Table XVI: Cost function and energy results for five optimization trials

than 10 degrees, the solution was penalized with an infinite cost. In practice a number of solutions would be penalized early in the generational progression. The number of penalized solutions would then decrease as the population improved throughout ongoing generations. These methods were found sufficient across all trials.

Due to the lengthy computation time required for this optimization, five trials were able to be completed. The data from Subject AB01 Trial 003 and related contact model were used across all trials. While the state switching method is capable of self-initialization during multiple stride trials, it was initialized by hand because of the single stride data being used in each trial. The results of these trials will be presented in the next section.

5.6 Results

Across five trials the final cost measures and amount of energy gained were remarkably consistent. These results are summarized in Table XVI. The accuracy of the tracking error is sufficient for gait across all trials. In comparison to the contact model for Subject AB01 Trial 003, GRF_{cost} has made significant improvement as well. According to integration of the precalculated power data from the VA dataset, the available energy at the knee is 9.565 J for Subject AB01 Trial 003, which each of the solutions approaches as desired. To further evaluate the detail of the results, examples will be provided from Trial 1. The convergence behavior of the minimum

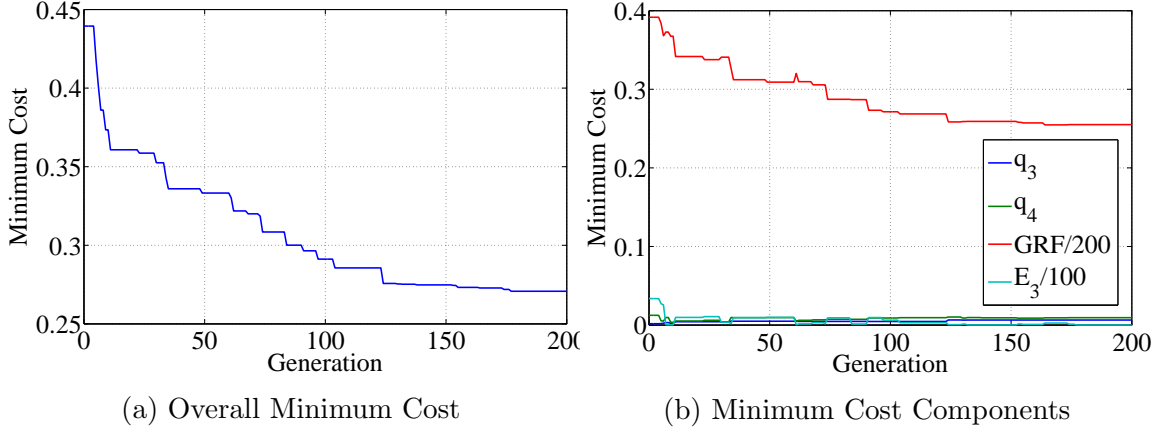(a) Overall Minimum Cost   (b) Minimum Cost Components

Figure 40: Example convergence results from Trial 1 optimization

cost and its components is shown in Figure 40.

The gains determined by the optimization process for all trials are reported in Appendix J. Variation in the selected gains from trial to trial is fairly extensive. This may suggest that there are many combinations possible to form the same level of performance upon which the cost functions appeared to be converging. However, one trend amid the variation is particularly notable. There is a high stiffness predicted for the knee upon heel strike (State 0), and a clear reduction during State 1. This may replicate the reduction in torque resisting knee flexion after the initial impact, as seen in [52].

In addition to the optimization indicators, plots were generated to observe the simulation results. The tracking performance is provided in Figure 41. Excellent tracking is seen for both hip trajectories and the knee trajectory. The ankle trajectory is also quite good. It is of particular interest because it portrays the expected behavior of an impedance controller. It allows divergence from the path but quickly regains tracking accuracy. The knee shows the same behavior though on a more limited scale.

As indicated by the GRF_{cost} previously reported, the vertical ground reaction force improved relative to the reference data. In Figure 42 one may note that a double peak has been formed, though it is not smooth. Some of the sharp portions

(a) Hip Displacement (b) Hip Angle

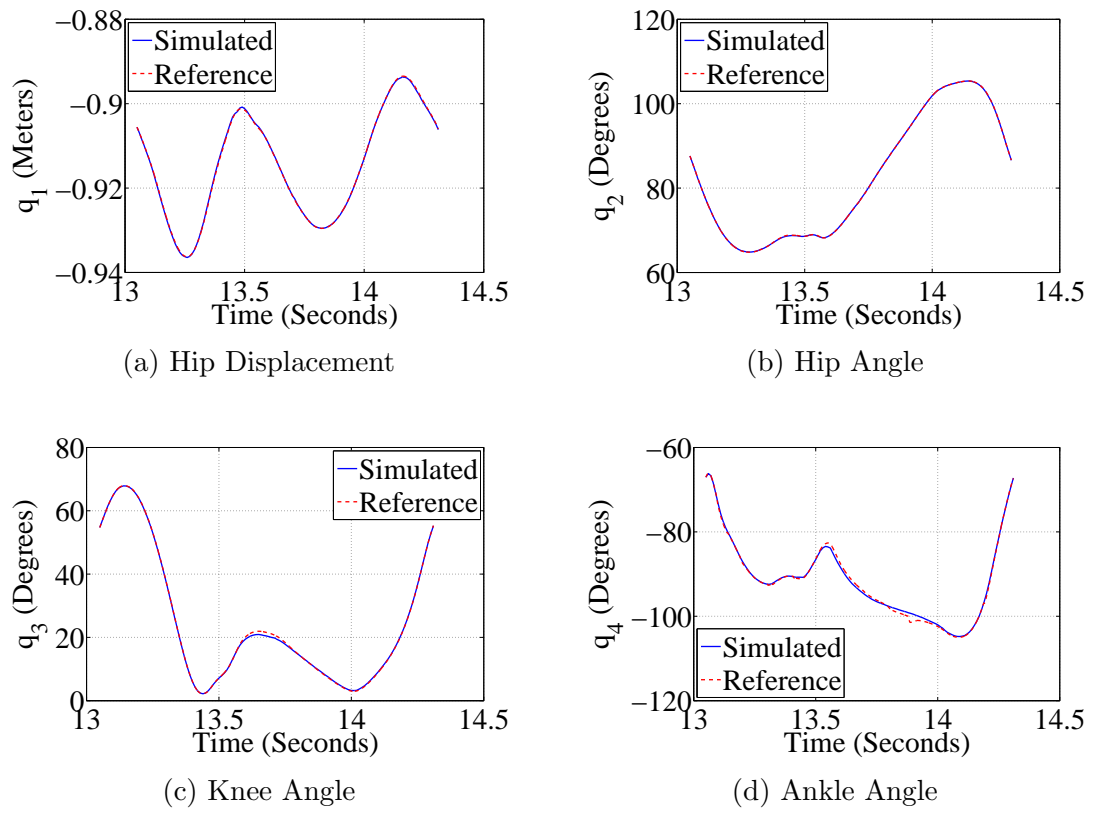(c) Knee Angle (d) Ankle Angle

Figure 41: Example tracking results from Trial 1 optimization
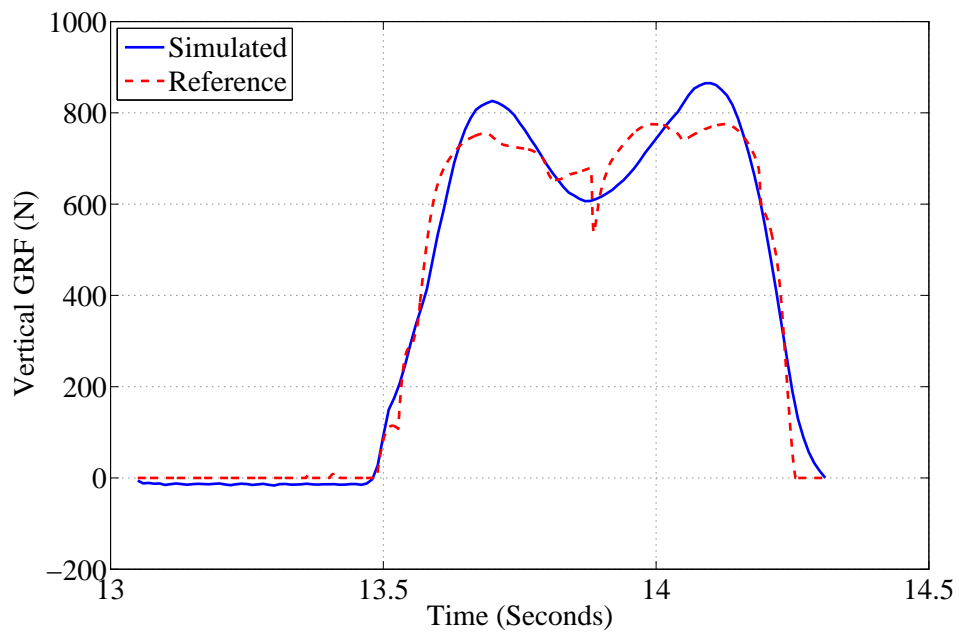

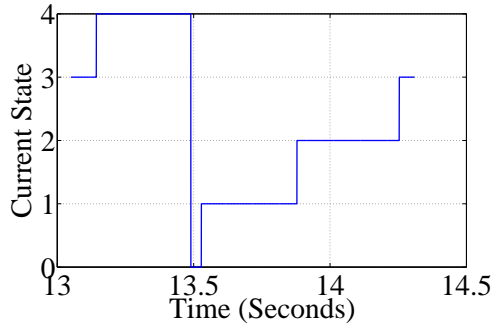Figure 42: Example vertical GRF results from Trial 1 optimization

Figure 43: Example state switching results from Trial 1 optimization

of the GRF curve may be associated with the diversions of the ankle joint from its intended trajectory.

Based upon the previously presented figures, one may consider the accuracy of the state switching method. The timing of the states is presented in Figure 43. No bouncing between states is observed. Each of the states are dwelt upon for a period of time.

In designing a controller one must consider the required control efforts. Figure 44 illustrates the control signal profiles. The preprocessed three-dimensional estimates of the required joint effort may be used to provide a baseline comparison between these control torques and those used by the human subject. This data is available for the hip torque, knee torque, and ankle torque. A peak magnitude of 27 Nm is given for the hip torque. The control signal peak is multiples larger than the reference. Comparing the peak knee torque to the reference peak, it is more than ten times the magnitude of the reference value, 44 Nm. The peak ankle torque, ignoring the instantaneous spike, is consistently less than the reference peak, 160 Nm. It is possible that this is related to the fact that the ankle showed the most impedance controlled-like behavior.
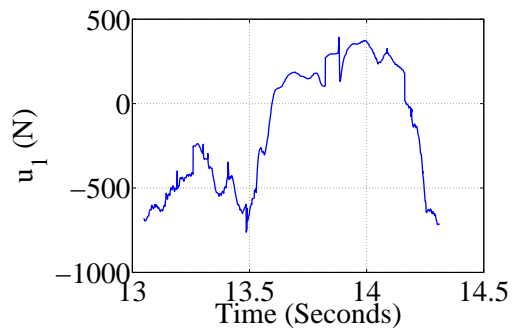
(a) Hip Control Force
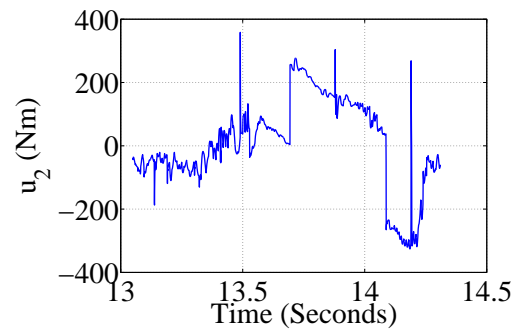
(b) Hip Control Torque
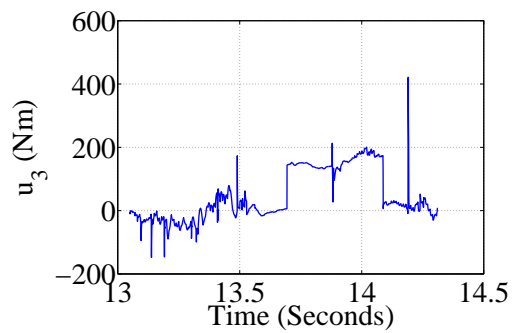
(c) Knee Control Torque
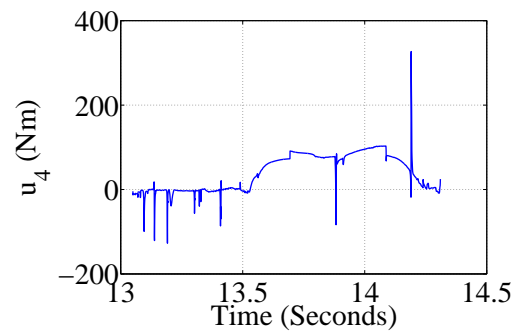
(d) Ankle Control Torque

Figure 44: Example control signal results from Trial 1 optimization
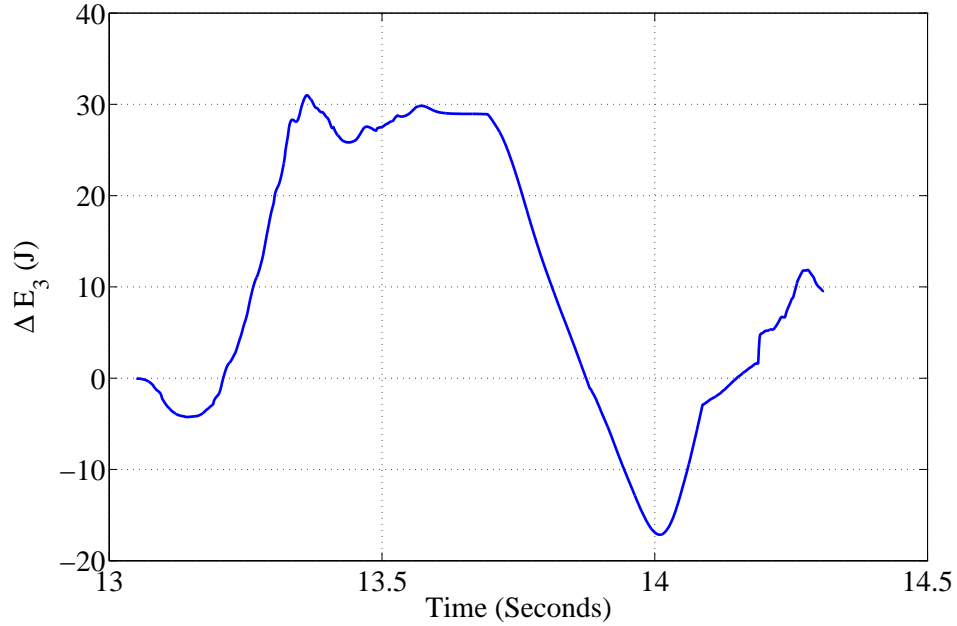
Figure 45: Example ΔE_3 results from Trial 1 optimization

Lastly, the energy profile was evaluated. It is shown in Figure 45. The general shape of the profile is fairly consistent with the result of integrating the reference power data, though the magnitude is greater because it is dependent on u_3. Furthermore, the timing of the largest positive change in energy corresponds with the latter part of swing phase. There is also an small increase associated with the early portion of stance phase. These are two of the typical periods when excess energy is typically dissipated. The other significant rise is early swing phase as the gait cycle approaches toe off. The remainder of the shape is associated with various periods of energy usage [52].

5.7 Discussion

Two ideas that have each been previously applied to prosthesis control, namely robust tracking/impedance control and switched impedance control, have been combined. The resulting controller was optimized. Throughout the process and

within the results it is clear that there is much room for further development.

There are multiple limitations to the modeling process. While the model was expanded to use the limb lengths of the subject rather than all robotic parameters, the masses, locations of the centers of mass, and moments of inertia remained unchanged from the original robot model. It may be due to these inconsistencies that some results of the simulation do not match the reference data better.

In addition, the control efforts, particularly those associated with the hip joint, have the potential of being high because of the tuning of the tracking portion of the controller. The goal of such a controller is following a trajectory regardless of external influences. Therefore, excessive force or torque may be used.

Improvements of the optimization portion of this work may be addressed in several ways. First, an excessive amount of computation time was required for one trial. By estimation this time may be reduced by at least a factor of 10 on a 24 core computer. Development of the optimization within a formal multi-objective framework may also be beneficial. By this means the balance of objectives could be more easily defined. Finally, extending the optimization across multiple gait cycles would encourage robustness of the controller.

In conclusion, the switched robust tracking/impedance controller was successful in meeting each of the proposed optimization goals. Accurate tracking was obtained in simulation. GRF was also realistic. Lastly, the excess energy typically seen within a natural knee joint was replicated, providing the opportunity to consider energy regeneration within lower limb prostheses.

CHAPTER VI

CONCLUSIONS AND FUTURE WORK

In conclusion, the goal of completing several steps in the design process of an electrically regenerative active knee and ankle prosthesis has been met. A complete crank-slider actuator system traversing from knee joint to supercapacitor has been evaluated and proven its capacity for energy regeneration in simulation. This process was completed in three consecutive models. First, a basic model to consider energy regeneration within the crank-slider actuator was optimized and validated. Secondly, a model including a screw geometry-based friction function was evaluated and indicated energy regeneration even with the inclusion of mechanical losses. Lastly, a generalized mechanical loss term was introduced in place of the complex friction function to form an actuator that could be optimized while yet including mechanical losses. This model also resulted in successful energy regeneration. The succession of these actuator models provides support for the possibility of using a crank-slider actuator to drive a prosthetic knee joint while harvesting energy.

To consider the controller of a prosthesis within a simulation environment ranging from the natural hip joint to contact with the ground, an improved two-dimensional ground contact model was completed. A contact model dependent on constant threshold and stiffness values was included within the combined hip robot and prosthetic leg simulation. While the approach was sufficient in the original case,

it was not adaptable to a variety of reference data sets. This low level of flexibility led to the development of a novel ground contact model. In addition to developing a method of optimizing the contact model for each subject and dataset, a damping term was added to the ground contact model to facilitate a more natural level of heel contact force and better timing of the heelstrike condition. The resulting contact model proved sufficiently accurate to use in a two-dimensional simulation of the leg for controller testing.

Lastly, a novel control strategy for the leg was presented. In this controller an established method, robust tracking/impedance control, was used as the foundation, and the known variable impedance of the human system was added by considering a previously developed impedance switching prosthesis controller. Implementation consisted of the hip joint of the hip robot and prosthesis system being driven solely by a robust passivity-based controller and the knee and ankle joints being controlled by the robust/tracking impedance controller. The gains for the two lower joint controllers were determined through a state switching algorithm with a total of five states. These gains were optimized for tracking at the knee and ankle joints, ground reaction force tracking, and energy regeneration. Across five trials good tracking was obtained along with the desired energy regeneration.

Future Work

In addition to the improvements mentioned under each individual topic there are several broader opportunities for future work. First, the contact model and controller may be extended to describe and handle stairs, slopes, and other terrain. This process would consist of several steps. Reference data for any task of interest must be collected and processed in a two-dimensional framework. This would be followed by defining the threshold as a function of the data that could be vertically shifted rather than shifting solely a constant. For slopes such a function could easily be a line. For

steps and other terrain it may need to be defined piecewise. New optimizations would then be required according to dataset to determine the contact model parameters. Extending the simulation in this way provides a means to test the prosthesis design across a variety of activities of daily living.

Each of the optimizations performed should be formally evaluated for parameter sensitivity. For example, within the actuator system portion of this work it is possible that the capacitance may not effect energy regeneration. Furthermore, there is a level of dependence between the geometric parameters of the crank-slider design. Completion of such an analysis would provide insight into the effects of each parameter and perhaps provide a means of reducing the number of optimization variables.

Also, the actuator model may be transposed into the combined hip robot and prosthesis simulation. For the knee joint this process may be completed with the actuator model's current formulation. Adjustments to the model to align coordinate systems would be required to add the actuator to the ankle joint. This combination would change the control variable from joint torques to the transformer modulus u, introducing the semi-active modulation method of control in both joints. Alongside the development of the actuator system, a power management system design must be prepared. Such a system, generally speaking, should control the transfer of energy in and out of multiple capacitors, particularly from the knee to the ankle. A battery is also a likely component within this system as a self-powering state is unlikely, especially considering high energy expenditure activities such as climbing a flight of stairs.

Combined with mechanical design work, the resulting model could then be prototyped. Following the creation of a prototype, experimental testing of the switched robust tracking/impedance controller may be completed with use of the hip robot hardware, making further validation of the simulations of this work possible. Successful testing with the hip robot would lend itself to testing with an able-bodied

subject by use of a bent-leg adapter. The goal would then be to progress to clinical testing with amputees.

Finally, it has been shown in the literature that the impedance displayed at human joints is a continuous variable [24]. Accordingly, the switching of the controller may be extended into a continuous function. This may be a function of both kinematic and kinetic variables at the joints. A significant amount of further study and likely experimental work would be required to better classify this function and successfully reproduce it within a controller. Mirroring able-bodied joint impedance should further the objective of producing able-bodied gait through a prosthetic leg. Each of these extensions will take the ideas presented in this work a step closer to an energy regenerative, powered transfemoral prosthetic system capable of replicating natural gait.

BIBLIOGRAPHY

[1] Marko Ackermann and Antonie van den Bogert. Optimality principles for model-based prediction of human gait. Journal of Biomechanics, 43(6):1055–1060, April 2010.

[2] Thierry Chevalier, Helen Hidgins, and Nachiappan Chockalingam. Plantar pressure measurements using an in-shoe system and a pressure platform: A comparison. Gait & Posture, 31(3):397–399, March 2010.

[3] Snehal Chokhandre, Jason Halloran, Antonie van den Bogert, and Ahmet Erdemir. A three-dimensional inverse finite element analysis of the heel pad. Journal of Biomechanical Engineering, 134(3):031002–1–031002–9, March 2012.

[4] Steven Collins and Arthur Kuo. Recycling energy to restore impaired ankle function during human walking. PLoS One, 5(2):e9307, February 2010.

[5] Juan Dixon, Ian Nakashima, Eduardo Arcos, and Micah Ortúzar. Electric vehicle using a combination of ultracapacitors and ZEBRA battery. IEEE Transactions on Industrial Electronics, 57(3):943–949, March 2010.

[6] Russell Eberhart and James Kennedy. A new optimizer using particle swarm theory. In Proceedings of the Sixth International Symposium on Micro Machine and Human Science, pages 39–43, Nagoya, Japan, 1995.

[7] Centers for Disease Control and Prevention. Number (in thousands) of hospital discharges for nontraumatic lower extremity amputation with diabetes as a listed diagnosis, United States, 1988-2009, 2012. http://www.cdc.gov/diabetes/statistics/lea/fig1.htm, accessed July 14, 2015.

[8] Robert Gailey, Kerry Allen, Julie Castle, Jennifer Kucharik, and Mariah Roeder. Review of secondary physical conditions associated with lower-limb amputation and long-term prosthesis use. Journal of Rehabilitation Research & Development, 45(1):15–29, 2008.

[9] Joost Geeroms, Louis Flynn, Rene Fabian, Bram Vanderborght, and Dirk Lefeber. Ankle-knee prosthesis with powered ankle and energy transfer for CY-BERLEGs α-prototype. In Proceedings of the IEEE International Conference on Rehabilitation Robotics, pages 1–6, Seattle, Washington, June 2013.

[10] Amit Gefen, Michal Megido-Ravid, Yacov Itzchak, and Mircea Arcan. Biomechanical analysis of the three-dimensional foot structure during gait: A basic tool for clinical applications. Journal of Biomechanical Engineering, 122(6):630–639, July 2000.

[11] Andrew Gitter, Joseph Czerniecki, and Kelly Weaver. A reassessment of center-of-mass dynamics as a determinate of the metabolic inefficiency of above-knee amputee ambulation. American Journal of Physical Medicine & Rehabilitation, 74(5):332–338, 1995.

[12] Brian Hafner, Laura Willingham, Noelle Buell, Katheryn Allyn, and Douglas Smith. Evaluation of function, performance, and preference as transfemoral amputees transition from mechanical to microprocessor control of the prosthetic knee. Archives of Physical Medicine and Rehabilitation, 88(4):207–217, April 2007.

[13] Zach Harvey, Benjamin Potter, James Vandersea, and Erik Wolf. Prosthetic advances. Journal of Surgical Orthopaedic Advances, 21(1):58–64, 2012.

[14] Neville Hogan. Impedance control: An approach to manipulation: Part I—Theory. Journal of Dynamic Systems, Measurement, and Control, 107(1):1–7, March 1985.

[15] Neville Hogan. Impedance control: An approach to manipulation: Part II—Implementation. Journal of Dynamic Systems, Measurement, and Control, 107(1):8–16, March 1985.

[16] Neville Hogan. Impedance control: An approach to manipulation: Part III—Applications. Journal of Dynamic Systems, Measurement, and Control, 107(1):17–24, March 1985.

[17] Hual-Te Huang and B. Ravani. Contact stress analysis in ball screw mechanism using the tubular medial axis representation of contacting surfaces. Journal of Mechanical Design, 119(1):8–14, March 1997.

[18] Nook Industries. PowerTrac 0631-0200 SRT RA, with SEL ball nut, adjustable preloaded product specification sheet. http://www.nookindustries.com/Product/ProductSpec/106544, accessed July 22, 2015.

[19] Jenniver Johansson, Delsey Sherrill, Patrick Riley, Paolo Bonato, and Hugh Herr. A clinical comparison of variable-damping and mechanically passive prosthetic knee devices. American Journal of Physical Medicine & Rehabilitation, 84(8):563–575, August 2005.

[20] Amin Kamalzadeh. Precision Control of High Speed Ball Screw Drives. Dissertation, University of Waterloo, 2008.

[21] Dean Karnopp, Donald Margolis, and Ronald Rosenberg. System Dynamics: Modeling, Simulation, and Control of Mechatronic Systems. Wiley, fifth edition, 2012.

[22] Yuichi Kitagawa, Hideaki Ichikawa, Albert King, and Paul Begeman. Development of a human ankle/foot model. In Janusz Kajzer, Eiichi Tanaka, and Hiroshi Yamada, editors, Human Biomechanics and Injury Prevention, pages 117–122. Springer, 2015.

[23] Chad Krueger, Joseph Wenke, and James Ficke. Ten years at war: Comprehensive analysis of amputation trends. Journal of Trauma and Acute Care Surgery, 73(6):S438–S444, December 2012.

[24] Daniel Ludvig and Eric Perreault. Task-relevant adaptation of musculoskeletal impedance during posture and movement. In Proceedings of the American Control Conference, pages 4784–4789, Portland, Oregon, 2014.

[25] Chris McGibbon and David Krebs. Discriminating age and disability effects in locomotion: Neuromuscular adaptations in musculoskeletal pathology. Journal of Applied Physiology, 96(1):149–160, January 2004.

[26] Terry McNier and Jeff Johnson. Specifying, Selecting and Applying Linear Ball Screw Drives.

[27] Hylton Menz and Meg Morris. Clinical determinants of plantar forces and pressures during walking in older people. Gait & Posture, 24(2):229–236, October 2006.

[28] Hadis Mohammadi and Hanz Richter. Robust tracking/impedance control: Application to prosthetics. In Proceedings of the American Control Conference, Chicago, Illinois, 2015.

101

[29] Robert L. Norton. Design of Machinery. McGraw-Hill Education, fifth edition, 2011.

[30] Dumitru Olaru, George Puiu, Liviu Balan, and Vasile Puiu. A new model to estimate friction torque in a ball screw system. In Doru Talab and Thomas Roche, editors, Product Engineering, pages 333–346. Springer Netherlands, 2005.

[31] Össur. The new power knee, 2010. http://assets.ossur.com/lisalib/getfile.aspx?itemid=22240, accessed July 14, 2015.

[32] Jarmo Perttunen. Foot Loading in Normal and Pathological Walking. Dissertation, University of Jyväskylä, 2002.

[33] Rick Rarick, Hanz Richter, Antonie van den Bogert, Dan Simon, Holly Warner, and Taylor Barto. Optimal design of a transfemoral prosthesis with energy storage and regeneration. In Proceedings of the American Control Conference, pages 4108–4113, Portland, Oregon, 2014.

[34] Hanz Richter. A framework for control of robots with energy regeneration. Journal of Dynamic Systems, Measurement, and Control, 137(9):091004–1–091004–11, September 2015.

[35] Hanz Richter and Dhipak Selvaraj. Impedance control with energy regeneration in advanced exercise machines. In Proceedings of the American Control Conference, Chicago, Illinois, 2015.

[36] Hanz Richter, Dan Simon, William Smith, and Sergey Samorezov. Dynamic modeling, parameter estimation, and control of a leg prosthesis test robot. Applied Mathematical Modelling, 39(2):559–573, January 2014.

[37] Hanz Richter, Dan Simon, and Antonie van den Bogert. Semiactive virtual control method for robots with regenerative energy-storing joints. In Proceedings

of the 19th IFAC World Congress, pages 10244–10250, Cape Town, South Africa, 2014.

[38] Ava Segal, Michael Orendurff, Glenn Klute, Martin McDowell, Janice Pecoraro, Jane Shofer, and Joseph Czerniecki. Kinematic and kinetic comparisons of transfemoral amputee gait using c-leg and mauch sns prosthetic knees. Journal of Rehabilitation & Development, 43(7):857–870, November 2006.

[39] Bhartendu Seth. Energy Regeneration and its Application to Active Above-Knee Prostheses. Dissertation, Massachusetts Institute of Technology, 1987.

[40] Dan Simon. Biogeography-based optimization. IEEE Transactions on Evolutionary Computation, 12(6):702–713, December 2008.

[41] Dan Simon. Evolutionary Optimization Algorithms. Wiley, 2013.

[42] Alexander Slocum. Precision Machine Design. Prentice-Hall, 1992.

[43] Mark Spong, Seth Hutchinson, and M. Vidyasagar. Robot Modeling and Control. Wiley, 2006.

[44] Pieter Struyf, Caroline van Heugten, Minou Hitters, and Rob Smeets. The prevalence of osteoarthritis of the intact hip and knee among traumatic leg amputees. Archives of Physical Medicine and Rehabilitation, 90(3):440–446, April 2009.

[45] Frank Sup, Huseyin Varol, and Michael Goldfarb. Upslope walking with a powered knee and ankle prosthesis: Initial results with an amputee subject. IEEE Transactions on Neural Systems and Rehabilitation Engineering, 19(1):71–78, February 2011.

[46] Frank Sup, Huseyin Varol, Jason Mitchell, Thomas Withrow, and Michael Goldfarb. Self-contained powered knee and ankle prosthesis: Initial evaluation on a

transfemoral amputee. In Proceedings of the IEEE International Conference on Rehabilitation Robotics, pages 638–644, Kyoto, Japan, 2009.

[47] Jindřich Sušeň. A study on the ball screw friction torque. In Proceedings of the Student's Conference, Prague, Czech Republic, 2011.

[48] Keith Tabor. The Real-Time Digital Control of a Regenerative Above-Knee Prosthesis. Thesis, Massachusetts Institute of Technology, 1988.

[49] Michael Tucker and Kevin Fite. Mechanical damping with electrical regeneration for a powered transfemoral prosthesis. In Proceedings of the IEEE/ASME International Conference on Advanced Intelligent Mechatronics, pages 13–18, Montréal, Canada, 2010.

[50] Antonie van den Bogert, Sergey Samorezov, Brian Davis, and William Smith. Modeling and optimal control of an energy-storing prosthetic knee. Journal of Biomechanical Engineering, 134(5):051007–1–051007–8, May 2012.

[51] Antonie van den Bogert and Anne Su. A weighted least squares method for inverse dynamic analysis. Computer Methods in Biomechanics and Biomedical Engineering, 11(1):3–9, February 2008.

[52] David Winter. Energy generation and absorption at the ankle and knee during fast, natural, and slow cadences. Clinical Orthopaedics and Related Research, (175):147–154, May 1983.

[53] Jia Yu, Duo Wai-Chi Wong, and Ming Zhang. Dynamic foot model for impact investigation. In Ming Zhang and Yubo Fan, editors, Computational Biomechanics of the Musculoskeletal System. Taylor & Francis Group, 2015.

APPENDICES

APPENDIX A

Bond Graph Theory Synopsis

The bond graph method was selected as the primary approach to modeling the actuator system in Chapter III. It is a tool used less frequently in deriving a system's dynamic equation description than free body diagramming, Lagrangian mechanics, or Kirchoff's voltage and current laws, for example. Therefore, a brief description of the terminology and methods of bond graphs is presented.

As previously stated, the premise of the bond graph modeling method is the conservation of power. The development of a bond graph at a high level simply consists of using power bonds, which denote the direction of power transmission and causality, to join a set of generalized elements. The final product is a bond graph in which all of the information necessary to systematically derive a set of state equations is contained.

One may visualize the power bonds as carrying two separate "substances," effort and flow, traveling in opposite directions. Physically, in the mechanical domain effort is equivalent to force or torque; in the electrical domain a parallel may be drawn between effort and voltage. Flow is the same as linear or angular velocity in the mechanical domain and current in the electrical domain. Other domains may similarly be discussed. The multiplication of any pair of effort and flow variables for a given bond yields the power of the bond.

Additional information carried by the power bonds include causality and power direction. Causality is denoted on a power bond by a short, perpendicular stroke at the end of the bond. This indicates that the effort variable is input to the element on the same side as the stroke. By elimination, because effort and flow travel in opposite directions, the element on the other side of the bond must receive the flow variable as its input. Finally, each power bond includes a half arrow at one end. The half arrow indicates the convention for positive power flow. Any time that multiplication of the effort and flow variables yields a positive value, the power flow is in the direction of the half arrow; a negative value would indicate power flow opposite the half arrow.

The bond graph framework defines three primary element classes, 1-port elements, 2-port elements, and 3-port junction elements. The 1-port elements include I, C, R, SE, and SF. While these elements may be used to represent components in domains other than the mechanical and electrical domains, these two domains are the applicable ones for this work. Therefore, an interpretation of these elements within only these two domains will be presented. First, the I element can be used to represent inertia, mass, or inductance, relating momentum and velocity or flux-linkage and current, dependent on the domain. Secondly, the C element can be used to represent stiffness or capacitance, relating displacement and force or charge and voltage. Next, the R element can be used to represent damping or resistance, relating velocity and force or current and voltage. Fourth, the SE element is used as a source of effort to the bond graph. Lastly, the SF element applies a specified flow to the bond graph.

Two 2-port elements are utilized for the construction of bond graphs, the transformer TF and the gyrator GY. In the case of the transformer TF a modulus value is used to relate the effort on one side of the TF element to the effort on the opposite side. Likewise, the flow on one side is related to the flow on the opposite

side by the same value. One example case for which a TF element may be used is in describing a gearset. The GY element is used to relate the effort on one side of the GY element to the flow on the opposite side and vice versa by a modulus value. Perhaps the best example of this element is a DC motor. There is a direct relationship between the voltage, an effort variable, and velocity, a flow variable. The same type of relationship may be described between the current, a flow variable, and the torque, an effort variable. Expanding upon these concepts briefly, a modulated transformer MTF and modulated gyrator MGY may be defined. In this case the modulus is no longer held constant but is a function. A continuously variable transmission exemplifies this case for a MTF element. A temperature-sensitive transducer could be an application of the MGY element.

The final class of elements fundamental to bond graphs are the 3-port junction elements. There are two elements altogether, the 1-junction and the 0-junction. Though these elements are termed 3-port junction elements, they may have more than three ports; three is a minimum. The 1-junction represents a common flow. All bonds attaching to this element carry the same flow, and the incoming effort of one bond is divided between the other bonds. Conversely, the 0-junction element describes a common effort among the connecting bonds. The incoming flow of one bond is divided among the remaining bonds in this case.

Upon completing a bond graph composed of these elements, the states of the system and any algebraic loops may be identified. This may then be followed by derivation of the system's differential equations in a well-defined and primarily algebraic manner. Each of the elements and junctions provide either one or two equations to the overall set. By writing out and combining these equations in an algorithmic manner, the state equations are determined. The final result is posed in such a way that it is straightforward to simulate for most cases.

APPENDIX B

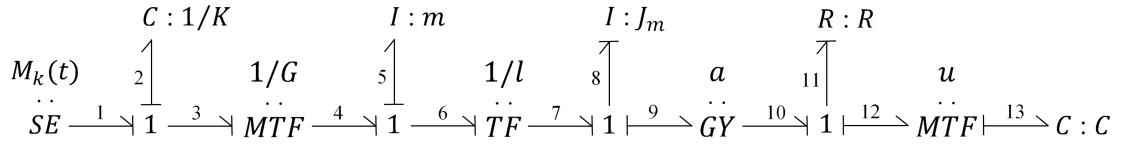# Basic Model Bond Graph Dynamic Equation Derivation

Figure 46: Reference bond graph for derivation of basic system model dynamic equations

The dynamic equations of the simplest actuator model of Section 3.1.2, referred to as the basic model, are derived here. There a total of three states, corresponding to three separate equations. The derivation of each equation is completed in the notation of the bond graph variables. Physical variable notation is then substituted.

Derive first state space equation:

$$\dot{q}_2 = f_2 = f_3 = Gf_4 = Gf_6 = Glf_7 = Glf_8 = Gl\frac{p_8}{J_m} \tag{B.1}$$

Derive second state space equation:

$$\dot{p}_8 = e_8 = e_7 - e_9 = le_6 - \alpha f_{10}$$

$$= l\left(e_4 - e_5\right) - \alpha f_{11} = l\left(Ge_3 - e_5\right) - \frac{\alpha}{R}e_{11}$$

$$= l\left(G\left(e_1 - e_2\right) - e_5\right) - \frac{\alpha}{R}\left(e_{10} - e_{12}\right)$$

$$= l\left(G\left(M_k\left(t\right) - Kq_2\right) - e_5\right) - \frac{\alpha}{R}\left(\alpha f_9 - ue_{13}\right) \tag{B.2}$$

$$= l\left(G\left(M_k\left(t\right) - Kq_2\right) - e_5\right) - \frac{\alpha}{R}\left(\alpha f_8 - u\frac{q_{13}}{C}\right)$$

$$= l\left(G\left(M_k\left(t\right) - Kq_2\right) - e_5\right) - \frac{\alpha}{R}\left(\alpha\frac{p_8}{J_m} - u\frac{q_{13}}{C}\right)$$

$$= lGM_k\left(t\right) - lGKq_2 - le_5 - \frac{\alpha^2}{RJ_m}p_8 + \frac{\alpha u}{RC}q_{13}$$

Require e_5 from derivative causality to complete (B.2):

$$p_5 = mf_5 = mf_6 = mlf_7 = mlf_8 = \frac{ml}{J_m}p_8 \tag{B.3}$$

Taking time derivative:

$$e_5 = \dot{p}_5 = \frac{ml}{J_m}\dot{p}_8 \tag{B.4}$$

Substituting (B.4) into (B.2):

$$\dot{p}_8 = lGM_k\left(t\right) - lGKq_2 - \frac{ml^2}{J_m}\dot{p}_8 - \frac{\alpha^2}{RJ_m}p_8 + \frac{\alpha u}{RC}q_{13} \tag{B.5}$$

Solving for $\dot{p}_8$:

$$\dot{p}_8 = \left(\frac{J_m}{J_m + ml^2}\right)\left(-\frac{\alpha^2}{RJ_m}p_8 - lGKq_2 + \frac{\alpha u}{RC}q_{13} + lGM_k\left(t\right)\right) \tag{B.6}$$

Derive third state space equation:

$$
\begin{aligned}
\dot{q}_{13} = f_{13} = u f_{12} = u f_{11} &= \frac{u}{R} e_{11} = \frac{u}{R} \left(e_{10} - e_{12} \right) = \frac{u}{R} \left(\alpha f_9 - u e_{13} \right) \\
&= \frac{u}{R} \left(\alpha f_8 - u \frac{q_{13}}{C} \right) = \frac{u}{R} \left(\alpha \frac{p_8}{J_m} - u \frac{q_{13}}{C} \right) = -\frac{u^2}{RC} q_{13} + \frac{\alpha u}{R J_m} p_8
\end{aligned}
\tag{B.7}
$$

Change of variables:

$q_2 = \phi_k$, knee angle

$p_8 = J_m \dot{\theta}_m$, motor momentum

$q_{13} = q_C$, capacitor charge

Taking time derivatives:

$\dot{q}_2 = \dot{\phi}_k$, knee angular velocity

$\dot{p}_8 = J_m \ddot{\theta}_m$, motor inertial force

$\dot{q}_{13} = \dot{q}_C = i_C$, capacitor current

Substitute change of variables and simplify to form final set of equations:

$$
\dot{\phi}_k = Gl\dot{\theta}_m
\tag{B.8}
$$

$$
\ddot{\theta}_m = \frac{1}{J_m + ml^2} \left(-\frac{\alpha^2}{R} \dot{\theta}_m - lGK\phi_k + \frac{\alpha u}{RC} q_C + lGM_k \left(t \right) \right)
\tag{B.9}
$$

$$
i_C = -\frac{u^2}{RC} q_C + \frac{\alpha u}{R} \dot{\theta}_m
\tag{B.10}
$$

APPENDIX C

Basic Model u-Inversion

An open-loop control method (Section 3.2) was selected for the actuator simulations. This required the computation of the control variable u from known information, an application of the method from [35]. The associated process is given here for the basic actuator model, which is presented as an example case.

Starting from the system equations:

$$\dot{\phi}_k = Gl\dot{\theta}_m \tag{C.1}$$

$$\ddot{\theta}_m = \frac{1}{J_m + ml^2}\left(lGM_k\left(t\right) - lGK\phi_k - \frac{\alpha^2}{R}\dot{\theta}_m + \frac{\alpha u}{RC}q_C\right) \tag{C.2}$$

$$i_C = \frac{\alpha u}{R}\dot{\theta}_m - \frac{u^2}{RC}q_C \tag{C.3}$$

Multiply (C.3) by q_C:

$$q_C i_C = \frac{\alpha u}{R}q_C\dot{\theta}_m - \frac{u^2}{RC}q_C^2 \tag{C.4}$$

Integrate (C.4) with respect to time:

$$\int_0^t q_C i_C d\tau = \int_0^t \left(\frac{\alpha u}{R}q_C\dot{\theta}_m - \frac{u^2}{RC}q_C^2\right) d\tau \tag{C.5}$$

112

Perform change of variables, $q_C = x_3$, $i_C = \dot{x}_3$:

$$\int_0^t x_3 \dot{x}_3 d\tau = -\frac{1}{RC} \int_0^t (ux_3)^2 d\tau + \frac{\alpha}{R} \int_0^t (ux_3) \dot{\theta}_m d\tau \tag{C.6}$$

Continue integration:

$$\frac{1}{2} \left(x_3(t)^2 - x_3(0)^2 \right) = -\frac{1}{RC} \int_0^t (ux_3)^2 d\tau + \frac{\alpha}{R} \int_0^t (ux_3) \dot{\theta}_m d\tau \tag{C.7}$$

Solve for $x_3(t)$:

$$x_3(t)^2 = 2 \left(-\frac{1}{RC} \int_0^t (ux_3)^2 d\tau + \frac{\alpha}{R} \int_0^t (ux_3) \dot{\theta}_m d\tau \right) + x_3(0)^2 \tag{C.8}$$

Solve (C.2) for ux_3, where $x_3 = q_C$:

$$ux_3 = \frac{RC}{\alpha} \left(\left(J_m + ml^2 \right) \ddot{\theta}_m - lGM_k(t) + lGK\phi_k + \frac{\alpha^2}{R} \dot{\theta}_m \right) \tag{C.9}$$

Substitution of (C.9) into (C.8) gives an expression for $x_3(t)^2$ in terms of values that are either known or could be obtained from reference data. Taking the square root of this result provides an expression for $x_3(t)$. Finally, dividing (C.9) by this expression for $x_3(t)$ yields a direct solution for u. The implementation of these final steps can be completed numerically within MATLAB and are, therefore, not shown here.

APPENDIX D

Complex Friction Model Bond Graph Dynamic Equation Derivation
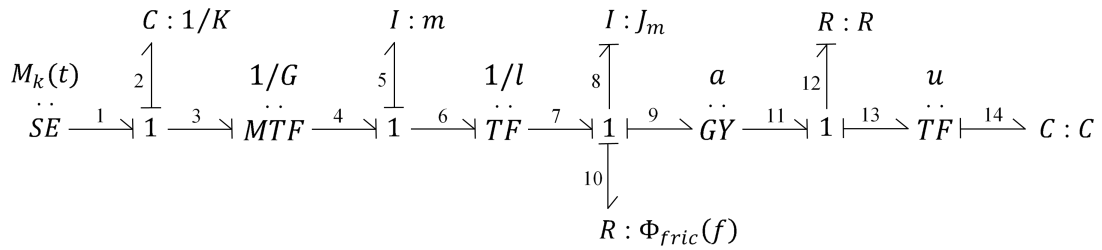
Figure 47: Reference bond graph for the derivation of a system of dynamic equations including the complex friction model

The actuator including the complex friction model from Section 3.1.2 may be described by Figure 47. Three equations may be determined from this bond graph, one for each state. The derivation of each equation is completed in the notation of the bond graph variables. Physical variable notation is then substituted.

Derive first state space equation:

$$\dot{q}_2 = f_2 = f_3 = Gf_4 = Gf_6 = Glf_7 = Glf_8 = Gl\frac{p_8}{J_m} \tag{D.1}$$

Derive second state space equation:

$$
\begin{aligned}
\dot{p}_8 = e_8 = e_7 - e_9 - e_{10} &= le_6 - \alpha f_{11} - \Phi\left(f_{10}\right) \\
&= l\left(e_4 - e_5\right) - \alpha f_{12} - \Phi\left(\frac{p_8}{J_m}\right) \\
&= l\left(Ge_3 - e_5\right) - \frac{\alpha}{R}e_{12} - \Phi\left(\frac{p_8}{J_m}\right) \\
&= l\left(G\left(e_1 - e_2\right) - e_5\right) - \frac{\alpha}{R}\left(e_{11} - e_{13}\right) - \Phi\left(\frac{p_8}{J_m}\right) \\
&= l\left(G\left(M_k\left(t\right) - Kq_2\right) - e_5\right) - \frac{\alpha}{R}\left(\alpha f_9 - ue_{14}\right) - \Phi\left(\frac{p_8}{J_m}\right) \\
&= l\left(G\left(M_k\left(t\right) - Kq_2\right) - e_5\right) - \frac{\alpha}{R}\left(\alpha f_8 - u\frac{q_{14}}{C}\right) - \Phi\left(\frac{p_8}{J_m}\right) \\
&= l\left(G\left(M_k\left(t\right) - Kq_2\right) - e_5\right) - \frac{\alpha}{R}\left(\alpha\frac{p_8}{J_m} - u\frac{q_{14}}{C}\right) - \Phi\left(\frac{p_8}{J_m}\right) \\
&= lGM_k\left(t\right) - lGKq_2 - le_5 - \frac{\alpha^2}{RJ_m}p_8 + \frac{\alpha u}{RC}q_{14} - \Phi\left(\frac{p_8}{J_m}\right)
\end{aligned} \tag{D.2}
$$

Require e_5 from derivative causality to complete (D.2):

$$
p_5 = mf_5 = mf_6 = mlf_7 = mlf_8 = \frac{ml}{J_m}p_8 \tag{D.3}
$$

Taking time derivative of (D.3):

$$
e_5 = \dot{p}_5 = \frac{ml}{J_m}\dot{p}_8 \tag{D.4}
$$

Substituting (D.4) into (D.2):

$$
\dot{p}_8 = lGM_k\left(t\right) - lGKq_2 - \frac{ml^2}{J_m}\dot{p}_8 - \frac{\alpha^2}{RJ_m}p_8 + \frac{\alpha u}{RC}q_{14} - \Phi\left(\frac{p_8}{J_m}\right) \tag{D.5}
$$

Solving (D.5) for $\dot{p}_8$:

$$
\dot{p}_8 = \left(\frac{J_m}{J_m + ml^2}\right)\left(-\frac{\alpha^2}{RJ_m}p_8 - lGKq_2 + \frac{\alpha u}{RC}q_{13} + lGM_k\left(t\right) - \Phi\left(\frac{p_8}{J_m}\right)\right) \tag{D.6}
$$

Derive third state space equation:

$$
\begin{aligned}
\dot{q}_{14} = f_{14} = u f_{13} = u f_{12} &= \frac{u}{R} e_{12} = \frac{u}{R} \left(e_{11} - e_{13} \right) = \frac{u}{R} \left(\alpha f_9 - u e_{14} \right) \\
&= \frac{u}{R} \left(\alpha f_8 - u \frac{q_{14}}{C} \right) = \frac{u}{R} \left(\alpha \frac{p_8}{J_m} - u \frac{q_{14}}{C} \right) = -\frac{u^2}{RC} q_{14} + \frac{\alpha u}{R J_m} p_8
\end{aligned}
\tag{D.7}
$$

Change of variables:

$q_2 = \phi_k$, knee angle

$p_8 = J_m \dot{\theta}_m$, motor momentum

$q_{14} = q_C$, capacitor charge

Taking time derivatives:

$\dot{q}_2 = \dot{\phi}_k$, knee angular velocity

$\dot{p}_8 = J_m \ddot{\theta}_m$, motor inertial force

$\dot{q}_{14} = \dot{q}_C = i_C$, capacitor current

Substitute change of variables and simplify to form final set of equations:

$$
\dot{\phi}_k = Gl\dot{\theta}_m
\tag{D.8}
$$

$$
\ddot{\theta}_m = \frac{1}{J_m + ml^2} \left(-\frac{\alpha^2}{R} \dot{\theta}_m - lGK\phi_k + \frac{\alpha u}{RC} q_C + lGM_k\left(t\right) - \Phi\left(\dot{\theta}_m\right) \right)
\tag{D.9}
$$

$$
i_C = -\frac{u^2}{RC} q_C + \frac{\alpha u}{R} \dot{\theta}_m
\tag{D.10}
$$

APPENDIX E

Generalized Friction Model Bond Graph Dynamic Equation Derivation

Figure 48: Reference bond graph for the derivation of a system of dynamic equations including the generalized friction model

   The system of three equations describing the actuator including the generalized friction model for use in optimization from Section 3.1.2 may be determined from the bond graph in Figure 48. The derivation of each equation is completed in the notation of the bond graph variables. Physical variable notation is then substituted.

Derive first state space equation:

$$\dot{q}_2 = f_2 = f_3 = Gf_4 = Gf_6 = Glf_7 = Glf_8 = Gl\frac{p_8}{J_m} \tag{E.1}$$

Derive second state space equation:

$$\dot{p}_8 = e_8 = e_7 - e_9 = \eta l e_6 - \alpha f_{10}$$

$$= \eta l (e_4 - e_5) - \alpha f_{11} = \eta l (Ge_3 - e_5) - \frac{\alpha}{R} e_{11}$$

$$= \eta l (G(e_1 - e_2) - e_5) - \frac{\alpha}{R}(e_{10} - e_{12})$$

$$= \eta l (G(M_k(t) - Kq_2) - e_5) - \frac{\alpha}{R}(\alpha f_9 - ue_{13}) \tag{E.2}$$

$$= \eta l (G(M_k(t) - Kq_2) - e_5) - \frac{\alpha}{R}\left(\alpha f_8 - u\frac{q_{13}}{C}\right)$$

$$= \eta l (G(M_k(t) - Kq_2) - e_5) - \frac{\alpha}{R}\left(\alpha \frac{p_8}{J_m} - u\frac{q_{13}}{C}\right)$$

$$= \eta l G M_k(t) - \eta l G K q_2 - \eta l e_5 - \frac{\alpha^2}{R J_m} p_8 + \frac{\alpha u}{RC} q_{13}$$

Require e_5 from derivative causality to complete (E.2):

$$p_5 = m f_5 = m f_6 = m l f_7 = m l f_8 = \frac{ml}{J_m} p_8 \tag{E.3}$$

Taking time derivative of (E.3):

$$e_5 = \dot{p}_5 = \frac{ml}{J_m} \dot{p}_8 \tag{E.4}$$

Substituting (E.4) into (E.2):

$$\dot{p}_8 = \eta l G M_k(t) - \eta l G K q_2 - \frac{m\eta l^2}{J_m} \dot{p}_8 - \frac{\alpha^2}{R J_m} p_8 + \frac{\alpha u}{RC} q_{13} \tag{E.5}$$

Solving (E.5) for $\dot{p}_8$:

$$\dot{p}_8 = \left(\frac{J_m}{J_m + m\eta l^2}\right)\left(-\frac{\alpha^2}{R J_m} p_8 - \eta l G K q_2 + \frac{\alpha u}{RC} q_{13} + \eta l G M_k(t)\right) \tag{E.6}$$

Derive third state space equation:

$$\dot{q}_{13} = f_{13} = uf_{12} = uf_{11} = \frac{u}{R}e_{11} = \frac{u}{R}\left(e_{10} - e_{12}\right) = \frac{u}{R}\left(\alpha f_9 - ue_{13}\right)$$

$$= \frac{u}{R}\left(\alpha f_8 - u\frac{q_{13}}{C}\right) = \frac{u}{R}\left(\alpha\frac{p_8}{J_m} - u\frac{q_{13}}{C}\right) = -\frac{u^2}{RC}q_{13} + \frac{\alpha u}{RJ_m}p_8 \tag{E.7}$$

Change of variables:

$$q_2 = \phi_k, \text{ knee angle}$$

$$p_8 = J_m\dot{\theta}_m, \text{ motor momentum}$$

$$q_{13} = q_C = i_C, \text{ capacitor charge}$$

Taking time derivatives:

$$\dot{q}_2 = \dot{\phi}_k, \text{ knee angular velocity}$$

$$\dot{p}_8 = J_m\ddot{\theta}_m, \text{ motor inertial force}$$

$$\dot{q}_{13} = \dot{q}_C, \text{ capacitor current}$$

Substitute change of variables and simplify to form final set of equations:

$$\dot{\phi}_k = Gl\dot{\theta}_m \tag{E.8}$$

$$\ddot{\theta}_m = \frac{1}{J_m + m\eta l^2}\left(-\frac{\alpha^2}{R}\dot{\theta}_m - \eta lGK\phi_k + \frac{\alpha u}{RC}q_C + \eta lGM_k\left(t\right)\right) \tag{E.9}$$

$$i_C = -\frac{u^2}{RC}q_C + \frac{\alpha u}{R}\dot{\theta}_m \tag{E.10}$$

APPENDIX F

Ballscrew Datasheet

Identification of a ballscrew was required for the completion of the complex friction model of Section 3.1.2. The complete parameters of the selected ballscrew may be found in the attached datasheet. Of particular interest were the ball circle diameter, lead, maximum load, and preload capacity.

NOOK

PowerTrac 0631 - 0200 SRT RA, with SEL Ball Nut, Adjustable

Call 800-321-7800 or visit us online at www.nookindustries.com to configure and order your PowerTrac 0631 - 0200 SRT RA, with SEL Ball Nut,

2D/3D CAD ONLINE
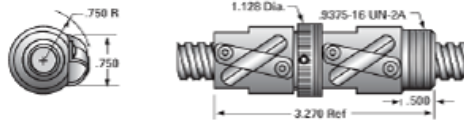
Inch Ball Screw	
Product Info	
Screw Code	0631-0200 SRT RA
Precision	SRT
Screw Material	4150
Thread Direction	RH
Details	
Ball Circle Diameter [in]	0.631
Lead [in]	0.200
Root Diameter [in]	0.500
End Code for Types 1,2,3,5 [* Journals may show tracings of the thread]	12
End Code for Type 4 [* Journals may show tracings of the thread]	8
Performance Specifications	
Lead Accuracy +/- [in./ft.]	0.0040
Part Numbers	
2 ft. Part Number	SRT9392
4 ft. Part Number	SRT9987
6 ft. Part Number	SRT7540
8 ft. Part Number	
12 ft. Part Number	
16 ft. Part Number	
20 ft. Part Number	
Weight	
Screw Weight [lb./ft.]	0.82
Inch Ball Nut, for SRT, Standard Accuracy, Preloaded, Adjustable, SEL	
Product Info	
Ball Nut Number	SEL10408
Thread Direction	RH
Details	
Ball Circle Diameter [in]	0.631
Lead [in]	0.200
Nominal Ball Diameter [in]	0.125
Root diameter [in]	0.500
Forces and Torques	
Torque to Raise 1 lb. [in-lb]	0.035
Flange Part Numbers	
Flange Part Number	FLG7570
Wiper Part Numbers	
Wiper Kit Part Number	WKB10407
Weight	
Nut Weight [lb]	0.65
Performance Specifications	
Lead Accuracy +/- [in./ft.]	0.004
Maximum Adjustable Preload [lb]	233
Spring Rate x 10^6 [lb./in.]	
Dynamic Load [lb]	815
Static Load [lb]	6384

APPENDIX G

Updating the crank-slider modulus G within the energy balance software for the basic actuator model

Within the simulation of the basic actuator (Section 3.3.1) the initial value of the G modulus is required, G_0. It is used to calculate the initial condition of the integrator block outputting the motor velocity $\dot{\theta}_m$. The value G_0 is obtained within the basic actuator model Simulink by selecting the first value of the bbo.ref.G array. This array is pre-calculated during the u-inversion process and simply used within the Simulink. For optimization this approach is suitable and sufficient. However, the energy balance software is setup to be run after the optimization is complete, loading the best solution from a .mat file. Prior to the creation of this file, bbo.ref.G is not updated to reflect the best solution; rather, it contains the G values of the last evaluated solution candidate. Accordingly, when running the Simulink in its original form, the value of G_0 does not match the best solution case. A method has been developed to address this oversight:

1. Load .mat file of interest and run Simulink.

2. Get G_sim(1) after simulation is complete.

3. Replace bbo.ref.G(1) in textbox of bbo.ref.G_0 constant block with G_sim(1) value.

4. Run Simulink again.

5. Run the energy balance code with the workspace resulting from the previous step still loaded.

For all consecutive models, namely the complex friction and efficiency models, of the crank-slider actuator this issue has been addressed within the code.

APPENDIX H

Heel and Toe Jacobians

To determine the external forces applied to the hip robot and prosthesis model as referenced in Section 5.1, the linear velocity Jacobians must be computed. This is completed by taking the time derivatives of the foot kinematic model equations given in Section 2.2.5 and arranging the results in matrix form. This process must be completed for each contact point, the heel and the toe, giving $J_{v,h}$ and $J_{v,t}$.

$$J_{v,h}(1,1) = 0$$

$$J_{v,h}(1,2) = -l_2 \sin(q_2) - l_3 \sin(q_2 + q_3) - aH \sin\left(q_2 + q_3 + q_4 + \left(\frac{\pi}{2} + \cos^{-1}\left(\frac{ah}{aH}\right)\right)\right)$$

$$J_{v,h}(1,3) = -l_3 \sin(q_2 + q_3) - aH \sin\left(q_2 + q_3 + q_4 + \left(\frac{\pi}{2} + \cos^{-1}\left(\frac{ah}{aH}\right)\right)\right)$$

$$J_{v,h}(1,4) = -aH \sin\left(q_2 + q_3 + q_4 + \left(\frac{\pi}{2} + \cos^{-1}\left(\frac{ah}{aH}\right)\right)\right)$$

$$J_{v,h}(2,1) = 1$$

$$J_{v,h}(2,2) = l_2 \cos(q_2) + l_3 \cos(q_2 + q_3) + aH \cos\left(q_2 + q_3 + q_4 + \left(\frac{\pi}{2} + \cos^{-1}\left(\frac{ah}{aH}\right)\right)\right)$$

$$J_{v,h}(2,3) = l_3 \cos(q_2 + q_3) + aH \cos\left(q_2 + q_3 + q_4 + \left(\frac{\pi}{2} + \cos^{-1}\left(\frac{ah}{aH}\right)\right)\right)$$

$$J_{v,h}(2,4) = aH \cos\left(q_2 + q_3 + q_4 + \left(\frac{\pi}{2} + \cos^{-1}\left(\frac{ah}{aH}\right)\right)\right)$$

$$J_{v,t}(1,1) = 0$$

$$J_{v,t}(1,2) = -l_2 \sin(q_2) - l_3 \sin(q_2 + q_3) - aT \sin\left(q_2 + q_3 + q_4 + \left(\frac{\pi}{2} - \cos^{-1}\left(\frac{ah}{aT}\right)\right)\right)$$

$$J_{v,t}(1,3) = -l_3 \sin(q_2 + q_3) - aT \sin\left(q_2 + q_3 + q_4 + \left(\frac{\pi}{2} - \cos^{-1}\left(\frac{ah}{aT}\right)\right)\right)$$

$$J_{v,t}(1,4) = -aT \sin\left(q_2 + q_3 + q_4 + \left(\frac{\pi}{2} - \cos^{-1}\left(\frac{ah}{aT}\right)\right)\right)$$

$$J_{v,t}(2,1) = 1$$

$$J_{v,t}(2,2) = l_2 \cos(q_2) + l_3 \cos(q_2 + q_3) + aT \cos\left(q_2 + q_3 + q_4 + \left(\frac{\pi}{2} - \cos^{-1}\left(\frac{ah}{aT}\right)\right)\right)$$

$$J_{v,t}(2,3) = l_3 \cos(q_2 + q_3) + aT \cos\left(q_2 + q_3 + q_4 + \left(\frac{\pi}{2} - \cos^{-1}\left(\frac{ah}{aT}\right)\right)\right)$$

$$J_{v,t}(2,4) = aT \cos\left(q_2 + q_3 + q_4 + \left(\frac{\pi}{2} - \cos^{-1}\left(\frac{ah}{aT}\right)\right)\right)$$

APPENDIX I

Hip Robot and Prosthesis Dynamic Equations

The hip robot and prosthesis dynamic system model referred to in Section 5.1 is provided below. It is written in terms of the parameters Θ, which are given at the end of the equation set. M is the mass matrix. C is the Coriolis matrix. G is the gravity vector. And R is the loss terms vector.

$$M(1,1) = \Theta_1$$

$$M(1,2) = \Theta_2 \cos(q_2) + \Theta_3 \cos(q_2 + q_3 + q_4) + \Theta_4 \cos(q_2 + q_3)$$

$$M(1,3) = \Theta_3 \cos(q_2 + q_3 + q_4) + \Theta_4 \cos(q_2 + q_3)$$

$$M(1,4) = \Theta_3 \cos(q_2 + q_3 + q_4)$$

$$M(2,1) = M(1,2)$$

$$M(2,2) = \Theta_5 + 2\Theta_6 \cos(q_3 + q_4) + 2\Theta_7 \cos(q_3) + 2\Theta_8 \cos(q_4)$$

$$M(2,3) = \Theta_9 + \Theta_7 \cos(q_3) + 2\Theta_8 \cos(q_4) + \Theta_6 \cos(q_3 + q_4)$$

$$M(2,4) = \Theta_{10} + \Theta_6 \cos(q_3 + q_4) + \Theta_8 \cos(q_4)$$

$$M(3,1) = M(1,3)$$

$$M(3,2) = M(2,3)$$

$$M(3,3) = \Theta_9 + 2\Theta_8 \cos(q_4) + m_4 l_3^2 + I_{3z} + I_{4z}$$

$$M(3,4) = \Theta_{10} + \Theta_8 \cos(q_4)$$

$$M(4,1) = M(1,4)$$

$$M(4,2) = M(2,4)$$

$$M(4,3) = M(3,4)$$

$$M(4,4) = \Theta_{10}$$

$$C(1,1) = 0$$

$$C(1,2) = -\dot{q}_3(\Theta_3 \sin(q_2 + q_3 + q_4) + \Theta_4 \sin(q_2 + q_3))$$
$$- \dot{q}_2(\Theta_2 \sin(q_2) + \Theta_3 \sin(q_2 + q_3 + q_4) + \Theta_4 \sin(q_2 + q_3))$$
$$- \Theta_3 \dot{q}_4 \sin(q_2 + q_3 + q_4)$$

$$C(1,3) = -\dot{q}_2(\Theta_3 \sin(q_2 + q_3 + q_4) + \Theta_4 \sin(q_2 + q_3))$$
$$- \dot{q}_3(\Theta_3 \sin(q_2 + q_3 + q_4) + \Theta_4 \sin(q_2 + q_3)) - \Theta_3 \dot{q}_4 \sin(q_2 + q_3 + q_4)$$

$$C(1,4) = -\Theta_3 \dot{q}_2 \sin(q_2 + q_3 + q_4) - \Theta_3 \dot{q}_3 \sin(q_2 + q_3 + q_4) - \Theta_3 \dot{q}_4 \sin(q_2 + q_3 + q_4)$$

$$C(2,1) = 0$$

$$C(2,2) = -\dot{q}_3(\Theta_6 \sin(q_3 + q_4) + \Theta_7 \sin(q_3)) - \dot{q}_4(\Theta_6 \sin(q_3 + q_4) + \Theta_8 \sin(q_4))$$

$$C(2,3) = -\dot{q}_2(\Theta_6 \sin(q_3 + q_4) + \Theta_7 \sin(q_3)) - \dot{q}_3(\Theta_6 \sin(q_3 + q_4) + \Theta_7 \sin(q_3))$$
$$- \dot{q}_4(\Theta_6 \sin(q_3 + q_4) + \Theta_8 \sin(q_4))$$

$$C(2,4) = -\dot{q}_2(\Theta_6 \sin(q_3 + q_4) + \Theta_8 \sin(q_4)) - \dot{q}_3(\Theta_6 \sin(q_3 + q_4) + \Theta_8 \sin(q_4))$$
$$- \dot{q}_4(\Theta_6 \sin(q_3 + q_4) + \Theta_8 \sin(q_4))$$

$$C(3,1) = 0$$

$$C(3,2) = \dot{q}_2(\Theta_6 \sin(q_3 + q_4) + \Theta_7 \sin(q_3)) - \Theta_8 \dot{q}_4 \sin(q_4)$$

$$C(3,3) = -\Theta_8 \dot{q}_4 \sin(q_4)$$

$$C(3,4) = -\Theta_8 \dot{q}_2 \sin(q_4) - \Theta_8 \dot{q}_3 \sin(q_4) - \Theta_8 \dot{q}_4 \sin(q_4)$$

$$C(4,1) = 0$$

$$C(4,2) = \dot{q}_2(\Theta_6 \sin(q_3 + q_4) + \Theta_8 \sin(q_4)) + \Theta_8 \dot{q}_3 \sin(q_4)$$

$$C(4,3) = \Theta_8 \dot{q}_2 \sin(q_4) + \Theta_8 \dot{q}_3 \sin(q_4)$$

$$C(4,4) = 0$$

$$G(1) = -g\Theta_1$$

$$G(2) = -g(\Theta_2 \cos(q_2) + \Theta_3 \cos(q_2 + q_3 + q_4) + \Theta_4 \cos(q_2 + q_3))$$

$$G(3) = -g\Theta_4 \cos(q_2 + q_3) - g\Theta_3 \cos(q_2 + q_3 + q_4)$$

$$G(4) = -g\Theta_3 \cos(q_2 + q_3 + q_4)$$

$$R(1) = \Theta_{12}\mathrm{sign}(\dot{q}_1)$$

$$R(2) = \Theta_{11}\dot{q}_2$$

$$R(3) = 0$$

$$R(4) = 0$$

$$\Theta_1 = m_1 + m_2 + m_3 + m_4$$

$$\Theta_2 = c_2 m_2 + l_2 m_3 + l_2 m_4$$

$$\Theta_3 = c_4 m_4$$

$$\Theta_4 = c_3 m_3 + l_3 m_4$$

$$\Theta_5 = I_{2z} + I_{3z} + I_{4z} + c_2^2 m_2 + c_3^2 m_3 + c_4^2 m_4 + l_2^2 m_3 + l_2^2 m_4 + l_3^2 m_4$$

$$\Theta_6 = c_4 l_2 m_4$$

$$\Theta_7 = c_3 l_2 m_3 + l_2 l_3 m_4$$

$$\Theta_8 = c_4 l_3 m_4$$

$$\Theta_9 = m_3 c_3^2 + m_4 c_4^2 + m_4 l_3^2 + I_{3z} + I_{4z}$$

$$\Theta_{10} = I_{4z} + c_4^2 m_4$$

$$\Theta_{11} = b$$

$$\Theta_{12} = f$$

APPENDIX J

Optimized Switched Robust
Tracking/Impedance Controller Gains

A total of 50 control gains were optimized as described in Section 5.5. This appendix details a portion of the results of that optimization, Section 5.6. The selected values for each of the 50 gains were tabulated and categorized by state for a total of five optimization trials.

State	Gain	Trial 1	Trial 2	Trial 3	Trial 4	Trial 5
State 0	Λ_3	2104.55	2072.13	1074.12	2897.02	3887.34
	K_3	3510.48	339.96	635.97	3600.80	3627.69
	I_3	0.60	0.44	5.49	3.99	3.30
	b_3	2859.94	5041.61	2975.51	2212.36	1559.57
	k_3	46428.67	55453.93	42016.98	36983.24	24394.90
	Λ_4	1289.75	2711.00	953.03	2786.35	2603.17
	K_4	2760.94	3884.77	3350.25	1124.62	990.47
	I_4	3.08	1.34	0.92	2.04	5.75
	b_4	201.52	289.06	1353.91	2976.18	1195.37
	k_4	662.00	51525.59	57692.63	6193.19	63314.20
State 1	Λ_3	840.20	1180.68	847.62	2608.33	895.00
	K_3	1642.72	249.16	2388.50	3012.43	2293.19
	I_3	5.05	3.63	1.13	2.73	2.48
	b_3	476.70	507.42	264.99	190.86	3431.62
	k_3	5517.38	8505.50	7792.28	2529.88	8554.47
	Λ_4	411.44	1484.58	1799.74	3528.20	2487.95
	K_4	2349.47	3086.26	853.52	3939.37	467.45
	I_4	5.52	3.72	4.75	1.07	2.51
	b_4	1240.47	2994.85	2640.80	522.91	2245.83
	k_4	3715.36	3848.21	4190.58	74395.32	1903.05
State 2	Λ_3	3926.98	1314.79	935.32	1578.02	44.21
	K_3	283.15	999.83	1309.65	2286.33	3958.97
	I_3	1.13	0.63	0.55	4.15	1.88
	b_3	4009.22	1712.07	613.32	4104.68	3074.07
	k_3	19596.31	20026.24	64006.87	58063.54	66237.25
	Λ_4	37.17	810.28	248.95	2782.64	728.87
	K_4	3389.48	447.92	987.10	239.33	889.69
	I_4	2.36	1.55	1.33	3.65	2.75
	b_4	1588.69	1494.52	1933.04	548.65	2036.18
	k_4	42832.44	41845.03	47102.95	68449.88	34863.64
State 3	Λ_3	695.70	488.79	1261.56	1062.97	1677.96
	K_3	3911.88	2989.00	1206.15	1052.94	3860.55
	I_3	1.90	2.36	2.10	0.70	2.89
	b_3	1267.55	1043.15	3530.01	500.00	707.29
	k_3	38853.24	3000.00	51825.81	68264.84	24772.57
	Λ_4	3477.74	2961.47	495.94	3868.01	278.95
	K_4	671.86	2503.44	1390.67	824.59	1338.31
	I_4	3.32	1.35	3.87	3.17	1.89
	b_4	2741.74	1354.73	1306.85	2865.91	1453.44
	k_4	58165.57	47725.56	49530.21	61164.89	19111.19
State 4	Λ_3	1294.74	2431.33	1499.49	1153.22	2967.92
	K_3	816.46	2962.23	2162.88	1960.42	167.88
	I_3	1.00	1.23	2.97	2.09	0.95
	b_3	150.00	4903.62	3037.19	772.85	2137.13
	k_3	55066.01	72544.84	69714.07	72281.89	53811.24
	Λ_4	3540.41	994.05	329.88	2417.60	3032.79
	K_4	310.32	757.90	2741.41	550.00	3572.16
	I_4	2.07	1.17	5.71	3.00	1.63
	b_4	2195.18	1245.47	1350.52	1110.14	2538.19
	k_4	59146.21	13357.86	73791.00	48473.00	69428.06

Table XVII: Control gains resulting from five optimization trials

APPENDIX K

Code Repository

Each of the code suites developed for the contributions of this work are available at the following URL's:

Chapter III: Actuator System Design and Optimization

http://embeddedlab.csuohio.edu/Prosthetics/CrankSliderActuator.html

Chapter IV: Ground Contact Model Design and Optimization

http://embeddedlab.csuohio.edu/Prosthetics/GroundContactModel.html

Chapter V: Control System Design and Optimization

http://embeddedlab.csuohio.edu/Prosthetics/SwitchedRobTrackImpCont.html

APPENDIX L

Copyright Permissions

Several figures as denoted throughout this work were adapted from previous publications of other authors. All were used with permission. For Figures 1 and 2 this permission was granted through an automated system. This process is shown in the first three images. Permission for Figure 6 was granted in writing, which is the final image. The incorporation of Figure 39 into this work was completed according to the IEEE guidelines.

Permission granted for use of C-leg and Mauch SNS kinematics plots of Figure 1 from [38]

Type of permission requested for use of joint power plots of Figure 2 from [25]

Permission granted for use of joint power plots of Figure 2 from [25]

Permission granted for use and adaptation of coordinate system illustration of Figure 6
from [37]